DUST IN PLANETARY AND COMETARY ATMOSPHERES: AN EXPERIMENTAL AND COMPUTATIONAL STUDY BASED ON THE ANALYSIS OF A LUNAR DUST ANALOG

by

Jesús Escobar-Cerezo

PhD. dissertation

Supervisors:
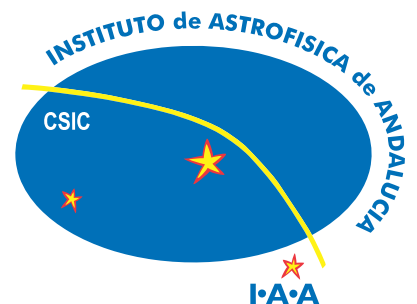Dra. Olga Muñoz Gómez & Dr. Fernando Moreno Danvila

Programa de Física y Ciencias del Espacio

Instituto de Astrofísica de Andalucía, (CSIC)

2018

UNIVERSIDAD DE GRANADA

A mis padres, María y Miguel,
a mis hermanos, Rocío y Javier,
y a mi mujer, Rocío.

Agradecimientos

Quiero agradecer a todo el personal del Instituto de Astrofísica de Andalucía el haberme acogido durante estos años y darme la oportunidad de hacer el doctorado. En particular quiero mencionar a los directores Pepe Vílchez y Antxon Alberdi, al personal de administración, a los técnicos del centro de cálculo y a los miembros del departamento del Sistema Solar. No me puedo olvidar de los compañeros que han trabajado conmigo en la investigación y el laboratorio, José Luis Ramos y Dani Guirado.

Agradecer y animar a todos los doctorandos que luchamos juntos por pasar por esta fase de aprendizaje, en especial Quique Macías, Naím Ramírez, Estefanía Casal, Antonio Fuentes y Salva Duarte. A aquellos compañeros que sin ser doctorandos son como nuestros hermanos mayores, Javi Blasco, Manu González y Marta González. Debo hacer una mención especial a Víctor Terrón por motivarme a mejorar mi kung fu en lo que a programación se refiere, y que es un ejemplo para mí de cómo debe ser una persona. Y especialmente quiero agradecer a los amigos que me han ayudado científicamente, tomando un café o haciendo vida fuera del trabajo: Ester Ramos, Pablo Galindo, Ana Karla Díaz y Pablo Ramírez.

I also want to thank to Karri Muinonen, Antti Penttilä and Tomas Kohout for hosting me during my stay in Finland. Without their work, help and support this thesis would not have been possible. I want to extent these thanks to the staff of the University of Helsinki.

Y por último y más importante quiero agradecer a mis directores de tesis, Olga Muñoz y Fernando Moreno, por haberme apoyado, enseñado y, como bien dice la palabra, dirigido en la buena dirección. Gracias por la paciencia que habéis tenido y por los valores que me habéis inculcado sobre como debe ser la buena ciencia. Pero mucho más importante, me habéis mostrado que para ser profesional no se tiene que dejar de ser buena persona. No se pueden pedir mejores mentores.

No puedo terminar sin agradecer a toda mi familia, mis padres, mis hermanos, mis tíos y mis primos que son los responsables en gran medida de ser como soy. Y sobre todo, a Rocío, porque gracias a ella he vivido los mejores años de mi vida, y los mejores que quedan por llegar. La mitad de esta tesis es mía. La otra mitad y lo que queda de mí es suyo.

PARTICIPATION IN CONGRESSES AND WORKSHOPS

Dust and Ice Particles Spectroscopy and Scattering, 2017 "Spectro-polarimetry as a tool for characterizing small cosmic dust grains." Olga Muñoz, Fernando Moreno, **Jesús Escobar-Cerezo** and Daniel Guirado (Oral presentation).

The 16th Electromagnetic and Light Scattering Conference, 2017 "Scattering by mm-sized cosmic dust grains" O. Muñoz, F. Moreno, D. Guirado, **J. Escobar-Cerezo** and J. W. Hovenier (Oral presentation).

The 16th Electromagnetic and Light Scattering Conference, 2017 "Light scattering by volcanic sand: single-scattering particles versus particulate surface" N. Zubko, O. Muñoz, E. Zubko, M. Gritsevich, J. Peltoniemi, **J. Escobar-Cerezo**, M. Berg, and J. Wen (Poster presentation).

The 16th Electromagnetic and Light Scattering Conference, 2017 "Scattering properties of large irregular cosmic dust particles at visible wavelengths", **J. Escobar-Cerezo**, C. Palmer, O. Muñoz, F. Moreno, A. I. Penttilä, and K. Muinonen (Oral presentation).

The 16th Electromagnetic and Light Scattering Conference, 2017 "Monte Carlo model of light scattered by mm-sized particles covered with micrometric irregular grains", D. Guirado, F. Moreno, O. Muñoz, and **J. Escobar-Cerezo** (Oral presentation).

6th Mars Atmosphere Modelling and Observations Workshop , 2017 "Light Scattering by Martian Dust Analogues", O. Muñoz, **J. Escobar-Cerezo**, D. Guirado, F. Moreno (Oral presentation).

European Conference on Laboratory Astrophysics: Gas on the rocks, 2016 "Scattered light as a diagnostic tool for characterizing cosmic dust grains. The IAA-COsmic DUst LABoratory". O. Muñoz, Fernando Moreno, **Jesús Escobar-Cerezo**, Daniel Guirado, Joop W. Hovenier (Oral presentation).

European Conference on Laboratory Astrophysics: Gas on the rocks, 2016 "Simulated reflectance spectra for space weathered lunar regolith". **J. Escobar-Cerezo**, A. Penttilä, T. Kohout, O. Muñoz, F. Moreno, K. Muinonen (Poster presentation).

A LABoratory spectroscopy workshop for ASTROphysics (ALABASTRO), 2016 "Impact of ice coatings and/or inclusions on the scattering properties of large cosmic dust grains". **Jesús Escobar-Cerezo**, Olga Muñoz, Fernando Moreno, Karri Muinonen, Antti Pentillä (Oral presentation).

Workshop CSIC-CNRS New Frontiers in Astrophysics: from the laboratory to space, 2015 "Experimental scattering matrices of lunar dust simulant at 488nm and 520nm" **J. Escobar-Cerezo**, O. Muñoz, D. Guirado, F. Moreno, J. L. Ramos, E. J. Garboczi, J. D. Goguen, Ann Debay, T. Lafarge (Oral presentation).

IV Reunión sobre Ciencias Planetarias y Exploración del Sistema Solar (CPESS4), 2015 "Experimental scattering matrices of lunar dust simulant at 488nm and 520nm" **J. Escobar-Cerezo**, O. Muñoz, D. Guirado, F. Moreno, J. L. Ramos, E. J. Garboczi, J. D. Goguen, Ann Debay, T. Lafarge (Oral presentation).

The 3rd SOLARNET workshop Polarization in the Sun, the Solar System, and Beyond, 2015 "Experimental scattering matrices of lunar dust simulant at 488nm and 520nm" **J.**

Escobar-Cerezo, O. Muñoz, D. Guirado, F. Moreno, J. L. Ramos, E. J. Garboczi, J. D. Goguen, Ann Debay, T. Lafarge (Oral presentation).

PUBLISHED WORKS

Escobar-Cerezo, J., Muñoz, O., Moreno, F., Guirado, D., Gómez Martı, J.C., Goguen, J.D., Garboczi, E.J., Chiaramonti, A.N., Lafarge, T., West, R.A. "Experimental scattering matrix for lunar regolith simulant JSC-1A at visible wavelengths" *The Astrophysical Journal Supplement Series*, Accepted (2018).

Escobar-Cerezo, J., Penttilä, A., Kohout, T., Muñoz, O., Moreno, F., Muinonen, K. "Simulations of Effects of Nanophase Iron Space Weather Products on Lunar Regolith Reflectance Spectra" *The Astrophysical Journal*, Volume 853, Issue 1, article id. 71, 6 pp. (2018).

Muñoz, O., Moreno, F., Vargas-Martín, F., Guirado, D., Escobar-Cerezo, J., Min, M., Hovenier, J. W. Experimental Phase Functions of Millimeter-sized Cosmic Dust Grains. *The Astrophysical Journal*, Volume 846, pp. 846-885 (2017).

Escobar-Cerezo, J., Palmer, C., Muñoz, O., Moreno, F., Penttilä, A., Muinonen, K. "Scattering Properties of Large Irregular Cosmic Dust Particles at Visible Wavelengths" *The Astrophysical Journal*, Volume 838, Issue 1, article id. 74, 17 pp. (2017).

BOOK CHAPTERS

The Methodology chapter presented in this thesis will be included slightly modified in a book to be edited by Springer.

Resumen

Esta tesis se enmarca en el estudio de scattering de luz visible por muestras de partículas irregulares cuyo tamaño es mayor al de la longitud de onda de la luz incidente. En Astronomía existe una amplia variedad de escenarios donde los procesos físicos asociados a la interacción de la luz con las partículas de polvo juegan un paper muy relevante. Algunos ejemplos son la ceniza volcánica o arena de los desiertos en suspensión en la atmósfera terrestre, las nubes de ácido sulfúrico en Venus, los tolines orgánicos en la atmósfera de Titán, o el polvo zodiacal en el Sistema Solar. A través del estudio de la función de fase y de la polarimetría se ha conseguido obtener información valiosa de estas muestras sin necesidad de tener acceso físico a ellas.

En nuestro caso, estamos interesados en caracterizar la respuesta espectropolarimétrica del regolito lunar. El regolito puede definirse como el material no consolidado en forma de granos o polvo que se encuentra sobre el lecho de roca sólida. Además, este material ha sido alterado con respecto al material primigenio rocoso por estar expuesto a la radiación y los impactos de meteoritos. La polarimetría de la Luna ha sido estudiada a partir de observaciones desde la Tierra durante los últimos dos siglos, pero cuando finalmente se consiguió llegar a su superficie y regresar con muestras reales, la mayor parte de las preguntas por responder fueron resueltas. Sin embargo, el método de estudio por técnicas remotas siguió desarrollándose ya que podía ayudar a caracterizar observaciones de otros planetas y satélites del Sistema Solar. De hecho, en los últimos años se ha propuesto usar la polarimetría para estudiar exoplanetas.

El objetivo de esta tesis es el de caracterizar el simulante lunar JSC-1A mediante su matriz de scattering. Para ello, se han realizado medidas experimentales en el COsmic DUst LABoratory situado en el Instituto de Astrofísica de Andalucía en Granada, España (IAA-CODULAB). Las medidas fueron realizadas a tres longitudes de onda en el visible (488, 520 y 647 nm) para ángulos de scattering comprendidos entre $3°$ y $177°$. Para poder facilitar su uso en aquellas investigaciones que requieran conocer la matriz de scattering en todo el rango de ángulos, se ha calculado por extrapolación una matriz sintética definida de $0°$ a $180°$.

Para completar las medidas de laboratorio se han realizado simulaciones de partículas irregulares usando el código SIRIS desarrollado en la Universidad de Helsinki. Este código simula particulas irregulares usando formas gaussianas aleatorias a las que además se le pueden incluir heterogeneidades internas y externas para simular inclusiones o rogusidad superficial. Primero se ha hecho un estudio metódico de los distintos parámetros que caracterizan a la partícula (tamaño, índice de refracción y composición de las heterogeneidades) para ver cómo se ve afectada la matriz de scattering. Una vez testeado el código, nos propusimos reproducir los efectos de la "erosión espacial" sobre el espectro de reflectancia de una muestra prístina de regolito lunar. Esta erosión espacial se produce cuando las partículas se encuentran expuestas al vacío del espacio, sufriendo impactos de meteoroides y efectos de la radiación cósmica y solar. Estos efectos generan nanopartículas de hierro reducido (Fe^0) que afectan al espectro de reflectancia oscureciéndolo, enrojeciéndolo y disminuyendo

la profundidad de las bandas de absorción. El código SIRIS reprodujo estos efectos al incluir partículas nanométricas con las características ópticas del Fe^0 como inclusiones dentro del regolito lunar.

Contents

Chapter 1

Introduction

With a few exceptions (e.g., gravitational waves, neutrinos, or cosmic rays detection), most astronomical observations are based on the study of the electromagnetic radiation that the heavenly bodies emit or reflect. When visible radiation interacts with matter, it can be partially absorbed and partially scattered in all directions. In this thesis we deal with the scattering processes occurring at the surface of the Moon. Since the light scattered is sensitive to the physical properties of the dust particles (e.g., size, shape, composition), this process can be used to assess the properties of the dust particles composing the lunar regolith. In that respect, polarimetric studies of the Moon surface have been made as early as the second half of the nineteenth century (see the review by Fielder (1961)). Those studies were constrained to certain lunar phases (i.e. waxing, full moon, and waning) and were aimed at retrieving the surface composition. Those studies suggested very polished surfaces of glass, igneous rocks or even ice. Lyot (1929) performed the first ground-based measurement of the polarimetric phase dependence of the Moon (from 0° to 160°). The phase curve showed a positive polarization maximum near 90° and a negative polarization branch at small phase angles. The interpretation of these results lead to the conclusion that the surface was actually composed by powder or sand. The observational campaigns continued consistently until the arrival of man to the Moon. Since the Apollo missions, the scientific community has had access to lunar regolith samples to study their physical and chemical properties and many questions were answered. The lunar regolith composition was described as being similar to some basalt species found on Earth, and new classifications appeared due to the different characteristics between mare regolith and highland regolith. The maria (Latin for "seas") are dark plains on the Moon's surface, mainly basaltic and geologically younger than the highlands, which are predominantly composed by anorthosites and present a brighter aspect than the maria. Another important difference is their iron content, which is higher in the mare regolith.

The spectropolarimetric surveys of the Moon continued because the development of this technique might help to characterize other planet surfaces as those of Mars and Venus, as well as asteroids and comets. Ground-based observations, satellite research and unmanned sample return missions (as the Luna soviet program) were carried out in the last decades

of the twentieth century. Some examples of these scientific results can be found in Doll-fus et al. (1971), Shkuratov et al. (1992a), Shkuratov et al. (1992b), and Shkuratov et al. (2011). The interest in the spectropolarimetric response of the lunar regolith has increased in recent years since Sterzik et al. (2012) proposed a new approach to detect biosignatures in Earth-like exoplanets. To test this method, the Earthshine on the Moon was studied. The Earthshine is the reflected light by the Earth's surface seen in the unlit portion of the Moon. It carries spectropolarimetric information about the Earth, but also about the Moon's surface which is used as mirror in this experiment. To subtract the Moon component, the lunar regolith spectropolarimetry has to be well characterized in the visible range. Parameters as the refractive index or the depolarization factor of the lunar regolith are not accurately known, so average values have been commonly used (see e.g. Sterzik et al., 2012). Also, a better understanding of the regolith properties and their effect on its spectropolarimetric observations would help to discriminate among the several possible sources of the observed effects.

As stated earlier, this thesis is devoted to study the scattering properties of the lunar regolith. To reach this goal, both experimental and computational approaches are used. From the experimental point of view, the laboratory results are aimed at characterizing the physical properties of the sample's particles as refractive index, size and shape, as well as their scattering matrices as functions of the scattering angle and corresponding asymmetry parameter. These measurements have been performed at the COsmic DUst LABoratory located at the Instituto de Astrofísica de Andalucía in Granada, Spain (IAA-CODULAB, Muñoz et al., 2010). Due to the fact that the lunar regolith is a scarce resource, lunar analogs have been used instead. An example of these analogs is the JSC-1A lunar simulant, where JSC stands for Johnson Space Center. This is a mare lunar regolith which has been designed to reproduce the size distribution and chemical composition of the Apollo 14 regolith sample 14163 as close as practical. In this thesis, the experimental measurements of the scattering matrix of the JSC-1A simulant at three optical wavelengths are presented.

Experimental data can be used in comparison with astronomical observations or to test advanced numerical techniques that model the scattering by irregular particles. Moreover, the problem under consideration may benefit from both laboratory measurements and computer simulations because they complement each other. Once the code is tested against experimental data it can be used to perform calculations at other sizes, compositions, angles, or wavelengths at which the experiments are difficult or not possible at all. Because of these reasons, the results presented in this thesis are a combination of experimental measurements and computational simulations.

One of the first things to consider when computing the scattering by irregular particles is the size parameter, which is a relationship between the size of the particle and the wavelength of the incident light. There are three different optical regimes depending on the size parameter: geometric optics when the particle size is much larger than the wavelength, the resonance regime when they are comparable, and the Rayleigh regime for those particles much smaller than the wavelength. The simulations carried out in the present work refer to the geometric optics regime.

Different approaches can be used in terms of the particle shape. For any particle shape with a size much smaller than the wavelength the Rayleigh approximation can be used as this does not depend on the shape (Rayleigh, 1881). If the particle is spherical or an infinite cylinder the Lorenz-Mie solution can be applied (Mie, 1908). The light scattering pattern by non-spherical particles can be computed by other methods, e.g. the T-matrix (Waterman, 1965; Mishchenko et al., 1996), discrete dipole approximation (DDA, see Draine et al., 1994) or finite-difference time-domain method (FDTD, see Yang et al., 2000). Finally, one of the multiple examples to reproduce more irregular particles is presented in Muinonen et al. (2009). The latter model mimics the irregularity of the shape by using the so-called Gaussian random shapes. The irregularity of these particles follows a probability density function whose parameters are tuned by the user. The results of the simulations presented in this thesis have been obtained using the code called SIRIS developed at the University of Helsinki. The SIRIS code also accounts for wavelength-sized inhomogeneities in the particle. Thereby, the scattered light carries information about particle features as internal inclusions of different composition and small-scale structure mimicking a surface roughness.

Thanks to the improvements in the SIRIS code that allow to include internal inhomogeneities presented above, another aspect of the regolith have been studied in this thesis: the space weathering products. The space weathering occurs when the regolith is exposed to the harsh environment of outer space in airless bodies. The galactic and solar cosmic rays in combination with meteoroid impacts and sputtering from the solar wind particles produce iron reduced nanoparticles inclusions (Fe^0) inside a regolith particle near the grain surface. These nanoparticles may appear as nanospheres smaller than 33 nm, known as nanophase iron, or larger particles, known as Britt-Pieters microphase (Britt et al., 1994). The space weathering affects strongly the reflectance spectra of the regolith, increasing the spectral slope for long wavelengths (reddening), decreasing the reflectance at all wavelengths (darkening) and shallowing the absorption bands at 1 and 2 μm due to Fe^{2+} in silicates. In this thesis, several space weathering simulations are presented, qualitatively reproducing these effects over the reflectance spectra.

One of the most difficult and important parameters of the lunar regolith to be measured is the complex refractive index. As the regolith presents a size distribution of particles and the sample composition may change from size to size (i.e. smaller sizes may have more agglutinates and glasses (McKay et al., 1974)) the refractive index span a large range of possible values. Several methods have been used in the past to estimate that quantity, as employing typical values of analog materials (Goguen et al., 2010), compute inverse models fixing different optical parameters (Shkuratov et al., 1999) or use the Umov's law (Umov, 1905). The latter states that the maximum degree of polarization is inversely proportional to the albedo, and has been profusely used in the literature (e.g., Wolff, 1980; Shkuratov et al., 1992b; Zubko et al., 2011). In this thesis we use the experimental laboratory measurements of the scattering matrix to qualitatively characterize the imaginary part of the refractive index of the JSC-1A sample. The polarization color have proved to be useful in the past, specifically to asses whether the behaviour of the imaginary part of the refractive index was constant or not in the measured wavelength range (Dabrowska et al., 2015). In addition,

derived from the space weathering's computations presented above we have been able to model the wavelength dependence of the imaginary part of the refractive index of a non-weathered lunar regolith sample. This has been done by fitting its reflectance spectra with several simulations.

Chapter 2

Methodology

Irregular cosmic dust grains play an important role in the radiative balance of planetary and cometary atmospheres in the Solar System. Light scattering properties of spherical particles can be computed from Lorenz-Mie solution. However, an exact solution for realistic polydispersions of irregular dust grains is extremely difficult to compute if possible at all. Therefore, an experimental study of the scattering behaviour of irregular dust particles that are candidates to be present in different astronomical scenarios is of main importance in order to interpret space- and ground-based observations.

In this chapter we present the COsmic DUst LABoratory developed at the Instituto de Astrofísica de Andalucía, CSIC (IAA-CODULAB) (Muñoz et al., 2010). The IAA-CODULAB is devoted to experimentally obtaining the angle dependence of the scattering matrices of clouds of small cosmic dust particles. We are especially interested in mineral dust particles that are candidates for being present in planetary and cometary atmospheres of the Solar System (olivines, pyroxenes, calcite, carbon, etc).

First, we present a theoretical background on the scattering matrix for non-spherical particles. This section is followed by a description of the experimental apparatus. The chapter continues with a section about the tests performed to validate the experimental results. At the end of the chapter a section devoted to explain the SIRIS code used to perform the simulations of this thesis is presented.

It is not the purpose of this chapter to fully describe the electromagnetic scattering phenomenon from an exact mathematical framework. In this chapter we study the scattering produced by particles of the order and larger than the wavelength. As we study these processes from a macroscopic point of view, we work with some restrictions that are thoroughly used and justified in the literature of light scattering (see, e.g. van de Hulst, 1957; Mishchenko et al., 2000; Mishchenko et al., 2002; Hovenier et al., 2004; Mishchenko, 2014). These are:

- We only consider elastic scattering, i.e. the frequency of the scattered light is the same as that of the incident light. Inelastic scattering phenomena as Raman and Brillouin scattering or fluorescence are not considered.

- We study scattering only in the far-field zone, where the propagation of the scattered wave is away from the particle, the electric vector vibrates in the plane perpendicular to the propagation direction, and the scattered field amplitude decreases inversely with distance from the particle. Furthermore, if the subject of study is a cluster of particles, the far-field zone is further than any linear dimension of the cluster (Mishchenko et al., 2002).

- Particles forming a cloud are considered as independent scatterers. The scattered field by each particle is the composition of the reactions to the external field and the secondary fields scattered by the surrounding particles. If the number of particles is sufficiently small and their relative distances sufficiently large, the contribution of these secondary waves is negligible compared to the external field. The total scattered field can be computed by the sum of the fields generated by the individual response of each particle to the incident field. This is known as single-scattering approximation (Mishchenko et al., 2002).

- Connected with the previous restriction, the assumption of independent scattering means that there is no systematic relation between the phases of all the waves present in the system (scattered and external). The phase differences may change completely when the particles are slightly altered (in position or orientation). The net effect is that for all practical purposes the scattered intensities by the ensemble of particles must be added without regard to phase. The scattering is considered incoherent (van de Hulst, 1957). In the forward direction, at nearly zero angle, no scattering in the ordinary sense can be observed.

2.1 Polarization parameters and scattering matrix.

One of the first parameters that appears when studying the electromagnetic radiation is the specific intensity I (or simply, the intensity). The radiant energy $\mathrm{d}E$ depends on the intensity I as follows (Hovenier et al., 2004):

$$\mathrm{d}E = I\mathrm{d}\nu\mathrm{d}\sigma\mathrm{d}\Omega\mathrm{d}t, \tag{2.1}$$

where $\mathrm{d}\nu$ defines the frequency interval $\nu \rightarrow \nu + \mathrm{d}\nu$, $\mathrm{d}\sigma$ is the surface area traversed by the energy perpendicular to the propagation direction of I, $\mathrm{d}\Omega$ the solid angle element that confines the directions studied and $\mathrm{d}t$ the time interval. The SI units of the intensity are W $\mathrm{Hz}^{-1}\mathrm{m}^{-2}\mathrm{sr}^{-1}$.

A beam of light is not only characterized by its intensity. In 1852, sir George Stokes introduced the so-called Stokes parameters, which represent exactly the polarization state and intensity of a beam of light propagating in certain a direction. It has to be taken into account that these parameters are, in most cases, used in a relative sense, i.e. compared to another Stokes parameters either of the same beam or from another beam (Hovenier et al.,

2004). These are named I, Q, U and V. I represents the intensity, Q and U characterize the linear polarization, and V the circular polarization. They are related in general by (Mishchenko et al., 2002):

$$I^2 \geq Q^2 + U^2 + V^2, \tag{2.2}$$

where equality holds when the beam of light is fully polarized. In the case of unpolarized light (also called natural light) $Q = U = V = 0$. In all other situations the light is called partially polarized.

Fluxes rather than intensities are considered in studies of single light scattering by small particles (Hovenier et al., 2004). We can define a flux vector $\pi\mathbf{\Phi} = \pi\{\Phi_1, \Phi_2, \Phi_3, \Phi_4\}$ where $\pi\Phi_1$ is the net flux, and Φ_2, Φ_3 and Φ_4 describe the polarization state of the beam of light in correspondence to the Stokes parameters Q, U and V. The net flux $\pi\Phi_1$ depends on I, and is described as the amount of energy flowing at a point of study in all directions per unit of frequency interval, of surface area, and of time. It is represented by the equation:

$$\pi\Phi_1 = \int \mathrm{d}\Omega I \cos\epsilon, \tag{2.3}$$

where the term $\cos\epsilon$ is the correction for the projected surface area in the case that the propagation direction of I is not perpendicular to the surface $d\sigma$ of Eq. 2.1. The net flux has SI units of W $\mathrm{Hz}^{-1}\mathrm{m}^{-2}$.

The scattering matrix $\mathbf{F}$ characterizes the polarimetric response of an ensemble of particles under incident electromagnetic radiation. In what follows, we assume that the particles are not optically active. The scattering matrix relates for each scattering direction the flux vector of the incident light, $\pi\mathbf{\Phi}_{inc}(\lambda, \theta)$, to the flux vector of the scattered light, $\pi\mathbf{\Phi}_{sca}(\lambda, \theta)$. The scattering matrix elements F_{ij} are dimensionless, and they depend on particle's physical properties as size, shape, and refractive index, as well on the wavelength of the incident light. The most general form of a scattering matrix is:

$$\begin{pmatrix} F_{11} & F_{12} & F_{13} & F_{14} \\ F_{21} & F_{22} & F_{23} & F_{24} \\ F_{31} & F_{32} & F_{33} & F_{34} \\ F_{41} & F_{42} & F_{43} & F_{44} \end{pmatrix}, \tag{2.4}$$

where we have sixteen elements. If we suppose that the particles are randomly oriented, certain relationships are given between them (see e.g. Hovenier et al., 2004, Section 2.4.1):

$$\frac{F_{21}(\theta)}{F_{11}(\theta)} = \frac{F_{12}(\theta)}{F_{11}(\theta)}, \tag{2.5}$$

$$\frac{F_{31}(\theta)}{F_{11}(\theta)} = \frac{-F_{13}(\theta)}{F_{11}(\theta)}, \tag{2.6}$$

$$\frac{F_{41}(\theta)}{F_{11}(\theta)} = \frac{F_{14}(\theta)}{F_{11}(\theta)}, \tag{2.7}$$

$$\frac{F_{32}(\theta)}{F_{11}(\theta)} = \frac{-F_{23}(\theta)}{F_{11}(\theta)}, \tag{2.8}$$

$$\frac{F_{42}(\theta)}{F_{11}(\theta)} = \frac{F_{24}(\theta)}{F_{11}(\theta)}, \tag{2.9}$$

$$\frac{F_{43}(\theta)}{F_{11}(\theta)} = \frac{-F_{34}(\theta)}{F_{11}(\theta)}, \tag{2.10}$$

which reduces the complexity to ten independent elements in the scattering matrix. In the case of randomly oriented particles, all scattering planes are equivalent, and the scattering direction is fully described by the scattering angle θ, which is the angle defined by the directions of the incident and scattered beams. Furthermore, if the studied sample consists of particles and their mirror particles in equal numbers, then $F_{13}(\theta)$, $F_{14}(\theta)$, $F_{23}(\theta)$, and $F_{24}(\theta)$ are identically zero for all scattering angles (van de Hulst, 1957). Under these conditions of randomly oriented particles and equal amounts of mirror particles, the governing equation relating the flux vectors of the incident and scattered beams can be written as:

$$\mathbf{\Phi}_{sca}(\lambda, \theta) = \frac{\lambda^2}{4\pi^2 D^2} \begin{pmatrix} F_{11} & F_{12} & 0 & 0 \\ F_{12} & F_{22} & 0 & 0 \\ 0 & 0 & F_{33} & F_{34} \\ 0 & 0 & -F_{34} & F_{44} \end{pmatrix} \mathbf{\Phi}_{inc}(\lambda, \theta), \tag{2.11}$$

where only six independent elements in the scattering matrix remain. The first elements of the column vectors are fluxes divided by π, and the other elements describe the state of polarization by means of the Stokes parameters; λ is the wavelength, and D is the distance between the detector and the sample.

The $F_{11}(\theta)$ element describes the angular distribution of scattered light by the sample. It is important to remark that the measured values of $F_{11}(\theta)$ for the aerosol samples in the laboratory setup presented in Section 2.2 (Muñoz et al., 2010; Muñoz et al., 2012) are arbitrarily normalized so that they are equal to 1 at $\theta = 30°$. The function $F_{11}(\theta)$, normalized in this way, is proportional to the flux of the scattered light for unpolarized incident light and called the phase function or scattering function throughout this manuscript.

The $-F_{12}(\theta)/F_{11}(\theta)$ ratio is equivalent to the degree of linear polarization for unpolarized incident light. The degree of linear polarization can be defined through the Stokes parameters as:

$$P_L = -\frac{\sqrt{Q_{sca}^2 + U_{sca}^2}}{I_{sca}}, \tag{2.12}$$

but if the incident light is unpolarized, i.e. $U_{inc} = Q_{inc} = V_{inc} = 0$, then the Eq. 2.12 simplifies to $-Q_{sca}/I_{sca}$. Also, if measurements are performed at different wavelengths, we can obtain information about the polarization color. This can be described as the difference between the $-F_{12}(\theta)/F_{11}(\theta)$ ratios at two different wavelengths.

The $F_{22}(\theta)/F_{11}(\theta)$, $F_{33}(\theta)/F_{11}(\theta)$ and $F_{44}(\theta)/F_{11}(\theta)$ ratios can be used as indicators of the non-sphericity of the particle. The Lorenz-Mie solution of light scattering by homogeneous isotropic spheres states that the identities $F_{22}(\theta) \equiv F_{11}(\theta)$ and $F_{33}(\theta) \equiv F_{44}(\theta)$ must be fulfilled. Moreover, the linear and circular backscattering depolarization ratios, δ_L and δ_C respectively, are defined as (see e.g. Mishchenko et al., 2002)

$$\delta_L = \frac{F_{11}(\pi) - F_{22}(\pi)}{F_{11}(\pi) + F_{22}(\pi)}, \tag{2.13}$$

$$\delta_C = \frac{F_{11}(\pi) + F_{44}(\pi)}{F_{11}(\pi) - F_{44}(\pi)}, \tag{2.14}$$

and are related for macroscopically isotropic and mirror-symmetric particles:

$$\delta_C = \frac{2\delta_L}{1 - \delta_L}, \tag{2.15}$$

These coefficients are useful in e.g. the lidar backscatter depolarization technique (LBDT). As these ratios must vanish for spherical particles, the detection of a non-zero ratio is indicative of irregular particles.

2.1.1 Synthetic scattering matrix.

The measurements are performed in the scattering angle range from 3° to 177°. The lack of measurements at forward and back-scattering angles limits the use of the measured scattering matrix data for radiative transfer calculations or comparisons with electromagnetic light scattering codes. To facilitate the use of the experimental data, the so-called synthetic scattering matrix $\mathbf{F^{syn}}$ is computed from the measurements through extrapolation to cover the whole scattering range. This function fulfills the condition (see Volten et al., 2006):

$$\frac{F_{11}(\theta)}{F_{11}(30°)} = \frac{F_{11}^{\text{syn}}(\theta)}{F_{11}^{\text{syn}}(30°)}. \tag{2.16}$$

This $F_{11}^{\text{syn}}(\theta)$ function is defined so that the normalization condition is fulfilled (see e.g. Mishchenko et al., 2000):

$$\frac{1}{2} \int_0^\pi \mathrm{d}\theta sin\theta F_{11}^{\text{syn}}(\theta) = 1. \tag{2.17}$$

The extrapolation of the $F_{11}^{\text{syn}}(\theta)$ element is computed as follows:

- The forward diffraction peak (0°-3°) is computed based on the assumption that the forward diffraction peak for randomly oriented particles with moderate aspect ratios mainly depends on the size of the particles and is only weakly dependent of their shape (Liu et al., 2003). The Lorenz-Mie solution is used to compute the scattering produced by projected-surface-area equivalent spheres between 0° and 3°. These computations depend on the size distribution and the refractive index of the sample.

- The back-scattering value at 180° is computed by applying the least squares method for a quadratic function using the measured data from 150° to 177° and calculating the value at 180° with the obtained function. An additional condition that must be fulfilled is that the scattering of random oriented irregular particles must be symmetric with respect to the forward and backward directions, so the first derivative for all the scattering elements must be null at 0° and 180° (Hovenier et al., 2014). The back-scattering is then reproduced with a cubic spline interpolation between the last measured data point (177°) and the extrapolated $F_{11}^{\text{syn}}(180°)$ value, taking into account the null derivative condition.

- At this point, the function is composed by the measured data from 3° to 177° and extrapolated data from 177° to 180°. This function is shifted vertically until the value of $F_{11}^{\text{syn}}(3°)$, as computed by Lorenz-Mie solution, matches the measured value of $F_{11}(3°)$.

The normalization condition given by Eq. 2.17 is then checked. If it is not satisfied within a 0.1 % accuracy, the value of $F_{11}(3°)$ is increased or decreased (within the experimental error bars) depending on whether the integral is greater or smaller than unity, and the three step process is repeated until the convergence criterion is reached.

The other missing values of the $\mathbf{F^{syn}}$ matrix elements are interpolated considering the well-known set of constraints of scattering matrices at forward and backward scattering as described in Hovenier et al., 2004:

$$\frac{F_{12}^{\text{syn}}(0)}{F_{11}^{\text{syn}}(0)} = \frac{F_{12}^{\text{syn}}(180°)}{F_{11}^{\text{syn}}(180°)} = \frac{F_{34}^{\text{syn}}(0)}{F_{11}^{\text{syn}}(0)} = \frac{F_{34}^{\text{syn}}(180°)}{F_{11}^{\text{syn}}(180°)} = 0, \tag{2.18}$$

$$\frac{F_{22}^{\text{syn}}(0)}{F_{11}^{\text{syn}}(0)} = \frac{F_{33}^{\text{syn}}(0)}{F_{11}^{\text{syn}}(0)} = 1, \tag{2.19}$$

$$\frac{F_{22}^{\text{syn}}(180°)}{F_{11}^{\text{syn}}(180°)} = -\frac{F_{33}^{\text{syn}}(180°)}{F_{11}^{\text{syn}}(180°)}, \tag{2.20}$$

$$\frac{F_{44}^{\text{syn}}(180°)}{F_{11}^{\text{syn}}(180°)} = 1 - 2\frac{F_{22}^{\text{syn}}(180°)}{F_{11}^{\text{syn}}(180°)}. \tag{2.21}$$

Only the value of $F_{22}^{\text{syn}}(180°)/F_{11}^{\text{syn}}(180°)$ must be extrapolated, using the same method as the $F_{11}^{\text{syn}}(180°)$ value explained above. In Figure 2.1, we present an example of the results of this extrapolation applied to a measurement of lunar regolith simulant at a wavelength of 488
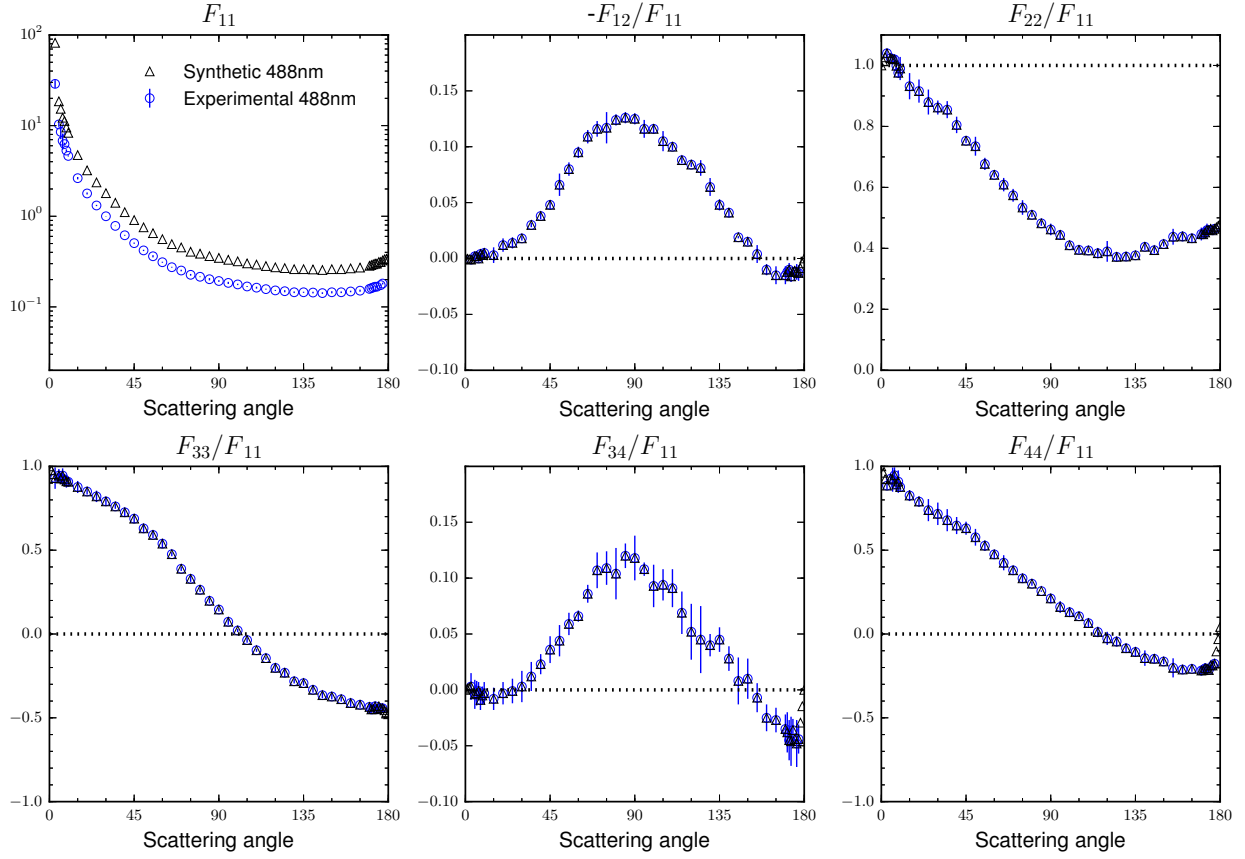
Figure 2.1: Comparison between the experimental scattering matrix of the JSC-1A lunar simulant at 488 nm (circles) and the extrapolated matrix (triangles). Note that measured $F_{11}(\theta)$ is normalized to unity at $30°$ whereas extrapolated $F_{11}^{\mathrm{syn}}(\theta)$ is normalized so that its average over all directions equals unity.

nm. Note that the measured $F_{11}(\theta)$ is normalized to unity at $30°$ whereas the extrapolated $F_{11}^{\mathrm{syn}}(\theta)$ is normalized so that its average over all directions equals unity, as stated in Eq. 2.17.

2.2   Laboratory apparatus.

In Figure 2.2 we show the IAA Cosmic Dust Laboratory (IAA-CODULAB) located at the Instituto de Astrofísica de Andalucía. The design is based on the Dutch instrument developed in the group of Prof. J.W. Hovenier at the Free University (Amsterdam) Hovenier, 2000; Volten et al., 2001) following the methodology described by Hunt et al., 1973.

A scheme of the setup is displayed in Figure 2.3. The light source is a tunable Ar-Kr laser, in which the emission wavelength values can be set to 483 nm, 488 nm, 520 nm, 568 nm, or 647 nm. Our measurements are usually presented only for 488 nm, 520 nm, and 647
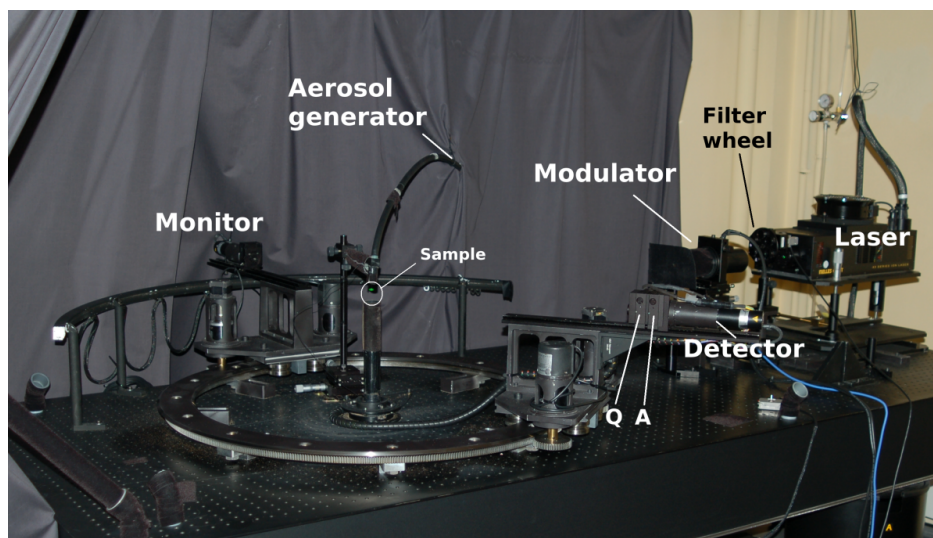
Figure 2.2: IAA Cosmic Dust Laboratory. The neutral filters are located in a filter wheel between the laser and the modulator. The integrated polarizer is coupled to the modulator. The quarter-wave plate (Q) and the analyzer (A) can be placed in the detector. In the center of the image the dust sample from the nebulizer can be seen as a bright dot. Two photomultipliers gather the signal: the detector which moves from 3° to 177° of scattering angle, and the monitor which is located in a fixed position to correct for fluctuations of dust density in the scattering volume. The sample comes out of the aerosol generator in the center of the apparatus.
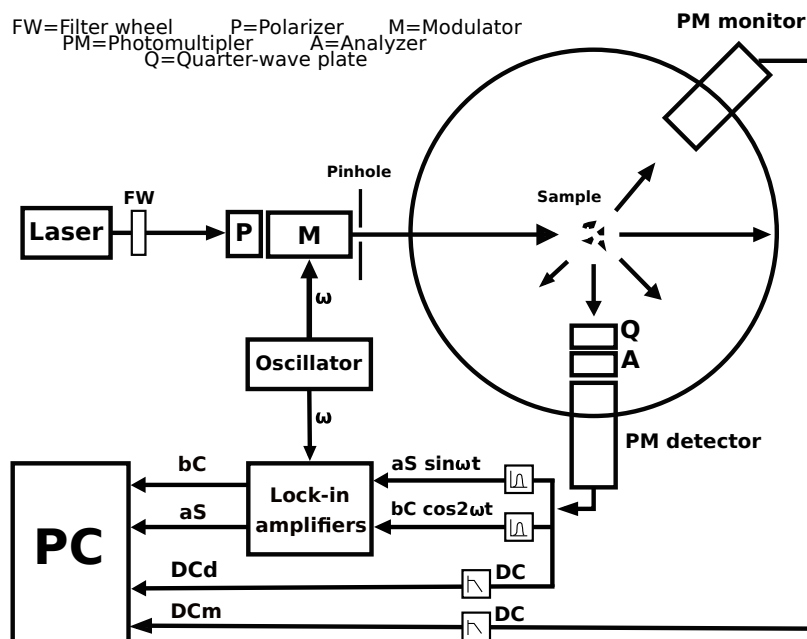

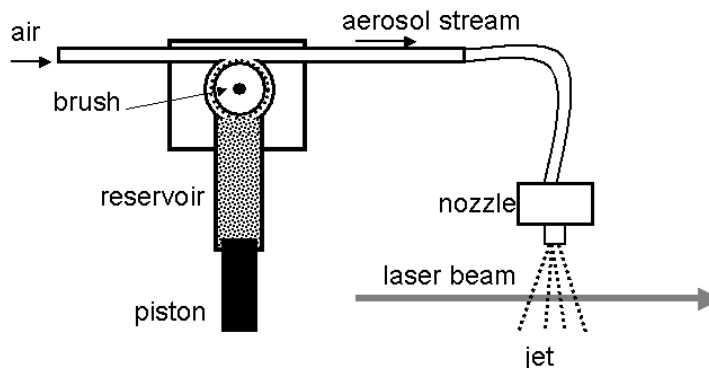Figure 2.3: Experimental laboratory scheme from Figure 2.2 (Muñoz et al., 2010).

Figure 2.4: Schematic picture of the aerosol generator. The dust sample in the reservoir is pushed onto the rotating brush by a piston at certain speed. An air stream carries the particles through a tube until a nozzle, which is placed above the laser path (Muñoz et al., 2011).

nm as these wavelength values are far enough from each other to produce differences in the scattering matrix elements. The light beam goes through an integrated polarizer (P) and an electro-optic modulator (M), which are present in all the optical configurations. The beam reaches the scattering volume, usually a dust sample coming from an aerosol generator, or a cloud of water droplets produced by a nebulizer. This design avoids the use of a container for the sample whose walls would potentially distort the scattered field or limit the angular range. The aerosol generator works as follows: a powder sample is loaded and compacted into a cylindrical reservoir; a piston pushes the powder onto a rotating brush at an adjustable speed; an air stream carries the aerosol particles of the brush through a tube to a nozzle above the scattering volume. A schematic picture of the aerosol generator is presented in Figure 2.4. The light is then scattered by the sample in all directions, reaching two photomultipliers which are placed on a one-meter radius goniometer ring. One of these photomultipliers acts as a detector, which can be moved along the ring from 3° scattering angle (nearly forward scattering) to 177° scattering angle (nearly backward scattering). The other photomultiplier is in a fixed position and works as a monitor to correct for possible fluctuations of the dust flux in the jet stream. Two optical elements can be placed in front of the detector, both optional depending on the optical configuration studied: a second polarizer acting as an analyzer (A), and a quarter-wave plate (Q). Along with these elements, a filter wheel (FW) is placed between the laser and the integrated polarizer (P), and a beam-stop is used to absorb the unscattered part of the incident beam.

The scattered flux vector of the light $\pi\boldsymbol{\Phi}_{sca}(\lambda, \theta)$ can be computed from the incident flux vector $\pi\boldsymbol{\Phi}_{inc}(\lambda, \theta)$ through the equation:

$$\boldsymbol{\Phi}_{sca}(\lambda, \theta) = c_1 \mathbf{A}_{\gamma_A} \mathbf{Q}_{\gamma_Q} \mathbf{F}(\theta) \mathbf{M}_{\gamma_M} \mathbf{P}_{\gamma_P} \boldsymbol{\Phi}_{inc}(\lambda, \theta) \tag{2.22}$$

where $\mathbf{A}$, $\mathbf{Q}$, $\mathbf{M}$, and $\mathbf{P}$ are the 4×4 Mueller matrices of the analyzer, the quarter-wave plate, the modulator, and the polarizer, respectively. The orientation angles γ_A, γ_Q, γ_M, and γ_P of the corresponding optical elements are the angles between their optical axes and the scattering plane, measured counter-clockwise from the scattering plane when looking in the direction of propagation of light. These matrices have the form:

$$\mathbf{A}_\gamma = \mathbf{P}_\gamma = \frac{1}{2} \begin{pmatrix} 1 & C & S & 0 \\ C & C^2 & SC & 0 \\ S & SC & S^2 & 0 \\ 0 & 0 & 0 & 0 \end{pmatrix}, \tag{2.23}$$

$$\mathbf{Q}_\gamma = \begin{pmatrix} 1 & 0 & 0 & 0 \\ 0 & C^2 & SC & -S \\ 0 & SC & S^2 & C \\ 0 & S & -C & 0 \end{pmatrix}, \tag{2.24}$$

where $C = \cos 2\gamma$ and $S = \sin 2\gamma$. However, the electro-optic modulator has a more complex Mueller matrix. It consists of a birefringent crystal whose birefringence is set by an electric field. The parallel and perpendicular components of light emerge from this element with a certain phase shift depending on the electric field applied. If the voltage over the crystal is varied sinusoidally in time, the induced phase shift ϕ varies in the same way. This modulation, in combination with the lock-in detection, increases the accuracy of the measurements and allows to determine several scattering matrix elements simultaneously. In order for this to happen, both electro-optic modulator and lock-in amplifiers must be synchronized through an oscillator. The phase shift is described by the formula:

$$\phi = \phi_c + \phi_0 \sin \omega t, \tag{2.25}$$

where ϕ_c is a constant phase shift owing to the intrinsic birefringence of the modulator crystal, ϕ_0 is the amplitude of the oscillating field and ω is the angular frequency applied to the field. Both ϕ_c and ϕ_0 depend on the wavelength, and must be calibrated when the laser device is tuned to a certain wavelength. ϕ_c is the phase shift produced by the modulator when no voltage is applied, so it must be corrected by the V_{DC} voltage. ϕ_0 is adjusted by the V_{AC} voltage as discussed below.

The Mueller matrix of the electro-optic modulator with an orientation γ_M between the scattering plane and its principal axis is:

$$\mathbf{M}_{\gamma_M}(\phi) = \begin{pmatrix} 1 & 0 & 0 & 0 \\ 0 & C^2 + S^2 \cos\phi & SC(1-\cos\phi) & -S\sin\phi \\ 0 & SC(1-\cos\phi) & S^2 + C^2 \cos\phi & C\sin\phi \\ 0 & S\sin\phi & -C\sin\phi & \cos\phi \end{pmatrix}, \qquad (2.26)$$

where ϕ is the phase shift from Eq. 2.25. We can decompose $\sin\phi$ and $\cos\phi$ in terms of their harmonics through the Fourier series of Bessel functions of the first kind:

$$\sin\phi = \sin(\phi_0 \sin\omega t) = 2\sum_{k=1}^{\infty} J_{2k-1}(\phi_0)\sin(2k-1)\omega t \qquad (2.27)$$

$$\cos\phi = \cos(\phi_0 \sin\omega t) = J_0(\phi_0) + 2\sum_{l=1}^{\infty} J_{2l}(\phi_0)\cos(2l)\omega t \qquad (2.28)$$

It is convenient to adjust the modulation voltage V_{AC} so that $J_0(\phi_0) = 0$, i.e. ϕ_0=2.40483 rad. Considering the terms of frequency 2ω or smaller only, the scattered intensity can be written as:

$$\mathbf{\Phi}_{sca}(\lambda, \theta) = c[DC(\theta) + 2J_1(\phi_m)S(\theta)\sin\omega t + 2J_2(\phi_m)C(\theta)\cos 2\omega t], \qquad (2.29)$$

where the coefficients $DC(\theta)$, $S(\theta)$ and $C(\theta)$ contain information about the scattering matrix elements, $2J_1(\phi_m)$=1.0383 and $2J_2(\phi_m)$=0.8635 (Muñoz et al., 2010), and c is a constant that depends on the measuring conditions. By using lock-in detection the $\sin\omega t$ and $\cos 2\omega t$ components can be separated from the total detected signal. This electronic configuration allows us to split the signal into $cDC(\theta)$, $c2J_1S(\theta)$ and $c2J_2C(\theta)$. The $c2J_1S(\theta)$ and $c2J_2C(\theta)$ signals are divided by $cDC(\theta)$, so the constant c vanishes. Thus, we can obtain all the scattering matrix elements with a handful of optical arrangements. Table 2.1 provides the results of different optical configurations on each channel.

Configuration	$\gamma_P(deg)$	$\gamma_M(deg)$	$\gamma_Q(deg)$	$\gamma_A(deg)$	$DC(\theta)$	$S(\theta)$	$C(\theta)$
1	45	0	-	-	F_{11}	$-F_{14}$	F_{13}
2	45	0	-	45	$F_{11} + F_{31}$	$-F_{14}$-F_{34}	F_{13}+F_{33}
3	45	0	0	45	$F_{11} + F_{41}$	$-F_{14}$-F_{44}	F_{13}+F_{43}
4	0	-45	-	-	F_{11}	$-F_{14}$	F_{12}
5	0	-45	-	0	$F_{11} + F_{21}$	$-F_{14}$-F_{24}	F_{12}+F_{22}

Table 2.1: Optical configurations and scattering elements retrieved from the three channels $DC(\theta)$, $S(\theta)$ and $C(\theta)$ (Muñoz et al., 2010).

As an example, if we select configuration 1 in Table 2.1, we obtain:

$$\mathbf{I}_{sca} = \mathbf{F}(\theta) \cdot \mathbf{M}_{0^{\circ}} \cdot \mathbf{P}_{45^{\circ}} \mathbf{I}_{in} = \left(\frac{I_{in} + U_{in}}{2} \right) \begin{bmatrix} F_{11} - F_{14} \sin\phi + F_{13} \cos\phi \\ F_{21} - F_{24} \sin\phi + F_{23} \cos\phi \\ F_{31} - F_{34} \sin\phi + F_{33} \cos\phi \\ F_{41} - F_{44} \sin\phi + F_{43} \cos\phi \end{bmatrix} \quad (2.30)$$

The detector only measures the intensity, i.e., the first component of the Stokes vector, $F_{11} - F_{14} \sin\phi + F_{13} \cos\phi$ in the previous equation. The information carried by each channel is F_{11} for the "DC channel", $-F_{14}$ in the "ω channel" ($S(\theta)$ coefficient in Eq. 2.29) and F_{13} in the "2ω channel" ($C(\theta)$ in the same equation).

2.3 Test measurements.

Owing to the complexity of the instrumental setup, many different tests must be performed to ensure the validity of the measurements. Among this, the correct alignment of the optical setup and the electronics must be tested, along with the fulfillment of the single scattering conditions and the absence of particle agglomeration. Also, the so-called Cloude coherence matrix test should be verified in order to mathematically validate the experimental data (Hovenier et al., 2000).

2.3.1 Water droplets and alignment simulation.

To test the optics alignment and electronics of our setup, we perform measurements of the scattering matrix of water droplets and these are compared with a Lorenz-Mie simulations for homogeneous spherical water droplets generated by a nebulizer. Since the size distribution of these water droplets is not known a priori, for the Lorenz-Mie computations a log-normal distribution of spheres is assumed with a refractive index typical for water at visible wavelengths m_{water}=1.33+i0.0. The log-normal distribution is characterized by the parameters σ_g and r_g, defined as

$$ln(r_g) = \int_0^{\infty} ln(rn(r))\mathrm{d}r, \quad (2.31)$$

$$\sigma_g^2 = \int_0^{\infty} (ln(r) - ln(r_g))^2 n(r)\mathrm{d}r, \quad (2.32)$$

where r is the sphere radius, $n(r)$ dr is the fraction of spheres between r and $r+dr$ per unit volume. These parameters are then fitted so that the differences between experimental and theoretical values of the $F_{11}(\theta)$ element and $-F_{12}(\theta)/F_{11}(\theta)$ ratio are minimal. The same procedure is applied at the three studied wavelengths (488 nm, 520 nm, and 647 nm).

In Figure 2.5 we present a comparison between the experimental measurements for water droplets at 520 nm wavelength and a Lorenz-Mie simulation for homogeneous spheres with
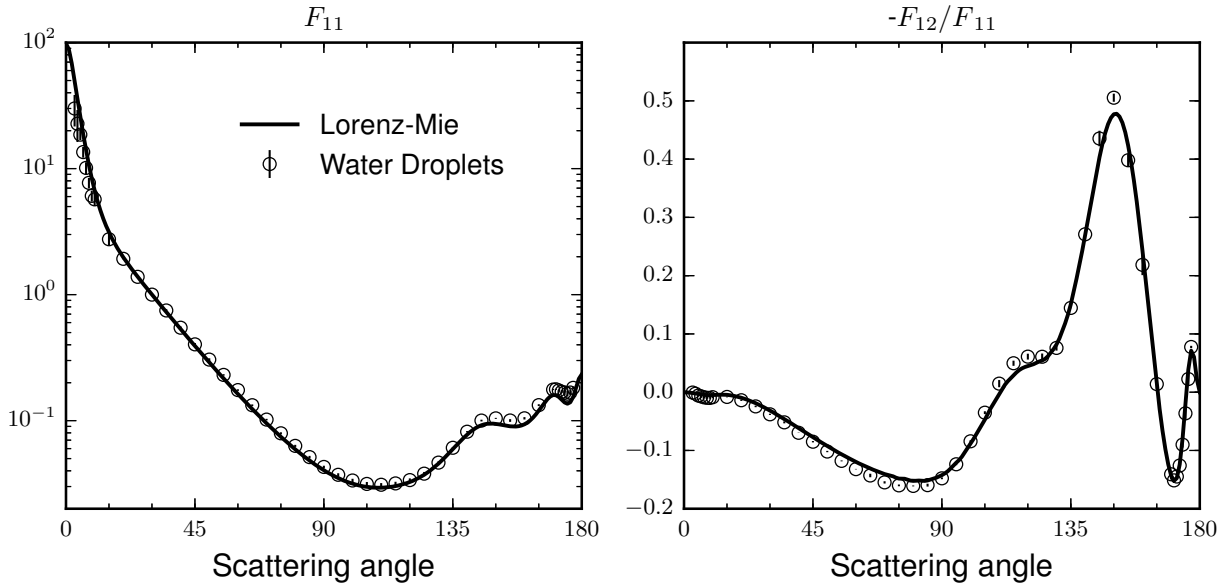
Figure 2.5: Comparison between the experimental $F_{11}(\theta)$ element and $-F_{12}(\theta)/F_{11}(\theta)$ ratio for water droplets at 520 nm wavelength and a Lorenz-Mie simulation for spheres with a refractive index of $m_{water} = 1.33 + i0$, r_g=0.68 μm and σ_g=1.76.

a refractive index of m= $1.33 + i0$ and the averaged values for the size distribution obtained from the best fits for the six studied functions, which are equal to r_g=0.68 μm and σ_g=1.76.

If the Lorenz-Mie simulation and the experimental scattering matrix for water droplets do not match, the differences must be due to systematic errors in the orientation of the principal axis of the optical elements. To locate which optical element could be causing the observed differences, we have developed a computational simulator of the optical train in our experiment based on the report of Kiphardt, 1993. This code sequentially simulates errors in the orientation angle γ on each Mueller matrix of the optical elements. Then it computes the Eq. 2.22, using as scattering matrix, $\mathbf{F}(\theta)$, the results of a Lorenz-Mie simulation for homogeneous water spheres. Depending on the optical configuration (Table 2.1) the output result of the equation can be predicted (as in Eq. 2.30). The output scattering matrix elements from the code (affected by the misalignment) are plotted against the expected results from the scattering matrix used as test (computed values from the Lorenz-Mie simulation considered as correct), and the misalignment effects are seen as differences between these two datasets. The study of different misalignment combinations on different optical elements gives us an idea of the origin of the problem. The affected element is then realigned accordingly, the experimental matrix is measured again, and the test is performed one more time. As an example, in Figures 2.6 and 2.7 we present the results of the simulations when errors in the alignment of the optical axis are present in the polarizer, P, and the modulator, M, respectively. The log-normal parameters for the simulated water spheres are r_g=0.75 μm and $\sigma_g = 0.205$, and λ=632.8 nm. Each column corresponds to a channel of information (as

described in Eq. 2.29), and each row corresponds to an optical configuration. In both figures the error values introduced are 4, 8, 12 and 16 degrees counter-clockwise. In Figure 2.8, the same errors that appear in Figures 2.6 and 2.7 are applied simultaneously to the polarizer and the modulator. It is interesting to note that in Figure 2.8, certain combinations of misalignments can compensate their effects, as seen in the central column, where no deviation is observed. This makes uneasy the detection of the cause of these problems. Because of this, it is important to measure and simulate the whole scattering matrix at several wavelengths.

2.3.2 Single scattering condition.

As stated at the beginning of the chapter, the single-scattering condition must be met in our experiment. The number of particles interacting with the laser during a measurement must be large enough to be representative of the sample, but not so much that multiple scattering may start playing a role.

To test if the single scattering condition is fulfilled in the laboratory, flux measurements with the detector in a fixed position can be made as suggested by Hovenier et al., 2003. Under single scattering conditions, the signal detected must vary linearly with the number density of particles. In the laboratory setup explained in Section 2.2, the amount of particles in the scattering volume is controlled by the piston's speed of the aerosol generator. In Figure 2.9 a test is presented for white clay particles with the detector fixed at a scattering angle of 10°. In this laboratory setup the typical speed used is in the range from 40 mm/h to 100 mm/h, depending on the physical properties of the sample and on the wavelength. As it can be seen in the figure, the speed values span from 50 mm/h to 250 mm/h, where even at this high value the trend is still linear. The results presented in Figure 2.9 confirm that the measurements are carried out in single-scattering conditions.

2.3.3 Particle aggregation.

One reasonable question about the laboratory setup is if the aerosol generator changes the shape/size of the sample studied, either by breaking the particles into smaller ones or by inducing some agglomeration. To test this, Field Emission Scanning Electron Microscope (FESEM) images are taken from the sample from the jet stream after it comes out from the aerosol generator. These are compared with images taken from unprocessed sample extracted directly from the container. As it can be seen in Figure 2.10, there are no substantial changes between the left panel (sample from the container) and the right panel (sample after it passes through the aerosol generator). The particles show same general structure and surface roughness, which indicates that no damage has occurred to the shapes. Also we can notice very small particles adhered to the surfaces of larger particles, probably due to electrostatic force. This results prove that the sample maintains its size and shape properties through the aerosol generator.
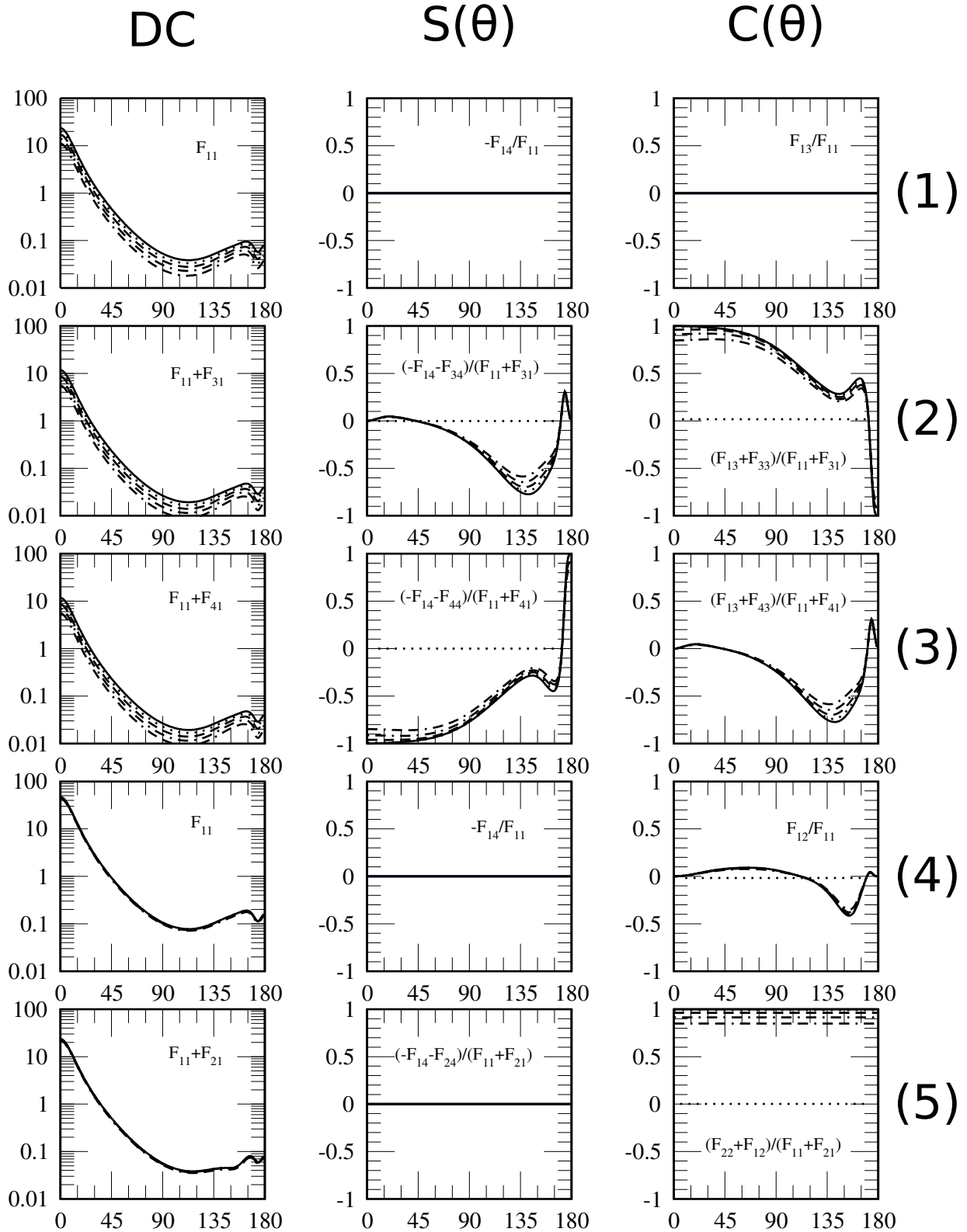
Figure 2.6: Results of the simulation when the orientation angle of the polarizer is not correctly aligned. The angle errors introduced (counter-clockwise) in degrees are 4 (dotted line), 8 (dashed line), 12 (dot-dashed line) and 16 (dot-dash-dash line). The columns correspond to the channels DC, $S(\theta)$ and $C(\theta)$, and each row corresponds to an optic configuration as shown in Table 2.1.
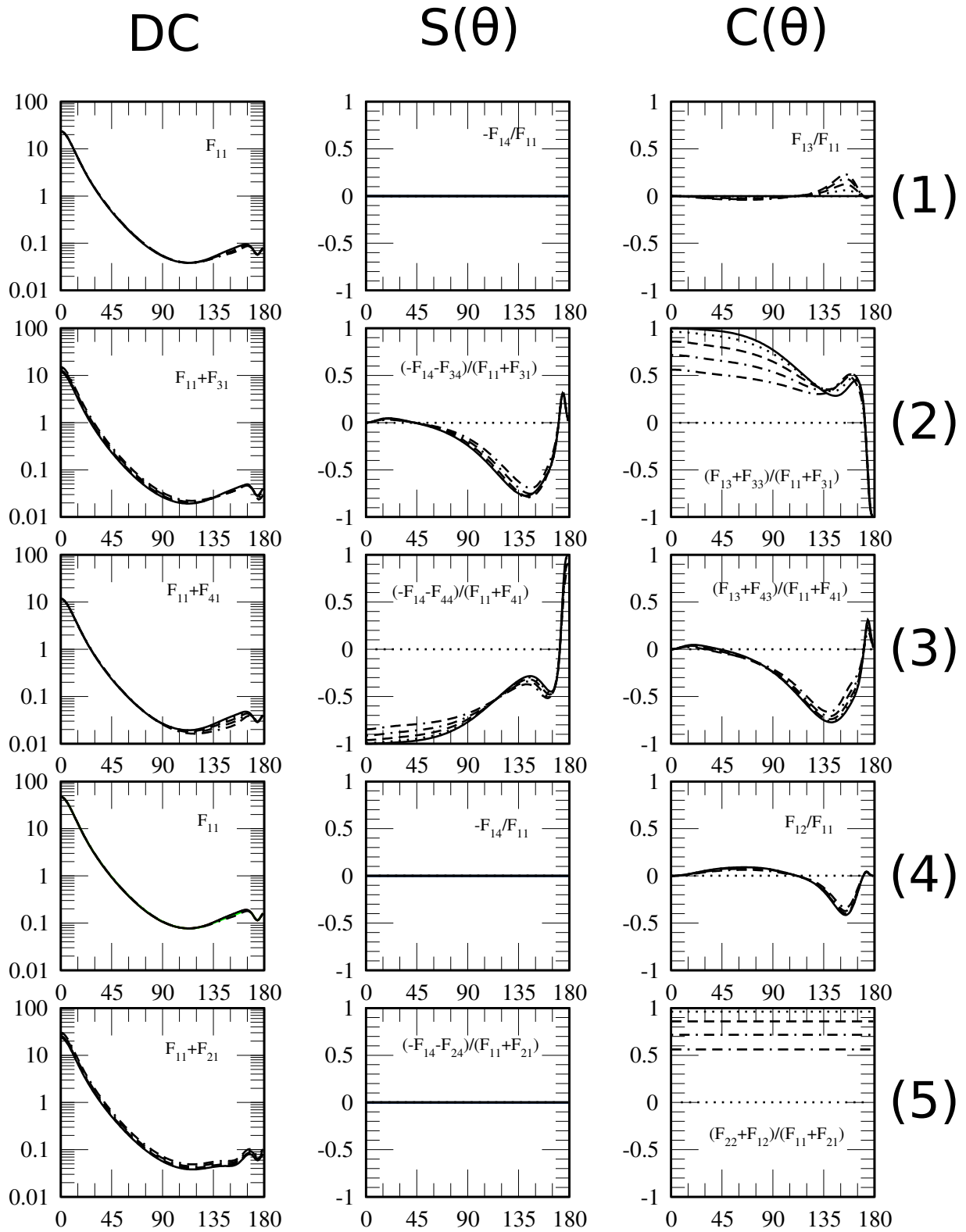
DC   S(θ)   C(θ)

Figure 2.7: As Figure 2.6 but the errors are applied to the modulator.
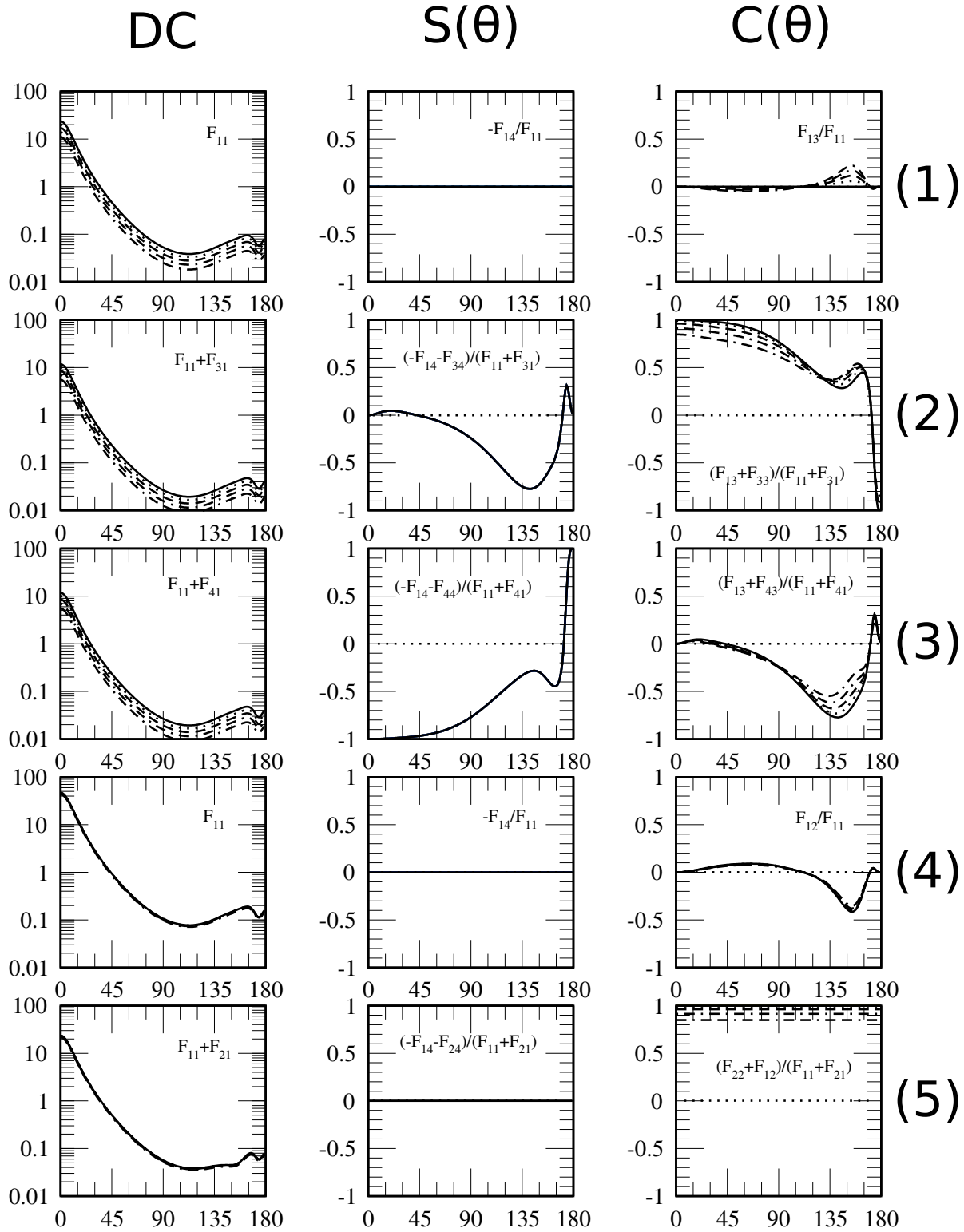
Figure 2.8: As Figures 2.6 and 2.7, but equal errors are introduced in both optical elements (counter-clockwise).
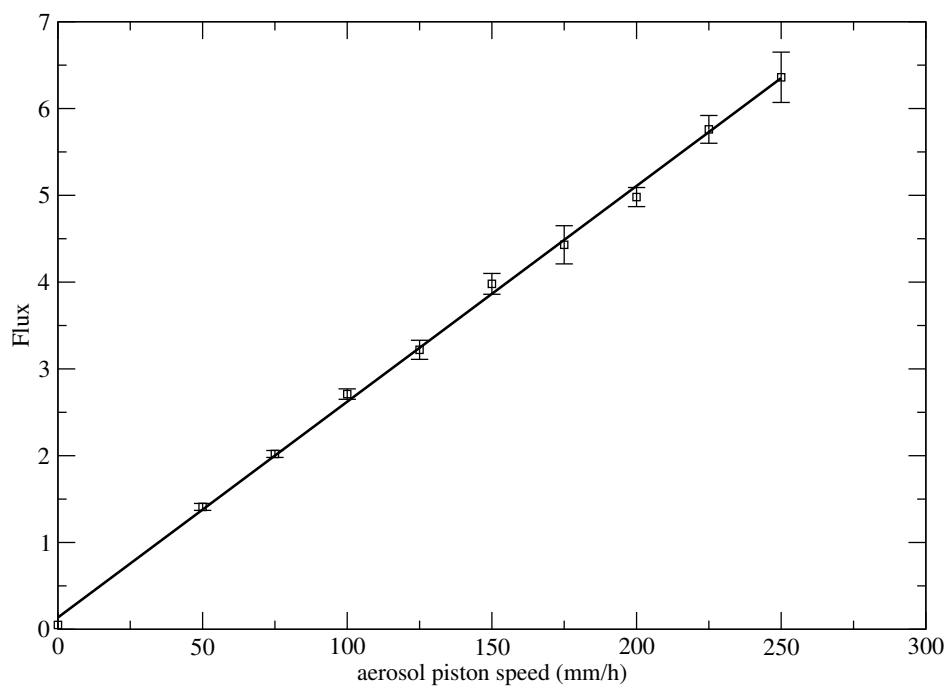
Figure 2.9: Flux of scattered light (in arbitrary units) versus piston speed for white clay particles. The detector is fixed at a scattering angle of 10° (Muñoz et al., 2011).
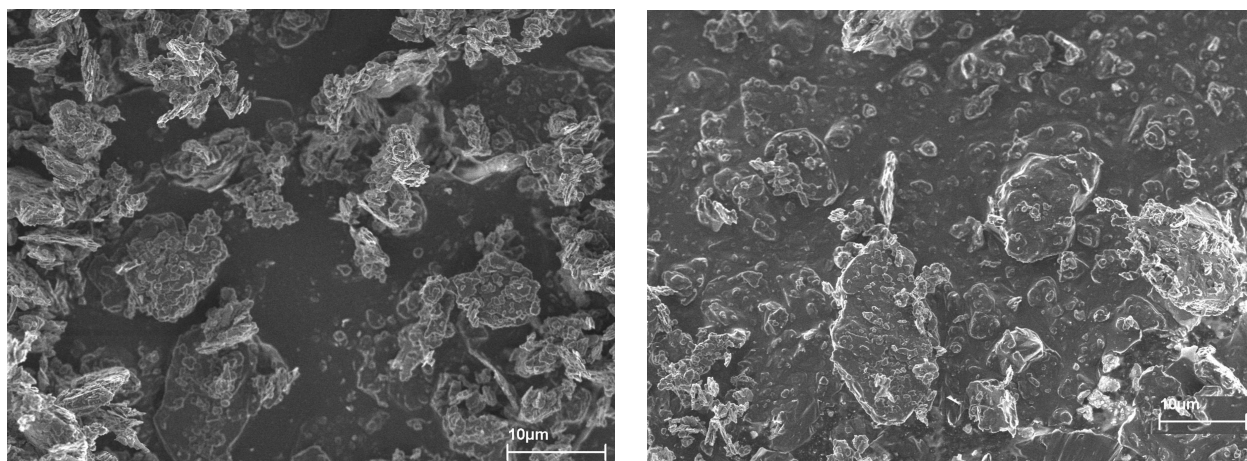

Figure 2.10: Field emission scanning electron microscope images of white clay particles. The left panel shows the particles before passing through the aerosol generator. The right panel is the sample gathered in the scattering volume where interacts with the laser, after passing the aerosol generator.

2.3.4 Cloude coherency matrix test.

One final test can be performed to check whether the measured scattering matrix is actually a phase matrix representative of a collection of particles. The scattering matrix $\mathbf{F}$ must be a sum of pure Mueller matrices. To check this, several type of tests have been proposed (see Hovenier et al., 2000, and references therein). Among these, the Cloude coherency matrix test has been thoroughly used as validity test for measured scattering matrices over the past three decades. The coherency matrix $\mathbf{T}$ is computed from $\mathbf{F}$ through linear transformations (Hovenier et al., 2004). This matrix $\mathbf{T}$ is always Hermitian, so its eigenvalues are real. If all four of these eigenvalues are non-negative and at least one of them is positive, then $\mathbf{F}$ is a sum of pure Mueller matrices, and the test is fulfilled.

2.4 Computer simulations: the SIRIS code.

As stated in the introduction chapter, the experimental data has been combined with computer simulations. The computational results shown in this thesis have been obtained using the SIRIS code. This code has been developed by the group of Prof. Karri Muinonen at University of Helsinki Muinonen et al. (2009).

There are many approaches to the computational problem as far as the definition of the shape is concerned. Spheres, ellipsoids, and cylinders have been profusely used because of their symmetry. Moreover, an ensemble of irregular particles can be defined by a few statistical parameters. The SIRIS code use Gaussian random shapes (GRS) to reproduce the irregularity of the particle. The code also allows to include wavelength size inhomogeneities to resemble internal and external features of the host particle as inclusions or surface roughness. In spherical coordinates, the GRS are described by a radius vector which is the exponential of a Gaussian random variable:

$$r(\vartheta, \phi)\mathbf{e}_r = \frac{a \exp[s(\vartheta, \phi)]}{\sqrt{1 + \sigma^2}}\mathbf{e}_r \tag{2.33}$$

$$s(\vartheta, \phi) = \sum_{l=0}^{\infty} \sum_{m=-l}^{l} s_{lm} Y_{lm}(\vartheta, \phi) \tag{2.34}$$

$$s_{l,-m} = (-1)^m s_{lm}^* \tag{2.35}$$

where $s(\vartheta, \phi)$ is the logarithmic radial distance, Y_{lm} are orthonormal spherical harmonics, and s_{lm} are Gaussian random variables with zero means. The parameters a and σ are the mean radius and relative standard deviation. The standard deviation of the Gaussian random variables s_{lm} follow the covariance function Σ_s which is given by a series of Legendre polynomials P_l. The degree l of these polynomials ranges from 0 to ∞, but in the code the series is truncated by $l_{\min}$ and $l_{\max}$. The greater the value of $l_{\min}$ and $l_{\max}$, the spikier the particle will be, reducing its sphericity accordingly. The two lowest degrees of l are special.

l=0 corresponds to a change in the mean radius a, so it does not affect the shape. l=1 is almost a pure translation, i.e. moves the center of the sphere with respect the origin and does not affect the shape unless σ is very large. The higher degree terms contribute mainly to the shape. Since these lowest values produce unrealistic results in some cases, the simulations presented in this thesis have a $l_{\min}$=2 and $l_{\max}$=11.

Another important concept to consider is the covariance function Σ_s. This covariance function describes the correlation of two (log)radii separated by an angle γ. The value of the correlation is in the range [-1,1]. A constant (unity) correlation function with respect to γ generates spheres, but if the value decrease intensely as γ increases, smaller-scale features can be described (i.e. spikier shapes will form). The correlation function C_s in this model can be expressed as a series expansion of Legendre polynomials P_l (Nousiainen et al., 2001):

$$\Sigma_s(\gamma) = \ln(\sigma^2 + 1)C_s(\gamma), \tag{2.36}$$

$$C_s(\gamma) = \sum_{l=0}^{\inf} c_l P_l(\cos\gamma), \tag{2.37}$$

$$\sum_{l=0}^{l_{max}} c_l \equiv 1 \tag{2.38}$$

where c_l are the Legendre polynomial's weights. The shapes considered in this thesis are similar to those presented in (Muñoz et al., 2007) from visual comparison of the SEM images. In the mentioned paper, the weights $c_l \propto l^{-\nu}$ where ν sets the power law of the covariance function and is fixed to 3.3. The variance parameter used in that work was $\sigma = 0.2$. In Figure 2.11 two examples of Gaussian random shapes is presented.

Once the shape is defined, the scattering study is performed using the ray-optics approximation. The particle size is characterized by the mean-radius size parameter $x = ka$, where k is the wave number. The SIRIS code has an optimal performance for particles in the geometric optics regime, i.e. x>10. The scattering computation is split in two: the forward diffraction (very small scattering angles) and the side- and back-scattering. For the diffraction part, the two-dimensional silhouette is computed for each sample shape, and the diffraction is then ensemble-averaged in the Kirchhoff approximation. For the remaining scattering angles, a Mueller matrix is related to each ray, and the reflection and refraction at the boundary surface are computed using Snell's law and Fresnel's reflection and refraction matrices. The entire history of the ray path is accounted for the scattering. Every time the ray changes its direction a new "chord" is accounted, and the code continues the computations until a maximum number of chords is reached or the ray is totally absorbed within the particle. For a more detailed explanation about how the SIRIS code works, see Muinonen et al. (1996).

In more recent versions of the code, the option of include wavelength sized inhomogeneities was implemented to mimic internal inclusions or surface roughness. These features
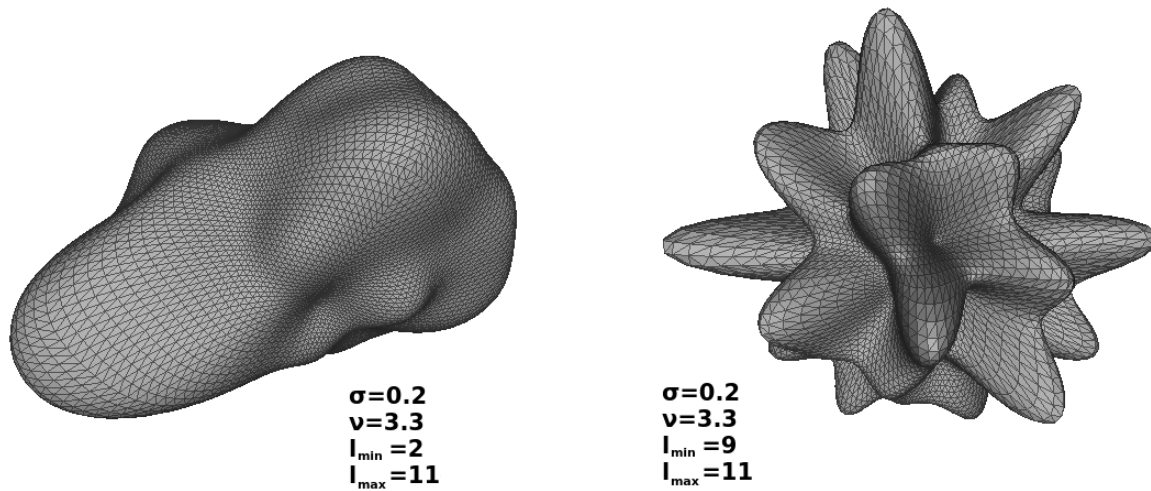
Figure 2.11: Gaussian random shapes generated by the SIRIS code. Left panel depicts a particle with the statistical values used in this thesis, i.e. ν=3.3, σ=0.2, $l_{\min}$=2, and $l_{\max}$=11. Right panels shows a spiky shape where the parameter $l_{\min}$=9.

are referred as diffuse internal medium (DIM) and diffuse external medium (DEM), respectively. Both DIM and DEM compositions may be characterized in different ways: if the inhomogeneities are suitable to use Rayleigh approximation (i.e., the scatterer is small compared to the wavelength), optical properties of the materials like the single scattering albedo and the extinction coefficient Q_{ext} are used. For larger inhomogeneities, a measured scattering matrix of the specific material may be used as input. These features allow to reproduce more realistic particles when computing the scattering matrices.

Chapter 3

Objectives

The motivation of this thesis is to characterize the spectropolarimetric response of the JSC-1A lunar dust sample for wavelengths in the optical range. The JSC-1A sample consists of dark irregular particles typically larger than the wavelength ($r_{eff} \sim 15$ μm). Since the lunar regolith has a composition mainly based in silicates, and similar composition can be found in other Solar System's objects, e.g. Mercury, Mars, or asteroids, this characterization might help in future research of these objects. In the past, some scattering properties of the lunar regolith have been measured independently, like the phase function or the polarimetry phase dependence, but to the author's knowledge, there are not any published values of the scattering matrix. Physical information of the sample can be obtained through this characterization due to the dependence of the scattering matrix with respect to the size distribution, shape, and refractive index. Other parameters to consider but not related to the sample are the polarization state of the incident light, the wavelength, and the scattering angle.

The physical properties of the sample affect simultaneously to all the scattering matrix elements, so the combination of physical parameters that produces a result might not be unique. Hence, it is usually difficult to test the dependence on a certain scattering matrix element of a given physical parameter. Electromagnetic scattering codes help in this respect. However, as the complexity of the particle grows (e.g. irregularity or complex structural features like tunnels, cavities, pores and surface roughness) the difficulty of modeling the scattering process increases. For this reason, the experimental measurements can be used as a test to verify the validity of the computational model.

The main objectives are pursued in this thesis through three papers:

- First, in the paper "Experimental scattering matrix for lunar regolith simulant JSC-1A at visible wavelengths" (Paper I hereafter) we aimed to characterize the JSC-1A lunar simulant sample through laboratory measurements of the scattering matrix. The experimental measurements were performed at optical wavelengths (488, 520 and 647 nm) for unpolarized incident light and random orientation of the particles. SEM images and size distribution parameters were also presented to describe the shape and size of

the particles studied. An extrapolated matrix was computed from the experimental measurements to cover the whole scattering angle range.

- Second, in the paper "Scattering properties of large irregular cosmic dust particles at visible wavelengths" (hereafter Paper II), we intended to distinguish between the physical properties that may be driving certain effects over the scattering matrix, e.g. changes in the maximum of the degree of linear polarization or a narrowing of the forward peak among others. A systematic study of the parameter space was carried out using the SIRIS3 code developed by Prof. Karri Muinonen at the University of Helsinki. The simulated particles included internal inclusions and surface roughness as wavelength-sized inhomogeneities, and their effects were studied both jointly and separately. Other parameters studied were particle size, imaginary part of the refractive index, and both densities and compositions of the internal inclusions and surface roughness.

- Third, in the paper "Simulations of effects of nanophase iron space weather products on lunar regolith reflectance spectra" (hereafter Paper III), we test the performance of the SIRIS3 code when trying to reproduce the effects of the space weathering over the reflectance spectra of a lunar regolith sample. The space weathering is produced by exposition to cosmic rays and meteoroid bombardment in airless bodies. This triggers a production of reduced iron inclusions in the regolith near the particle surface. The effects of these inclusions are easily spotted in the reflectance spectra as an increase of the spectral slope (reddening), a decrease of the intensity at all wavelengths (darkening) and subdued absorption bands. These effects were qualitatively well reproduced by the simulations using internal inclusions acting as the reduced iron nanoparticles.

Paper I: Experimental scattering matrix for lunar regolith simulant JSC-1A at visible wavelengths

EXPERIMENTAL SCATTERING MATRIX FOR LUNAR REGOLITH SIMULANT JSC-1A AT VISIBLE WAVELENGTHS.

J. Escobar-Cerezo[1], O. Muñoz[1], F. Moreno[1], D. Guirado[1], J.C. Gómez Martín [1], J.D. Goguen[2], E.J. Garboczi[3], A.N. Chiaramonti[3], T. Lafarge[4], R.A. West[2]

[1]Instituto de Astrofísica de Andalucía, CSIC, Glorieta de la Astronomía s/n, 18008 Granada, Spain.

[2]Jet Propulsion Laboratory, California Institute of Technology, 4800 Oak Grove Drive, Pasadena, CA 91109, United States.

[3]Applied Chemicals and Materials Division, Material Measurement Laboratory, National Institute of Standards and Technology, Boulder, CO, USA.

[4]Statistical Engineering Division, Information Technology Laboratory, National Institute of Standards and Technology, Gaithersburg, MD, USA.

ABSTRACT

We present the experimental scattering matrix as a function of the scattering angle of the lunar soil simulant JSC-1A. The measurements were performed at 488 nm, 520 nm, and 647 nm, covering the range of scattering angles from 3° to 177°. The effect of sub-micron size particles on the measured phase function and degree of linear polarization has been studied. After removing particles smaller than 1 µm radius the forward scattering peak becomes steeper. Further, the maximum of the degree of linear polarization increases, moving toward smaller scattering angles. Interestingly, the negative branch at backward direction disappears as the small particles are removed from the sample. As multiple scattering calculations with polarization included require single scattering matrices in the whole scattering range (from 0° to 180°), we computed the corresponding synthetic scattering matrix through an extrapolation method, considering theoretical boundary conditions. From the extrapolated results, the asymmetry parameter g and the back-scattering linear depolarization factor δ_L were computed.

Keywords: Experimental techniques, Moon, Polarimetry

1. INTRODUCTION.

The Moon is one of the most studied celestial bodies in astronomy. In this work we are interested in the polarimetric point of view of the subject. The first polarimetric studies of the Moon surface date back to Lyot (1929). More recently, there has been an increasing interest in polarimetric measurements since the work of Sterzik et al. (2012), who presented a new method to detect spectropolarimetric biosignatures in earth-like exoplanets. In that paper, the Moon surface was used as a mirror to extract biosignatures from the Earth's spectrum. In order to improve the accuracy of this method, the background signal produced by lunar regolith has to be characterized with precision to subtract it from the spectrum.

Apollo missions brought to Earth 382 kilograms of lunar samples between 1969 and 1972. In addition, some 300 grams of sample were returned from the Moon by Luna's automated missions. Due to the limited amount of lunar samples available to study, lunar simulants were developed to cover that need. In the early 1990s, a mare lunar regolith simulant called JSC-1 (Johnson Space Center-1, McKay et al. (1994)) was produced to support NASA's future lunar surface missions. This simulant was created to resemble as much as possible the composition and size distribution of lunar soil 14163 from the Apollo 14 mission. When this simulant ran out, NASA ordered a new simulant called JSC-1A, matching the JSC-1 simulant as closely as possible. This simulant has been studied from various points of view, but to our knowledge, its scattering matrix has never been measured.

In this work, we present the experimental scattering matrices as functions of the scattering angle of the JSC-1A lunar simulant at three visible wavelengths (488 nm, 520 nm, and 647 nm). These measurements were performed at the IAA COsmic DUst LABoratory (IAA-CODULAB) located at the Instituto de Astrofísica de Andalucía (Muñoz et al. 2010). The experimental apparatus is presented in Section 2. The description of the physical properties of

the JSC-1A samples is presented in Section 3. The lack of measurements at very small and very large scattering angles (0° to 3° and 177° to 180°) limits the applicability of the measured scattering matrices for multiple scattering calculations. Therefore, we extrapolate the experimental scattering matrices to cover the entire 0° to 180° angle range. The extrapolation of the components of the scattering matrix **F** was performed following the procedure presented by Liu et al. (2003) for the phase function and Muñoz et al. (2006) for the rest of the scattering elements. The asymmetry parameter g and the back-scattering linear depolarization factor $\delta_L(180°)$ were calculated from these extrapolated matrices. All these results are presented in Section 4. Conclusions are drawn in Section 5.

2. EXPERIMENTAL APPARATUS.

In this section, we give a brief description of the IAA-CODULAB apparatus. A detailed description of the experimental setup, including the calibration process and data acquisition, is presented in Muñoz et al. (2010). All published results are freely available at the Amsterdam-Granada light scattering database (http://www.iaa.es/scattering).

We use an Argon-Krypton laser that is tunable to five different wavelengths in the visible range. In this work, we present the results at 488 nm, 520 nm, and 647 nm as these wavelengths are sufficiently separated to obtain differences in the results, if they exist. The laser beam passes through an integrated polarizer and an electro-optic modulator, which in combination with lock-in amplifiers and an oscillator allows us to increase the accuracy of the measurements as well as determine several elements of the scattering matrix simultaneously. The laser beam is scattered by a cloud of particles produced by an aerosol generator. Two photomultipliers located in a one meter ring collect the signal. One of them, the monitor, is located in a fixed position to correct for fluctuations of the jet stream, while the other acts as a detector, moving from 3° to 177°. Two additional optical elements, a quarter-wave plate and an analyzer, are optionally placed in the detector photomultiplier. By using five different configurations of these optical elements, we measure the 4×4 scattering matrix, which has only six independent real elements when assuming mirror symmetry and randomly oriented particles in the sample (Hovenier et al. 2004),

$$\mathbf{F} = \begin{pmatrix} F_{11} & F_{12} & 0 & 0 \\ F_{12} & F_{22} & 0 & 0 \\ 0 & 0 & F_{33} & F_{34} \\ 0 & 0 & -F_{34} & F_{44} \end{pmatrix}. \tag{1}$$

The scattering matrix elements depend on the wavelength λ and on the particle size, shape distribution, and complex refractive index of the particles. The elements also depend on the scattering angle θ, which is the angle defined by the directions of the incident and scattered beams. All scattering elements $F_{ij}(\theta)$ are normalized to $F_{11}(\theta)$, except $F_{11}(\theta)$ itself, which is normalized to unity at 30°. The $F_{11}(\theta)$ element normalized in this way is called the phase function in this work. The $-F_{12}(\theta)/F_{11}(\theta)$ ratio is equivalent to the degree of linear polarization for unpolarized incident light.

From the $F_{22}(\theta)/F_{11}(\theta)$ ratio, we can compute the linear depolarization factor at back-scattering δ_L according to the equation (Mishchenko et al. 2002):

$$\delta_L = \frac{F_{11}(180°) - F_{22}(180°)}{F_{11}(180°) + F_{22}(180°)}. \tag{2}$$

The validity of the measurements has been tested by comparing spherical water droplet measurements with Lorenz-Mie computations for homogeneous spherical particles (Muñoz et al. 2010). Moreover, special tests have been carried out to test that our measurements are performed under single scattering conditions (Muñoz et al. 2011). Further, we checked that the measured scattering matrices fulfilled the Cloude coherence matrix test within the experimental errors at all measured scattering angles (Hovenier et al. 1986).

3. PHYSICAL PROPERTIES OF JSC-1A LUNAR SIMULANT.

As mentioned, the JSC-1A mare regolith simulant was produced to match the Apollo 14 sample 14163. In Table 1, we present a composition comparison between simulant JSC-1A and the Apollo 14 sample 14163. The JSC-1A material was mined from a commercial cinder quarry at Merriam Crater (35°20' N, 111°17' W), a volcanic cinder cone located in the San Francisco volcano field near Flagstaff, Arizona. No chemical processing was performed on the simulant.

3.1. *Size characterization.*

Constituent oxides	Apollo 14 sample 14163 (Papike et al. 1982)	JSC-1A (Ray et al. 2010)
SiO_2	47.3 %	45.7 %
Al_2O_3	17.8 %	16.2 %
CaO	11.4 %	10.0 %
FeO	10.5 %	-
Fe_2O_3	-	12.4 %
MgO	9.6 %	8.7 %
TiO_2	1.6 %	1.9 %
Na_2O	0.70 %	3.2 %
K_2O	0.55 %	0.8 %
MnO	0.135 %	0.2 %

Table 1. Composition in mass percentage (mass %) of the major constituents of the JSC-1A lunar simulant compared with the Apollo 14 sample 14163.

The original mined material from the cinder quarry was milled and sieved to approximate the finer component of lunar regolith, where an important percentage of grain sizes are below 20 µm. Before using the JSC-1A in our light scattering experiment, we removed the large grains by using a sieve with 140 µm grid width to avoid clogging the aerosol generator. The size distribution was then measured with a commercial particle sizer. This instrument measures the phase function of the sample at a wavelength of 632.8 nm at certain scattering angles, with special attention to the forward scattering peak. The angular patterns obtained of the phase function are compared to those simulated by the instrument software in order to retrieve the volume distribution that best fits the data. These simulations use either Lorenz-Mie (Mie 1908) or Fraunhofer diffraction theory (van de Hulst 1957) under the assumption of spherical particles to obtain numerical results. As these two methods are usually used by the astronomy community, we show here both results to be available. The Fraunhofer diffraction theory states that the diffraction pattern depends on the shape and size of the particle, but is independent of its composition and the nature of its surface. Because of this, the Fraunhofer approach does not require the refractive index as input to compute the volume distribution, but puts restrictions on the size of the particles since it is only applicable to particles larger than the wavelength of the incident light. In the Lorenz-Mie calculations, we used $m = 1.65 + i0.003$ as the complex refractive index (Goguen et al. 2010). From the estimated volume distribution, we compute the number distribution of the sample $n(r)$ such that $n(r)\mathrm{d}r$ is the relative number of spheres per unit volume in the size range r and $r + \mathrm{d}r$. The values of the effective radius r_{eff} and effective variance v_{eff} are computed accordingly to the equations (Hansen and Travis 1974):

$$r_{\mathrm{eff}} = \frac{\int_0^\infty r\pi r^2 n(r)\mathrm{d}r}{\int_0^\infty \pi r^2 n(r)\mathrm{d}r}, \tag{3}$$

$$v_{\mathrm{eff}} = \frac{\int_0^\infty (r - r_{\mathrm{eff}})^2 \pi r^2 n(r)\mathrm{d}r}{r_{\mathrm{eff}}^2 \int_0^\infty \pi r^2 n(r)\mathrm{d}r}. \tag{4}$$

In Table 2, we present the resulting values for our JSC-1A sample.

As mentioned, during the experiment the cloud of particles is located in a jet stream produced by an aerosol generator. In this way a sample container is not needed. This is very convenient since the container walls would produce reflections or stray light decreasing the accuracy of the measurements and limiting the angular range. A disadvantage of this method is that we need a continuous flow of particles during the measurements, requiring a sufficient amount of sample. The sample has to be discarded after being blown through the scattering volume. In an attempt to reduce this problem, we have used a dedicated pump in order to recover the JSC-1A sample and re-use it in subsequent measurements. To check how this recycling process changes the size distribution of the sample we have performed the following test: 17 g of the bulk JSC-1A sample was recycled twice. After one recovery cycle, the mass loss was 1.6 g, 9.4 % of the original mass. After the second recovery, the loss was significantly smaller, being 0.4 g, 2.6 % of the 15.4 g of the first recovered material. The size distribution of the recycled sample was measured after
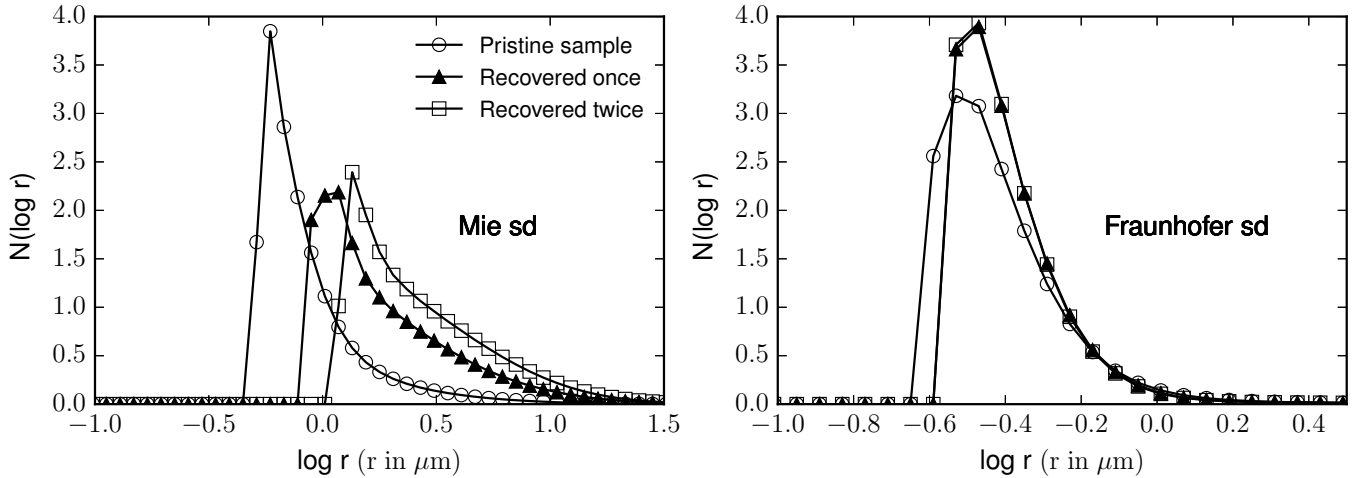
Figure 1. Number distribution $N(\log r)$ versus $\log r$ of the pristine lunar simulant JSC-1A (circles) and same samples after recovering once from the collecting system (triangles) and after two recoveries (squares). Retrievals based on Mie and Fraunhofer theories are presented in the left and right panels, respectively. The refractive index used in the Mie light scattering model is $m = 1.65 + i0.003$.

the first and second recoveries. The r_{eff} of the sample after the first recovery changed from 15.85 µm to 20.62 µm, an increase of 30 %. After the second recovery, the r_{eff} value was 21.86 µm, an increase of 6 % from 20.62 µm. Therefore, during the recovery process a high percentage of the small particle fraction is lost. This effect tends to saturate after the first recovery. With regard to the v_{eff}, this value varies from 1.28 for the pristine sample, to 1.06 for the sample recovered once and 1.05 for the sample recovered twice. The size distribution becomes narrower, but again this effect saturates. In Figure 1 and Table 2, we show a comparison between the number size distributions as function of $\log r$, $N(\log r)$, where $N(\log r)\mathrm{d}\log r$ can be defined as the relative number of spheres per unit volume in the size range $\log r$ and $\log r + \mathrm{d}\log r$. We present also in Figure 2 $S(\log r)$, which can be defined as the relative contribution to the total surface area of projected-surface-area-equivalent spheres of radius r as function of $\log r$. As the area under the curve is normalized to unity, we observe that the recovered sample has lost the contribution of the small particles to the size distribution.

| Sample	Mie		Fraunhofer	
	$r_{eff}(\mu m)$	v_{eff}	$r_{eff}(\mu m)$	v_{eff}
Pristine	15.85	1.28	10.50	1.69
Recovered once	20.63	1.06	13.80	1.42
Recovered twice	21.86	1.05	14.67	1.45

Table 2. Size distribution parameters r_{eff} and v_{eff} for the pristine sample, the sample after recovering once, and twice. The effective radius and variance based on Mie and Fraunhofer theories are presented in the second and third columns, respectively. For the Mie model, the refractive index used was $m = 1.65 + i0.003$ (Goguen et al. 2010).

3.2. *Shape characterization.*

A deep analysis of the JSC-1A particle shape was presented in Garboczi (2011), where X-ray computed tomography (X-ray CT) was used to characterize the simulant. In this work, we use the same techniques to describe our sample.

In Figure 3, we show X-ray CT images qualitatively showing the shape variation in the JSC-1A lunar simulant. To prepare samples, the particles of interest were mixed with epoxy and the mixture pulled into a narrow (3 mm diameter) plastic tube. Pieces of the tube were cut and used in the upright position as samples in one of two X-ray microCT instruments. For the image in Figure 3c, the epoxy-particle mixture was dripped on the outside of the same tube, to give a thinner sample. The thinner sample gave better images at this very high resolution than the regular samples.

Figure 3a is approximately 1.04 mm in width. Notice the air bubbles in some of the particles. Since JSC-1A has a volcanic origin, these must be the remnants of air bubbles that were entrained during the original lava flow. The large
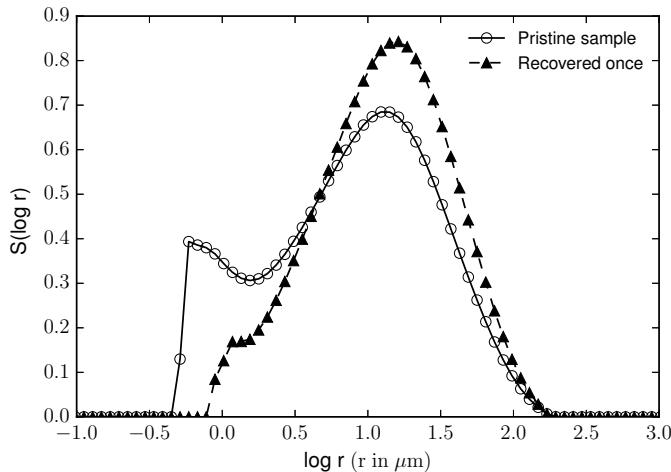
Figure 2. Projected-surface-area distribution $S(\log r)$ versus size logarithm $\log r$ of the pristine lunar simulant JSC-1A (circles) and same sample after recovering once from the collecting system (triangles). The Mie light scattering model has been used to compute the size distribution with a refractive index of $m = 1.65 + i0.003$ (Goguen et al. 2010). The cut slope seen for small sizes is an artifact produced by the retrieved data from the commercial particle sizer.

particle in the right of the image seems to be a conglomerate of large and small particles.

Figure 3b is approximately 1.12 mm in width. Note that Figure 3b is about the same physical size as Figure 3a, but the large particles have been eliminated by sieving through a 75 µm sieve and many of the smaller particles have been eliminated by sieving through a 20 µm sieve. Note the irregular, non-spherical shapes, typical of a ground rocky material.

Figure 3c is approximately 0.16 mm in width. As in the previous panel, the material used to make these images passed the 75 µm sieve and were retained on the 20 µm sieve. Again note the irregular, non-spherical shapes, typical of a ground rocky material. The particle at the left bottom corner (inside circle) is about 16 µm in width, in this cross-section.

In Figure 4, we show four scanning electron microscope (SEM) images of the JSC-1A sample. Figures 4a and 4c correspond to the pristine sample, while Figures 4b and 4d correspond to the recovered sample from the pump.

The angularity of the shape is a common feature at all sizes. As can be seen, the irregularity is the norm. In general, the particles also seem somewhat glassy and faceted, as might be expected from ground volcanic material. Another sign of the volcanic origin of the sample can be perceived in the three central particles in Figure 4c, where traces of enclosed gas bubbles can be seen in the surface of those particles. In Figure 4a, we can see some very small particles clinging to the larger particle surfaces. It is probable that these small particles are only clinging through electrostatic forces. The particles show a very soft and almost featureless surfaces. In Figure 4b, we show some particles about 15 µm in radius, which is the characteristic size of this sample as presented above. Qualitatively, based on these admittedly small amount of particles, we can affirm that particle shape is roughly invariant with respect to particle size. This has been seen before for crushed natural particles (Garboczi et al. 2012), albeit at a somewhat larger size scale. Figures 4c and 4d have a similar magnification, so here we can observe the difference between the pristine and the recovered sample. In Figure 4c, the very small particles seem to be more abundant than in Figure 4d, which is consistent with the size distribution r_{eff} values presented in Table 2.

4. EXPERIMENTAL SCATTERING MATRIX.

In Figure 5, we present the experimental scattering matrix elements as functions of the scattering angle at three different wavelengths (488 nm, 520 nm, and 647 nm). The measurements cover the scattering angle range from $3°$ to $177°$. The ratios $F_{13}(\theta)/F_{11}(\theta)$, $F_{14}(\theta)/F_{11}(\theta)$, $F_{23}(\theta)/F_{11}(\theta)$ and $F_{24}(\theta)/F_{11}(\theta)$ are not represented since they were found to be zero over the entire angle range within the accuracy of the measurements (as expected by Eq. 1). The experimental errors are represented as error bars (note that some error bars are smaller than the symbol itself). The main source of noise is the statistical variation of the number of large particles passing through the scattering volume, resulting in a smaller signal-to-noise ratio.

The $F_{11}(\theta)/F_{11}(30°)$ ratio, which we have previously defined as the phase function, shows the usual behaviour of large irregular mineral dust, i.e. a strong forward peak and almost no structure at side- and back-scattering, as shown
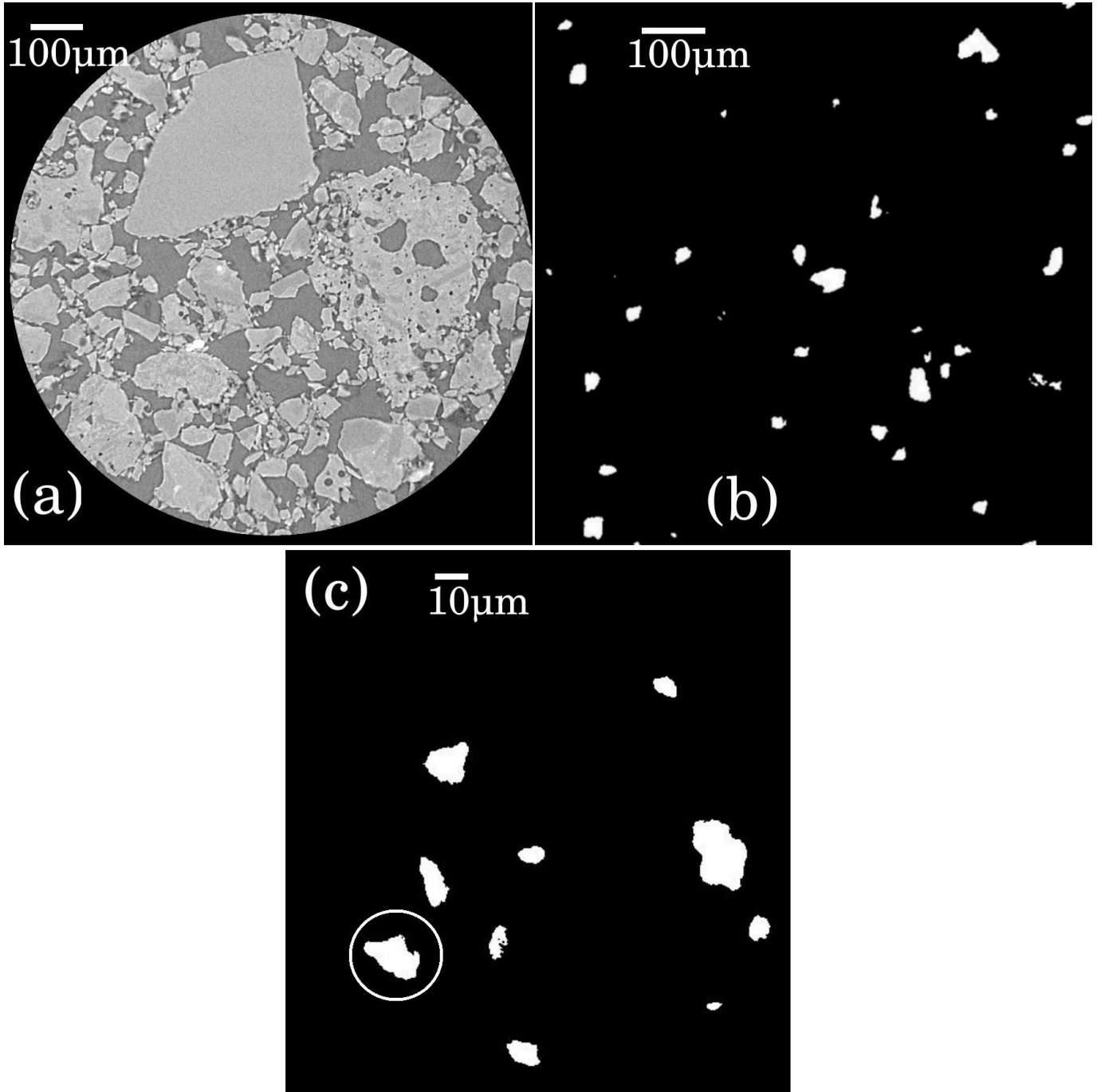
Figure 3. X-ray CT images of the JSC-1A sample. The particles were mixed with epoxy and introduced in a 3 mm diameter tube before cutting into slices. Panel (a) depicts the bulk sample, as no sieving was performed. Panel (b) shows particles in the size range of 20 µm to 75 µm after removing larger and smaller particles through sieving. Panel (c) shows the same population as (b), but with larger magnification.

in Fig. 5a. The forward diffraction peak can be used to characterize the mean size of the particles as it increases as the particle size grows (Liu et al. 2003). We do not observe any significant difference in the measured values of $F_{11}(\theta)/F_{11}(30°)$ with the wavelength. As stated above, the scattering elements depends mainly on size, shape and refractive index of the sample. The lack of differences between wavelengths is indicative of a flat dependence of the imaginary part of the refractive index with the wavelength. Also the relative size to the wavelength does not significantly change at the measured wavelengths. We have to take into account that some minor differences in the phase function may appear between wavelengths, but the logarithmic representation and the arbitrary normalization to unity at 30 degrees may mask these differences.
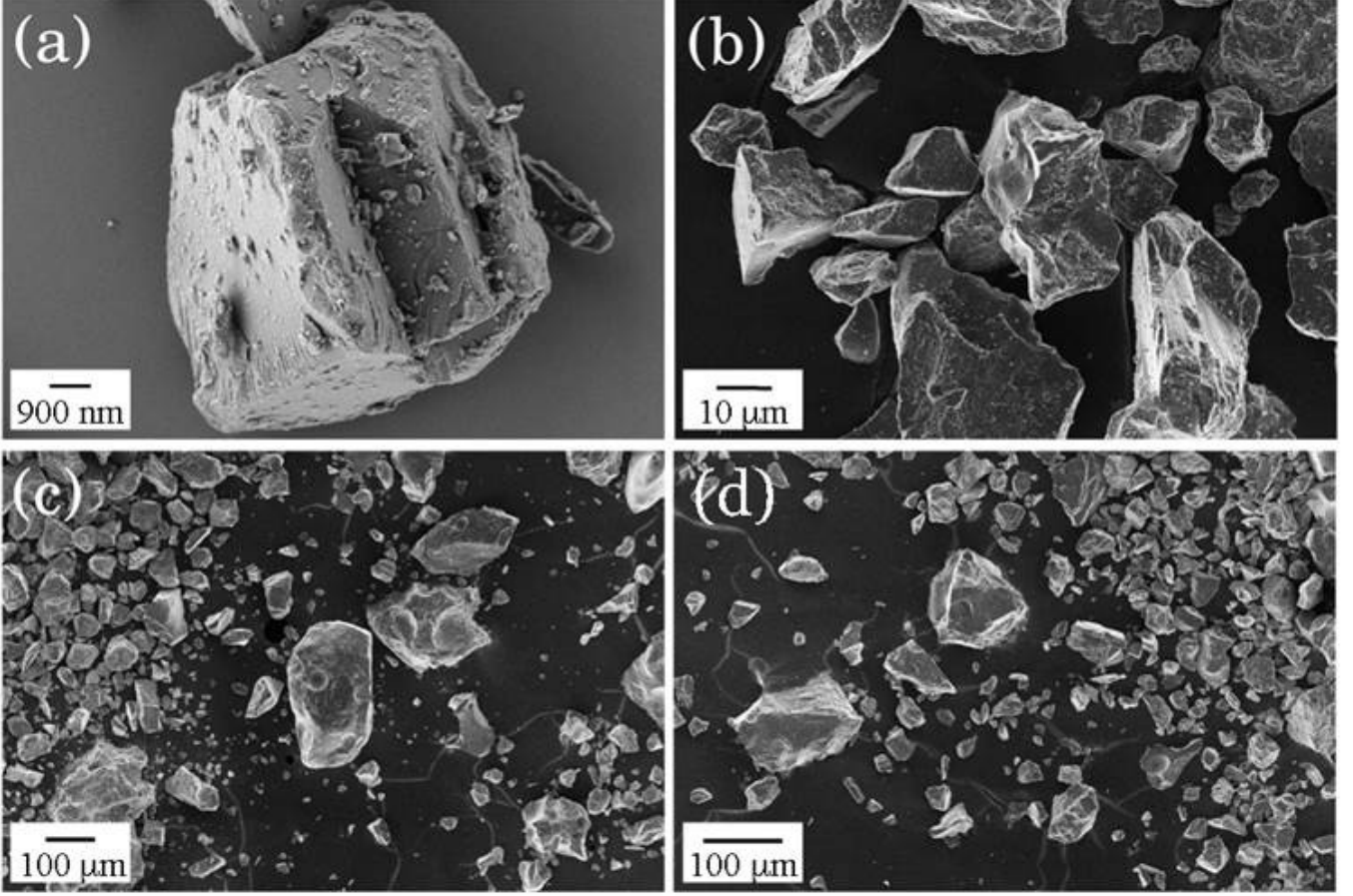
Figure 4. Scanning electron microscope images of the JSC-1A pristine sample and recovered from the jet pump. Panels (a) and (c) correspond to the pristine sample, and panels (b) and (d) correspond to the recovered sample.

The $-F_{12}(\theta)/F_{11}(\theta)$ ratio, shown in Fig. 5b, equals the degree of linear polarization for unpolarized incident light. This plot presents the typical bell shape for irregular particles randomly oriented (Muñoz et al. 2012), with a maximum of polarization near 90° and a small inversion branch at back-scattering (~ 2 % of negative polarization). The maximum of the degree of linear polarization shows slightly larger values at 647 nm than at 488 nm, i.e. it presents a red polarization color. This has been observed consistently in our database in silicate-type particles when the imaginary part of the refractive index has a constant dependence on the wavelength (see e.g. Muñoz et al. 2012; Dabrowska et al. 2015).

The $F_{22}(\theta)/F_{11}(\theta)$ ratio, shown in Fig. 5c, is commonly used as a proof of the non-sphericity of the particles, since this ratio equals unity at all scattering angles for optically inactive spheres. The JSC-1A sample shows a $F_{22}(\theta)/F_{11}(\theta)$ ratio different from unity at nearly all measured scattering angles. The depolarization factor (Eq. 2) also depends on this ratio. No significant differences are found between the studied wavelengths.

The $F_{33}(\theta)/F_{11}(\theta)$ and $F_{44}(\theta)/F_{11}(\theta)$ ratios, shown in Fig. 5d and 5f respectively, can be studied jointly also as a sign of non-sphericity, indicating irregular particles when they are different from each other (Mishchenko et al. 2000). The measured $F_{44}(\theta)/F_{11}(\theta)$ ratio for the JSC-1A sample is larger than the $F_{33}(\theta)/F_{11}(\theta)$ ratio in the $\sim 75°$ to 177° scattering angle range, while in the case of homogeneous spherical particles the $F_{33}(\theta)/F_{11}(\theta)$ ratio is equal to the $F_{44}(\theta)/F_{11}(\theta)$ ratio at all scattering angles. The $F_{34}(\theta)/F_{11}(\theta)$ ratio, shown in Fig. 5e, shows the strongest wavelength dependence of all measured scattering matrix elements.

We have studied the effect of the loss of small particles on the scattering matrix elements. Due to limited amount of recycled sample, we have only measured the $F_{11}(\theta)$, $-F_{12}(\theta)/F_{11}(\theta)$ and $F_{22}(\theta)/F_{11}(\theta)$ ratios at 520 nm. In Figure 6, we present the latter scattering elements for the pristine sample and the JSC-1A simulant after one recovery. As stated
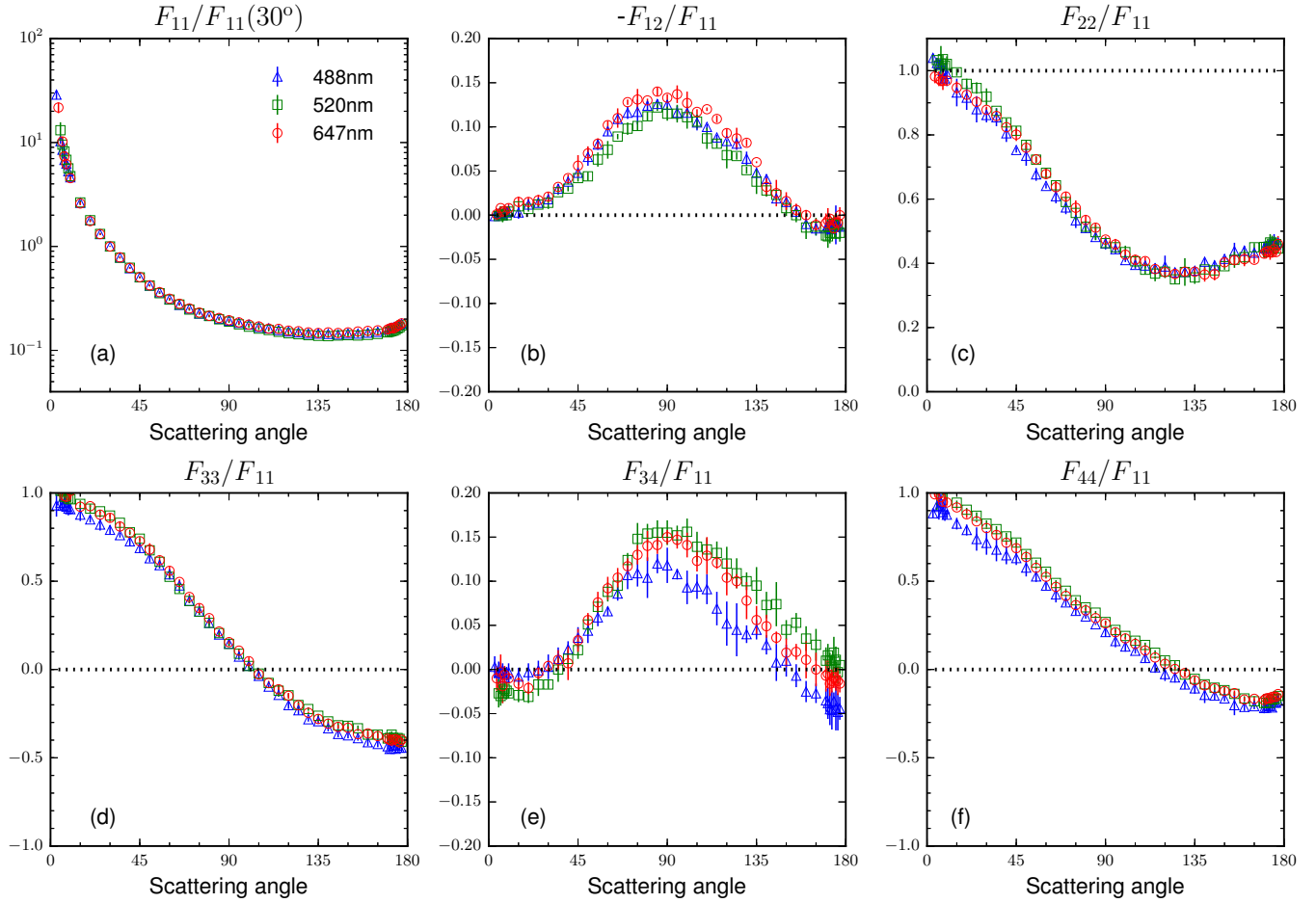
Figure 5. Experimental scattering matrix for lunar simulant JSC-1A at three different wavelengths (488 nm, 520 nm and 647 nm).
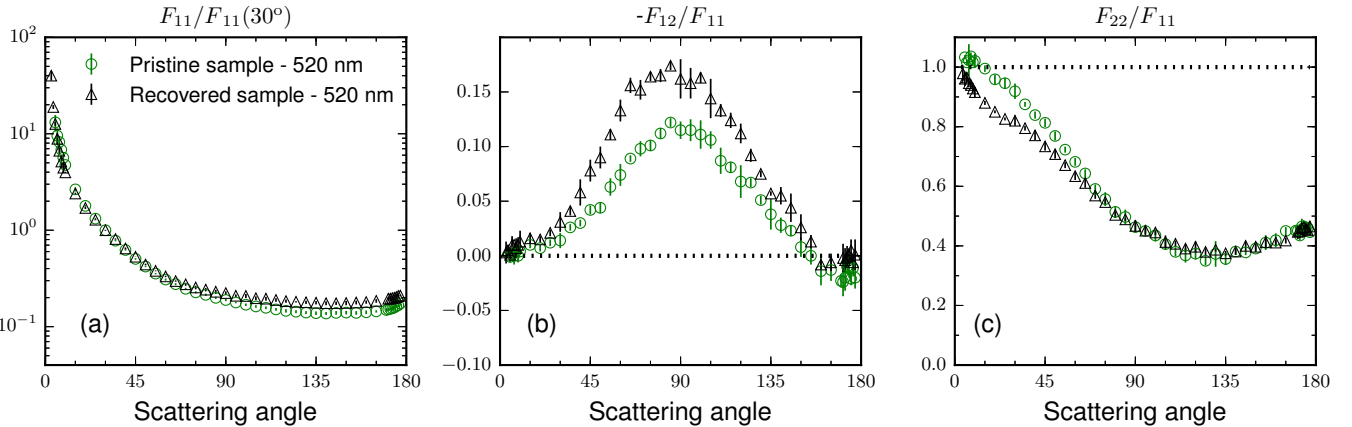
Figure 6. The $F_{11}(\theta)/F_{11}(30°)$, $-F_{12}(\theta)/F_{11}(\theta)$ and $F_{22}(\theta)/F_{11}(\theta)$ experimental scattering ratios for lunar simulant JSC-1A after recovery it once from the pump. The measurements were performed at 520 nm.

above, the smaller particles of the sample are depleted during the collecting process. The effect of this depletion on the scattering matrix is noticeable. In the phase function in Fig. 6a, we observe an increase of the forward scattering peak. This is expected as this diffraction peak depends on the particle size, being steeper for larger particles. The maximum of the degree of linear polarization increases by a factor of 1.5. Moreover, the maximum is moved toward smaller scattering angles. Apparently the small particle fraction was determining the maximum of the degree of

linear polarization. This is consistent with simulations presented in Liu et al. (2015) for Gaussian random shapes. In those simulations, as the mean size parameter of the particles grows, the resonance scattering region moves into the geometric optics regime, where the maximum in the ratio $-F_{12}(\theta)/F_{11}(\theta)$ increases as the size of the particles increases. Therefore, the small particles are limiting the maximum of the degree of linear polarization. Another interesting feature observed in our results is that the negative polarization branch nearly disappears for the recovered sample. The $F_{22}(\theta)/F_{11}(\theta)$ ratio, shown in Fig. 6c, varies slightly at small scattering angles, but is unaffected at back-scattering, so the depolarization ratio is not altered by the particle recovery process.

4.1. Synthetic scattering matrix.

As mentioned in Section 2, the laboratory measurements do not cover the whole scattering angle range from $0°$ to $180°$. The lack of measurements at forward and back-scattering angles limits the use of the measured scattering matrix data for radiative transfer calculations. To facilitate the use of our experimental data we compute the so-called synthetic scattering matrix $\mathbf{F}^{\mathrm{syn}}$ from our measurements. This matrix is defined in the full scattering angle range. Therefore, what we measure in the laboratory is the relative phase function $F_{11}(\theta)/F_{11}(30°)$, where (see Volten et al. (2006)):

$$\frac{F_{11}(\theta)}{F_{11}(30°)} = \frac{F_{11}^{\mathrm{syn}}(\theta)}{F_{11}^{\mathrm{syn}}(30°)}, \tag{5}$$

and $F_{11}^{\mathrm{syn}}(\theta)$ is the synthetic phase function, which is normalized according to Eq. 6:

$$\frac{1}{2} \int_0^\pi \mathrm{d}\theta \sin\theta F_{11}^{\mathrm{syn}}(\theta) = 1. \tag{6}$$

The synthetic phase function $F_{11}^{\mathrm{syn}}(\theta)$ covers all the scattering angles from $0°$ to $180°$. The extrapolation of the $F_{11}^{\mathrm{syn}}(\theta)$ element is computed as follows:

- The forward diffraction peak ($0°$-$3°$) is computed based on the assumption that the forward diffraction peak for randomly oriented particles with moderate aspect ratios mainly depends on the size of the particles and is only weakly dependent of their shape (Liu et al. 2003). We use the Lorenz-Mie theory to compute the scattering produced by projected-surface-area equivalent spheres between $0°$ and $3°$. These computations depends on the size distribution and the refractive index of the sample. For the refractive index, we use $m = 1.65 + i0.003$ (Goguen et al. 2010), while the size distributions are those presented in Section 3 (Table 2).

- Back-scattering extrapolation at $180°$ is performed using the least squares method for a quadratic function using the measured data from $150°$ to $177°$. As the scattering of random oriented irregular particles must be symmetric with respect to the forward and backward directions, the first derivative for all the scattering elements must be null at $0°$ and $180°$ (Hovenier and Guirado 2014). The back-scattering is reproduced with a cubic spline interpolation between the last measured data point ($177°$) and the extrapolated $F_{11}^{\mathrm{syn}}(180°)$ value, taking into account the null derivative condition.

- At this point, we have a data function given by the measured data from $3°$ to $177°$ and extrapolated data from $177°$ to $180°$. This function is shifted vertically until the value of $F_{11}^{\mathrm{syn}}(3°)$, as computed by Lorenz-Mie theory, matches the measured value of $F_{11}(3°)$.

The normalization condition given by Eq. 6 is then checked. If it is not satisfied within a 0.1 % accuracy, the value of $F_{11}(3°)$ is increased or decreased (within the experimental error bars) depending on whether the integral is greater or smaller than unity, and the three step process is repeated.

The other missing values of the $\mathbf{F}^{\mathrm{syn}}$ matrix elements are interpolated considering the well-known set of constraints of scattering matrices at forward and backward scattering (Hovenier et al. 2004):

$$\frac{F_{12}^{\mathrm{syn}}(0)}{F_{11}^{\mathrm{syn}}(0)} = \frac{F_{12}^{\mathrm{syn}}(180°)}{F_{11}^{\mathrm{syn}}(180°)} = \frac{F_{34}^{\mathrm{syn}}(0)}{F_{11}^{\mathrm{syn}}(0)} = \frac{F_{34}^{\mathrm{syn}}(180°)}{F_{11}^{\mathrm{syn}}(180°)} = 0, \tag{7}$$

$$\frac{F_{22}^{\mathrm{syn}}(0)}{F_{11}^{\mathrm{syn}}(0)} = \frac{F_{33}^{\mathrm{syn}}(0)}{F_{11}^{\mathrm{syn}}(0)} = 1, \tag{8}$$

$$\frac{F_{22}^{\mathrm{syn}}(180°)}{F_{11}^{\mathrm{syn}}(180°)} = -\frac{F_{33}^{\mathrm{syn}}(180°)}{F_{11}^{\mathrm{syn}}(180°)}, \tag{9}$$
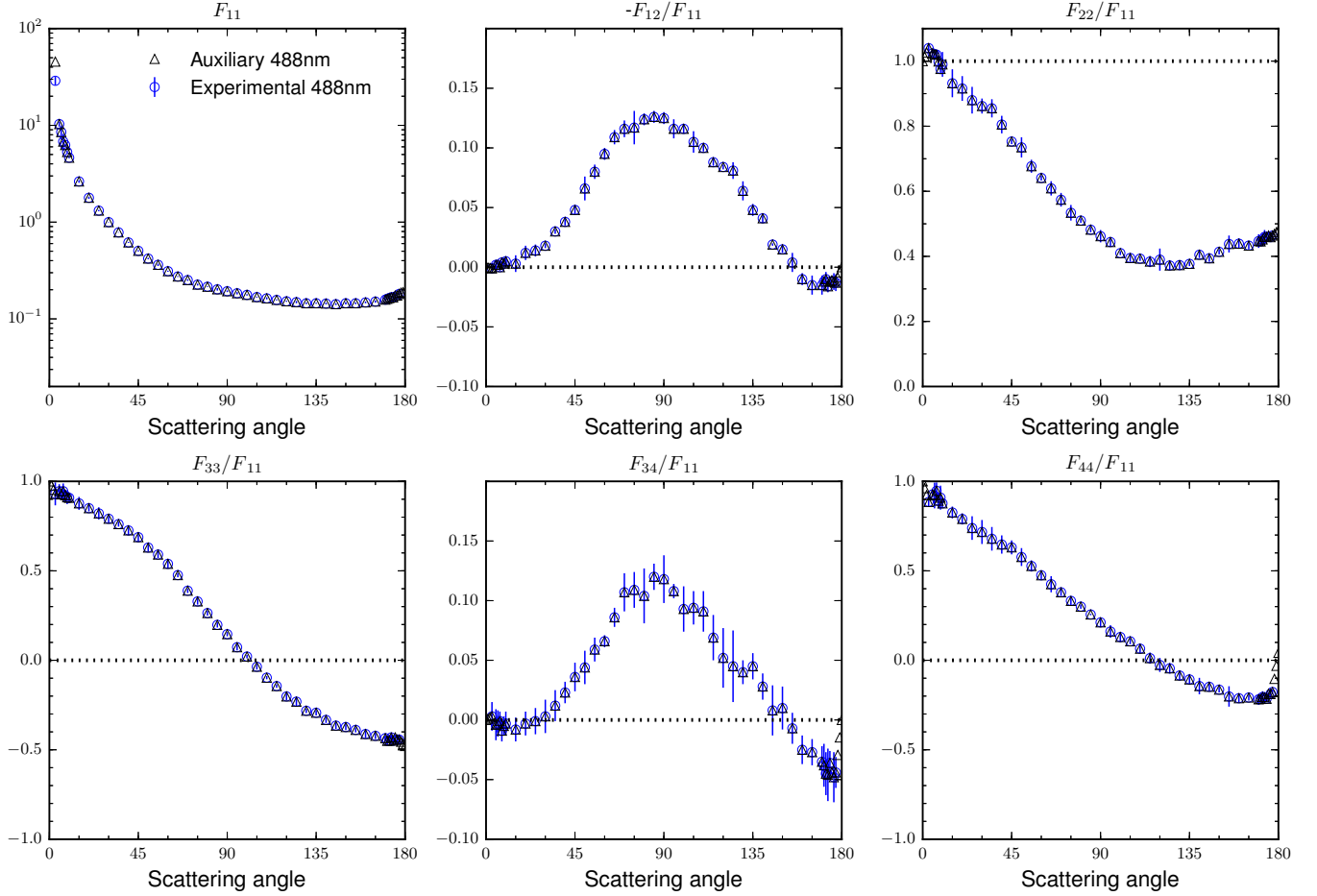
Figure 7. Comparison between the experimental scattering matrix of the JSC-1A lunar simulant at 488 nm (circles) and the extrapolated matrix (triangles). Note that measured $F_{11}(\theta)$ is normalized to unity at 30° whereas extrapolated $F_{11}^{\text{syn}}(\theta)$ is normalized so that its average over all directions equals unity.

$$\frac{F_{44}^{\text{syn}}(180°)}{F_{11}^{\text{syn}}(180°)} = 1 - 2\frac{F_{22}^{\text{syn}}(180°)}{F_{11}^{\text{syn}}(180°)}. \tag{10}$$

Only the value of $F_{22}^{\text{syn}}(180°)/F_{11}^{\text{syn}}(180°)$ must be extrapolated, using the same method as the $F_{11}^{\text{syn}}(180°)$ value explained above. In Figure 7, we present the results of this extrapolation for λ=488 nm. Note that measured $F_{11}(\theta)$ is normalized to unity at 30° whereas extrapolated $F_{11}^{\text{syn}}(\theta)$ is normalized so that its average over all directions equals unity, as stated in Eq. 6. Also, the $F_{34}(\theta)/F_{11}(\theta)$ ratio should tend to zero at back-scattering, but there is a gap between the last measured scattering angle and the back-scattering direction. This small disagreement could be due to a slight disadjustment in the V_{DC} during the measurement. Also, we see a step in the $F_{44}(\theta)/F_{11}(\theta)$ ratio. This is probably an artifact of the extrapolation, as this ratio depends on other scattering elements according to Eq. 10, so the error inherent to the extrapolations of $F_{11}(180°)$ and $F_{22}(180°)/F_{11}(180°)$ is affecting this result.

The asymmetry parameter g is calculated from the extrapolated phase function using:

$$g = \int_0^\pi d\theta \sin\theta \cos\theta F_{11}^{\text{syn}}(\theta). \tag{11}$$

The values of g are presented in Table 3. They are classified depending on the size distribution model used in the extrapolation of $F_{11}^{\text{syn}}(\theta)$ (Mie or Fraunhofer) and for the three visible wavelengths used.

In Table 4, we present the computed depolarization factor $\delta_L(180°)$ using Eq. 2. The results are classified according to the wavelength and the light scattering model used in the extrapolation.

5. CONCLUSIONS.

Asymmetry parameter g		
Wavelength λ	Mie	Fraunhofer
488 nm	0.74	0.57
520 nm	0.75	0.60
647 nm	0.74	0.59

Table 3. Asymmetry parameter g for the JSC-1A lunar simulant retrieved from the extrapolated phase function $F_{11}^{\mathrm{syn}}(\theta)$. The results are presented according to the light scattering model used in the extrapolation (Mie or Fraunhofer) and depending on the wavelength (488 nm, 520 nm and 647 nm).

Back-scattering depolarization factor $\delta_L(180°)$		
Wavelength λ	Mie	Fraunhofer
488 nm	0.35	0.35
520 nm	0.42	0.42
647 nm	0.31	0.31

Table 4. Back-scattering depolarization factor $\delta_L(180°)$ for the JSC-1A lunar simulant retrieved from Eq. 2 and the extrapolated $F_{22}^{\mathrm{syn}}(180°)$. The results are presented according to the light scattering model used in the extrapolation (Mie or Fraunhofer) and depending on the wavelength (488 nm, 520 nm, and 647 nm).

We presented the 4×4 experimental scattering matrices for the lunar simulant JSC-1A at three visible wavelengths (488 nm, 520 nm, and 647 nm). The data were extrapolated at forward and back-scattering to obtain the synthetic matrices that cover the whole scattering range from $0°$ to $180°$. The size distribution of the sample was also measured for the pristine sample and after being recovered twice from the collecting device to study the size-selection effect. Tables of the measured and synthetic scattering matrices are available in the Amsterdam–Granada Light Scattering Database (www.iaa.es/scattering). The data are freely available under citation request of this paper and (Muñoz et al. 2012).

In general, the experimental matrices were very similar at all the studied wavelengths. The results show a behaviour typical for mineral dust. The $-F_{12}(\theta)/F_{11}(\theta)$ ratio shows a red polarization color. This seems to indicate a nearly constant value of the imaginary part of the refractive index at the measured wavelengths (see e.g. Muñoz et al. 2012; Dabrowska et al. 2015).

The measured data were extrapolated at forward and back-scattering, and the asymmetry parameter g and back-scattering linear depolarization factor δ_L were computed from this synthetic matrices. The retrieved linear depolarization ratio varies with wavelength, obtaining values of 0.35, 0.42 and 0.31 at 488 nm, 520 nm, and 647 nm, respectively.

The effect of removing particles smaller than 1 µm in radius on the measured $F_{11}(\theta)$, $-F_{12}(\theta)/F_{11}(\theta)$ and $F_{22}(\theta)/F_{11}(\theta)$ ratios was studied. As the small particles were depleted from the sample due to the filters in the pump system, the forward scattering peak of the phase function became steeper. Further, the maximum of the degree of linear polarization maximum increased, moving toward smaller scattering angles. The negative polarization branch at large scattering angles nearly disappeared after removing the sub-micron fraction from the sample. The $F_{22}(\theta)/F_{11}(\theta)$ ratio was slightly affected in the forward direction and unaffected in back-scattering.

As future work, it would be interesting to study highland simulants as the MLS-1 (Weiblen et al. 1990) to compare with the results presented here. The final step on these studies would be to measure the scattering matrix of a lunar regolith sample to verify the suitability of these simulants as opto-polarimetric replicas of the Moon surface's dust.

REFERENCES

D. D. Dabrowska, O. Muñoz, F. Moreno, J. L. Ramos, J. Martínez-Frías, and G. Wurm. Scattering matrices of martian dust analogs at 488 nm and 647 nm. *Icarus*, 250: 83–94, April 2015. doi:10.1016/j.icarus.2014.11.024.

E. J. Garboczi. Three dimensional shape analysis of JSC-1A simulated lunar regolith particles. *Powder Technology*, 207: 96–103, 2011.

E. J. Garboczi, X. Liu, and M. A. Taylor. The Shape of a Blasted and Crushed Rock Material over More than Three Orders of Magnitude: 20 mm to 60 mm. *Powder Technology*, 229:84–89, 2012.

J. D. Goguen, T. C. Stone, H. H. Kieffer, and B. J. Buratti. A new look at photometry of the Moon. *Icarus*, 208:548–557, August 2010. doi:10.1016/j.icarus.2010.03.025.

J. E. Hansen and L. D. Travis. Light scattering in planetary atmospheres. *SSRv*, 16:527–610, October 1974. doi:10.1007/BF00168069.

J. W. Hovenier and D. Guirado. Zero slopes of the scattering function and scattering matrix for strict forward and backward scattering by mirror symmetric collections of randomly oriented particles. *JQSRT*, 133:596–602, 2014.

J. W. Hovenier, H. C. van de Hulst, and C. V. M. van der Mee. Conditions for the elements of the scattering matrix. *A&A*, 157:301–310, March 1986.

J. W. Hovenier, C. Van Der Mee, and H. Domke. *Transfer of polarized light in planetary atmospheres : basic concepts and practical methods*, volume 318 of *Astrophysics and Space Science Library*. Springer Netherlands, 2004. doi:10.1007/978-1-4020-2856-4.

J. Liu, P. Yang, and K. Muinonen. Dust-aerosol optical modeling with Gaussian spheres: Combined invariant-imbedding T-matrix and geometric-optics approach. *JQSRT*, 161:136–144, 2015.

L. Liu, M. I. Mishchenko, J. W. Hovenier, H. Volten, and O. Muñoz. Scattering matrix of quartz aerosols: comparison and synthesis of laboratory and Lorenz-Mie results. *JQSRT*, 79:911–920, 2003. doi:10.1016/S0022-4073(02)00328-X.

B. Lyot. Recherches sur la polarisation de la lumière des planètes et de quelques substances terrestres. *Annales de l'Observatoire de Paris, section de Meudon*, 8:1–161, 1929.

D. S. McKay, J. L. Carter, W. W. Boles, C. C. Allen, and J. H. Alton. Jsc-1: a new lunar soil simulant. page 857, 1994.

G. Mie. Beiträge zur Optik trüber Medien, speziell kolloidaler Metallösungen. *Annalen der Physik*, 330:377–445, 1908. doi:10.1002/andp.19083300302.

M. I. Mishchenko, W. J. Wiscombe, J. W. Hovenier, and L. D. Travis. Overview of Scattering by Nonspherical Particles. In M. I. Mishchenko, J. W. Hovenier, and L. D. Travis, editors, *Light Scattering by Nonspherical Particles : Theory, Measurements, and Applications*, page 30. Academic Press, January 2000.

M. I. Mishchenko, L. D. Travis, and A. A. Lacis. *Scattering, absorption, and emission of light by small particles*. Cambridge University Press, 2002.

O. Muñoz, H. Volten, J. W. Hovenier, M. Min, Y. G. Shkuratov, J. P. Jalava, W. J. van der Zande, and L. B. F. M. Waters. Experimental and computational study of light scattering by irregular particles with extreme refractive indices: hematite and rutile. *A&A*, 446:525–535, February 2006. doi:10.1051/0004-6361:20053727.

O. Muñoz, F. Moreno, D. Guirado, J. L. Ramos, A. López, F. Girela, J. M. Jerónimo, L. P. Costillo, and I. Bustamante. Experimental determination of scattering matrices of dust particles at visible wavelengths: The IAA light scattering apparatus. *JQSRT*, 111:187–196, January 2010. doi:10.1016/j.jqsrt.2009.06.011.

O. Muñoz, F. Moreno, D. Guirado, J. L. Ramos, H. Volten, and J. W. Hovenier. The IAA cosmic dust laboratory: Experimental scattering matrices of clay particles. *Icarus*, 211:894–900, January 2011. doi:10.1016/j.icarus.2010.10.027.

O. Muñoz, F. Moreno, D. Guirado, D. D. Dabrowska, H. Volten, and J. W. Hovenier. The Amsterdam-Granada Light Scattering Database. *JQSRT*, 113:565–574, February 2012. doi:10.1016/j.jqsrt.2012.01.014.

J. J. Papike, S. B. Simon, and J. C. Laul. The lunar regolith - Chemistry, mineralogy, and petrology. *Reviews of Geophysics and Space Physics*, 20:761–826, November 1982. doi:10.1029/RG020i004p00761.

C. S. Ray, S. T. Reis, S. Sen, and J. S. O'Dell. JSC-1A lunar soil simulant: Characterization, glass formation, and selected glass properties. *Journal of Non-Crystalline Solids*, 356: 2369–2374, October 2010.

M. F. Sterzik, S. Bagnulo, and E. Palle. Biosignatures as revealed by spectropolarimetry of Earthshine. *Nature*, 483: 64–66, March 2012. doi:10.1038/nature10778.

H. C. van de Hulst. *Light Scattering by Small Particles*. John Wiley & Sons, 1957.

H. Volten, O. Muñoz, J. W. Hovenier, and L. B. F. M. Waters. An update of the Amsterdam Light Scattering Database. *JQSRT*, 100:437–443, July 2006. doi:10.1016/j.jqsrt.2005.11.055.

P. W. Weiblen, M. J. Murawa, and K. J. Reid. Preparation of simulants for lunar surface materials. In *Engineering, Construction and Operations in Space II*, pages 428–435. American Society of Civil Engineers, New York, 1990.

Paper II: Scattering properties of large irregular cosmic dust particles at visible wavelengths

SCATTERING PROPERTIES OF LARGE IRREGULAR COSMIC DUST PARTICLES AT VISIBLE WAVELENGTHS

J. ESCOBAR-CEREZO[1], C. PALMER[1], O. MUÑOZ[1], F. MORENO[1], A. PENTTILÄ[2], K. MUINONEN[2,3]

[1]Instituto de Astrofísica de Andalucía, CSIC, Glorieta de la Astronomía s/n, 18008 Granada, Spain.
[2]Department of Physics, P.O. Box 64, 00014 University of Helsinki (Finland)
[3]National Land Survey of Finland, Finnish Geospatial Reseach Institute, P.O. Box 84, 00521 Helsinki (Finland)

ABSTRACT

The effect of internal inhomogeneities and surface roughness on the scattering behaviour of large cosmic dust particles is studied by comparison of model simulations with laboratory measurements. The present work shows the results of an attempt to model a dust sample measured in laboratory with simulations performed by a ray-optics model code. We consider this dust sample as a good analog for interplanetary and interstellar dust as it shares its refractive index with known materials in these media. Several sensitivity tests have been performed for both structural cases (internal inclusions and surface roughness). Three different samples have been selected to mimic inclusion/coating inhomogeneities: two measured scattering matrices of hematite and white clay, and a simulated matrix for water ice. These three matrices are selected to cover a wide range of imaginary refractive indices. The selection of these materials also seeks to study astrophysical environments of interest such as Mars, where hematite and clays have been detected, and comets. Based on the results of the sensitivity tests shown in this work, we perform calculations for a size distribution of silicate type host particle model with inclusions and surface roughness to reproduce the experimental measurements of a dust sample. The model fits quite well the measurements, proving that surface roughness and internal structure play a role in the scattering pattern of irregular cosmic dust particles.

Keywords: Light scattering, Ray-Optics Approximation, Measurements, Mineral dust, Modeling, Scattering matrix

1. INTRODUCTION

Dust can be found in many different environments in the universe, from being a component of the interstellar medium to forming the regolith and atmospheres of Solar System bodies. As an example of its distant detection and study, optical images of the nearby star Fomalhaut show a ring of dust orbiting the central star. This dust is expected to be similar in several properties to the zodiacal dust in our Solar System (Min et al. 2010), so through its study we can better understand our vicinity. Moreover, the scattered light by this system could be dominated by large dust grains of at least 100 µm. Dust grains are the building blocks of planetary systems. In the core accretion disk surrounding young stars, grains grow typically through collisions, from sub-micron sized particles into larger aggregates until these aggregates reach planetesimal sizes. This growth is limited to micron sizes in dense regions of molecular clouds, but it is possible for them to grow further in the mid-plane of protoplanetary disks (Testi et al. 2014). Here, micron-size dust grains coagulate to form larger structures with complex shapes and compositions. This process significantly changes the optical properties of the scattering particles. To properly interpret observations of protoplanetary disks and to place these observations in the context of the early stages of planet formation, it is crucial to understand the optical properties of these complex structures (Min et al. 2016).

Mineral dust is also present in many Solar System bodies. In planetary atmospheres, suspended grains play an important role in the radiative transfer of incident solar energy, and act as condensation and freezing nuclei within the water cycle. Dust is also found in comets and the surface of atmosphereless satellites. Recently, the Rosetta mission has studied in situ, among other things, dust properties of both the nucleus surface and coma of comet 67P/Churyumov-Gerasimenko thanks to instruments such as GIADA (Grain Impact Analyser and Dust Accumulator) and OSIRIS (Optical, Spectroscopic, and Infrared Remote Imaging System). GIADA was able to distinguish different types of particles populating the coma of 67P. These particles can be separated into two families: compact particles (ranging in

size from 0.03 to 1 mm), that underwent processing within the solar nebula, and fluffy aggregates (ranging in size from 0.2 to 2.5 mm) of sub-micron grains that might be a record of a primitive component, probably linked to interstellar dust (Fulle et al. 2015). Some physical processes related to comets depend strongly on the size distribution of dust particles in their atmospheres, surfaces and the first few meters below (Fulle et al. 2016). It is also important to know the spatial distribution of grains in the coma as illustrated in Della Corte et al. (2015) for Comet 67P/Churyumov-Gerasimenko. The authors determined dynamical and physical properties of cometary dust particles to support the study of the production process and dust environment evolution.

In addition to observations and laboratory measurements of scattering patterns of dust particles, several computational codes have been developed in the last couple of decades to simulate their scattering behaviour, which depends on a broad range of physical properties of the grains. In early investigations these particles were assumed to be spheres so as to simplify the calculations. Electromagnetic scattering from spherical particles is described analytically by Mie theory (Mie 1908), which provides an exact solution to the problem. Unfortunately this approach proved to be unfruitful in many applications as the simulations reproduced neither the observations nor experimental measurements (Mishchenko et al. 2003). Further refinements were made; instead of spheres, cylinders were used in an attempt to introduce more asymmetry in the particles according to the irregularity of natural dust, but, despite this refinement, the results were not as good as expected (Wolff et al. 2006, 2010). The problem is that dust particles are highly irregularly shaped, with a high variety of surface roughness and internal cavities and inhomogeneities.

Several attempts have been made in the past to find a way to reproduce experimental measurements and observations of large irregular particles by means of computer simulations (Draine and Flatau 1994; Mishchenko et al. 2000; Kahnert 2003; Min et al. 2005a; Mishchenko et al. 2009; Muinonen et al. 2009; Nousiainen et al. 2009, 2011; Zubko et al. 2013). The ray-optics approximation method (ROA) is applicable to particles much larger than the incident wavelength, and tries to mimic scattering by tracing ray trajectories through the dust grain (Muinonen et al. 1996). In our approach, these particles are simulated using Gaussian Random Spheres (GRS), as described in section 4.2. ROA computes separately the scattering produced by forward diffraction and geometrical optics. The forward diffraction computation takes into account the two dimensional silhouette of each sample shape. For the geometric optics part, every ray is related to a Stokes vector and, once the ray reaches the surface, reflection and refraction are evaluated according to Fresnel's equation and Snel's law. Although ROA does a significantly better job at reproducing scattering by dust particles than simpler models, like Mie theory, some fine tuning is required by the user.

It is not only the grain's shape but also the presence of wavelength-scale surface roughness which affects scattering properties (Kemppinen et al. 2015). Indeed, the surface roughness seems to be responsible for the phase reddening (increasing spectral slope with increasing solar phase angle) observed in Mars (Schröder et al. 2014). Because of this, the next step in the refinement of phenomenological scattering models was to simulate surface roughness and internal inhomogeneities using simple schemes of Lambertian surface elements and internal screens (Nousiainen et al. 2003). The comparison of the experimental scattering matrix of a dust sample consisting of particles larger than the wavelength with calculations of a ray-optics method employing Gaussian random spheres has made it clear that the single-scattering properties of some samples of irregular particles cannot be accurately modeled without accounting for the effects of surface roughness (Muñoz et al. 2006). More sophisticated models have since been made in response (Muinonen et al. 2009). The results were promising, but insufficient to reproduce experimental measurements. Subsequently, ROA evolved into RODS (Ray Optics with Diffuse and Specular interactions) which is explained in Section 4. RODS includes the effects of more detailed features such as wavelength-scale internal inhomogeneities and surface roughness, characterized by additional scattering matrices. As a first approach, synthetic matrices resembling the scattering of certain materials were used to model wavelength-scale surface roughness, obtaining promising results in the field.

In this work we study for the first time the effect of using experimental scattering matrices to mimic internal and external inhomogeneities in particles larger than the wavelength of the incident light. Moreover, we also perform a parameter space exploration on particle size and volume of inhomogeneities (both internal inclusions and surface roughness) to study their effect on the computed scattering matrix elements. All computations presented in this work are performed at a wavelength of 632.8 nm. The performance of RODS is tested by direct comparison with the experimental scattering matrix of a dust sample with optical properties (refractive index) similar to enstatite, a free-iron form of pyroxene found in both interplanetary and interstellar media. Detailed information about these samples is presented in Section 3.

This article is structured as follows: in Section 2 we present a brief review of the basic scattering concepts; Section 3 gives a description and a discussion of the physical properties of the samples; the ray-optics approximation and RODS code are explained in Section 4; sensitivity tests and the results of simulations to fit experimental data are presented in Section 5; finally, a summary of the results and the conclusions are presented in Section 6.

2. BASIC CONCEPTS.

The polarization state of a light beam can be characterized by the Stokes vector and its parameters, I, Q, U, and V, known as Stokes parameters. An incident beam $\pi\Phi_0(\lambda)$ is related to the scattered beam $\pi\Phi_{\mathbf{det}}(\lambda, \theta)$ through the 4×4 scattering matrix, $\mathbf{F}$ for a sample of randomly oriented particles, where θ is the angle between the propagation directions of incident and scattered light. This matrix has the form (Hovenier et al. 2004):

$$\Phi_{\mathbf{det}}(\lambda, \theta) = \frac{C_{sca}}{4\pi^2 D^2} \begin{pmatrix} F_{11} & F_{12} & F_{13} & F_{14} \\ F_{12} & F_{22} & F_{23} & F_{24} \\ -F_{13} & -F_{23} & F_{33} & F_{34} \\ F_{14} & F_{24} & -F_{34} & F_{44} \end{pmatrix} \Phi_0(\lambda, \theta), \tag{1}$$

where the first elements of the column vectors are fluxes divided by π, and the state of polarization of the beams is described by the other Stokes parameters. Furthermore, λ is the wavelength, C_{sca} is the scattering cross section (rate of energy scattered by the sample), and D is the distance from the sample to the detector. The plane containing the directions of the incident and scattered beams, known as the scattering plane, is the plane of reference for the flux vectors. The F_{ij} elements are dimensionless and depend on particle physical properties, as size, shape, and refractive index, and other parameters as the number of the scattering particles that contribute to the detected radiation, the wavelength of the radiation, and the direction of the scattered light, which is sufficiently described by means of the scattering angle θ for randomly oriented particles. The matrices are normalized such that

$$\frac{1}{4\pi} \int_{4\pi} F_{11} d\Omega = 1, \tag{2}$$

where Ω is the solid angle. The $F_{11}(\theta)$ normalized in this way is called the phase function. The usual way to represent the scattering matrix elements is by dividing $F_{ij}(\theta)$ elements by $F_{11}(\theta)$, for i,j=1, 2, 3, 4 except for i=j=1. For $F_{11}(\theta)$ we will use the relative phase function expression $F_{11}(\theta)/F_{11}(30^o)$ when dealing with size distributions for comparison with measurements. For those sensitivity tests involving individual sizes (no size distribution integration) we maintain the $F_{11}(\theta)$ normalized as presented in Eq. 2. Also, for unpolarized light, the ratio $-F_{12}(\theta)/F_{11}(\theta)$ is called the degree of linear polarization of the scattered light.

The scattering matrix for a given particle depends on the particle's size relative to the wavelength of incident light. This is expressed by the size parameter, x:

$$x = \frac{2\pi a}{\lambda}, \tag{3}$$

where a is the mean radius of the particle.

The rates of energy scattered and absorbed by single particles are expressed by scattering and absorption cross sections, C_{sca} and C_{abs}. These quantities have dimensions of length squared and relate the power scattered and absorbed to a normal surface area upon which equal power is incident. The total attenuation of incident power is the sum of C_{sca} and C_{abs} and is called the extinction cross section C_{ext}. The single-scattering albedo can be described as the fraction of light which is scattered, over that which is extinguished:

$$\varpi = \frac{C_{sca}}{C_{ext}} = \frac{C_{sca}}{C_{sca} + C_{abs}} \tag{4}$$

The angular distribution of scattered power can be conveniently characterized by the so-called asymmetry parameter

$$g = \frac{1}{4\pi} \int_{4\pi} F_{11} cos\theta d\Omega, \tag{5}$$

where θ is the scattering angle. The asymmetry parameter is often used, e.g. in atmospheric energy balance considerations due to its connection to the amount of power scattered back to space.

In this work, every simulation consists of a bulk particle, known also as the host particle, which has a certain size and shape as determined by the choice of GRS parameters. The host particle can contain additional scattering elements with different optical properties to the host, so as to simulate the effect of surface roughness and internal inclusions.

To characterize internal inhomogeneities and structure, a diffuse internal medium (DIM) can be added. We use the single-scattering albedo, ϖ_{DIM}, of the DIM material and a mean free-path length of interaction, l_o, to describe internal structure. In RODS, l_o is related to the volume fraction of diffuse internal scatterers, and is a measure of the mean length that an electromagnetic wave can travel inside the host material between diffuse scattering events. For internal scatterers of radius r and volume fraction ρ_{int}, the mean free path, l_o, can be calculated by

$$l_o = \frac{4r_{DIM}}{3\rho_{int}Q_{ext}},$$ (6)

where Q_{ext} is the extinction efficiency. In our case we compute Q_{ext} by applying Mie theory for small homogeneous spheres of radius r_{DIM} with a refractive index equal to that of the desired inclusion material. Please note that the scatterers are dimensionless in the code: the purpose of r_{DIM} is just to evaluate l_o.

The surface roughness, or diffuse external medium (DEM) is defined in this work through the albedo of the DEM, ϖ_{DEM}, and the optical thickness τ_{ext}, which represents the extinction suffered by electromagnetic waves when transmitted through the host particle surface. The amount of energy that travels through the surface layer unaltered, known as transmittance T, can be described by:

$$T = e^{-\tau_{ext}}$$ (7)

### 3. SAMPLE AND EXPERIMENTAL DATA.

The main objective of this work is to test the RODS approach for reproducing the effect of internal inhomogeneities and wavelength-scale surface roughness on the optical properties of cosmic dust grains much larger than the wavelength of incident light. To do this, we try to model the experimental scattering matrix elements as functions of the scattering angle of a Saharan desert (Libyan) dust sample (Muñoz et al. 2007) which from now on we refer to as dust sample. The measurements of this sample performed at λ=632.8 nm are freely available at the Amsterdam-Granada Light Scattering Database (Muñoz et al. 2012)(http://www.iaa.es/scattering/). Moreover, as detailed below, this sample consists of particles larger than λ, which makes it an ideal test case for the performance of RODS. Based on published refractive indices (Patterson et al. 1977; Dubovik et al. 2006; Shettle and Fenn 1979), we estimate an average refractive index of our experimental sample, m_{sample}=1.5+i0.0004, at λ=632.8 nm. This refractive index is similar to that found in free-iron pyroxene, i.e. enstatite (MgSiO$_3$, $m_{enstatite}$=1.569+i2.6·10^{-5} for λ=650 nm) (Dorschner et al. 1995). Enstatite has been found in protoplanetary debris disks around young stars (Fujiwara et al. 2010) and evolved stars (Molster et al. 2002), and has been proposed through computational modelling as a component, among other silicates, of the Hale-Bopp dust coma (Min et al. 2005b). For these reasons we consider this sample as a good analog for silicate species found in interplanetary and interstellar media.

Size is an important parameter to consider when determining the scattering properties of small particles. To simplify the description of the size distribution, each particle is replaced by a sphere of radius r, with a projected surface area equal to the averaged value over all orientations. Some of the results presented later depend on a size distribution of particles. RODS can compute one single size per simulation, so we perform simulations for various particle size following the measured size distribution of the sample. The values of this size distribution are presented and studied in Muñoz et al. (2007) and are available in the Amsterdam-Granada Light Scattering Database (Muñoz et al. 2012). From the retrieved number distribution we obtained the values of the effective radius, r_{eff}, and effective variance, v_{eff}, defined as follows (Hansen and Travis 1974):

$$r_{eff} = \frac{\int_0^\infty r\pi r^2 n(r)dr}{\int_0^\infty \pi r^2 n(r)dr}$$ (8)

$$v_{eff} = \frac{\int_0^\infty (r - r_{eff})\pi r^2 n(r)dr}{r_{eff}^2 \int_0^\infty \pi r^2 n(r)dr}$$ (9)

The effective radius and variance for the dust sample are r_{eff}=125 µm and v_{eff}=0.15 which makes it an ideal test case for the performance of RODS.
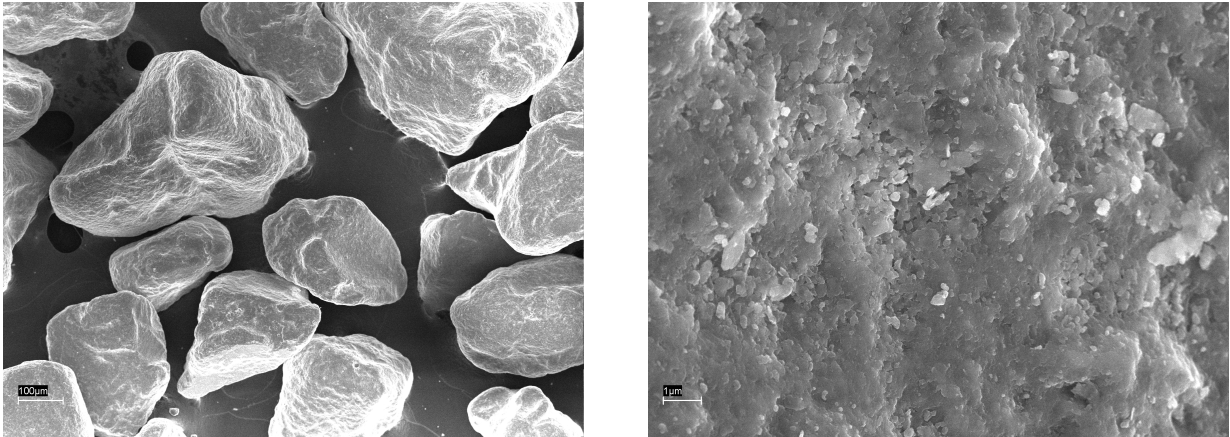
Figure 1: FESEM images of the dust sample. The image on the left shows us the shape that we are trying to reproduce with Gaussian Random Spheres. The right image shows wavelength size surface roughness. The bar in the bottom left corner of each panel correspond to 100 µm and 1 µm respectively.

Some examples of images of particles in the sample, taken with a Field Emission Scanning Electron Microscope (FESEM), are presented in Figure 1. The particles have round shapes with occasional sharp edges (Figure 1 left panel). In Figure 1 right panel, we show a close up of the small-scale surface structure.

4. MODELING APPROACH.

In this work we use a simulation code based on ray optics with diffuse and specular interactions (RODS). The method is thoroughly described by Muinonen et al. (2009), so here we give only a brief description. Diffraction and geometric optics are treated separately. Moreover, the RODS code takes into account internal and/or external diffuse scattering media. The diffuse scatterers can constitute an internal medium distributed uniformly within the particle interior (DIM). Moreover, they can be added as an external medium covering the surface of the particle (DEM). Whereas DIM is a three-dimensional medium, the physical thickness of DEM is negligible compared to the size of the particle, and diffuse scattering occurs within a single infinitesimal location on the surface. DIM is defined by the volume fraction ρ_{int} and single scattering albedo ϖ_{int}, while DEM is described by its optical thickness τ_{ext} and ϖ_{ext}. These inhomogeneities produce their own scattering pattern inside the host particle. The scattering behaviour of these inclusions can be simulated inside RODS using either double Henyey-Greenstein functions, Rayleigh scattering or customized input matrices. The latter case is the one selected in this work; the input matrices comprise six elements ($F_{11}(\theta)$, $F_{12}(\theta)$, $F_{22}(\theta)$, $F_{33}(\theta)$, $F_{34}(\theta)$, and $F_{44}(\theta)$) taken from laboratory measurements; these are the non-zero independent elements when the sample is an ensemble of irregular particles with random orientations.

The simulations discussed in this work were performed at $\lambda = 632.8$ nm so as to agree with the laboratory setup used to measure the input matrices, as well as the results of Nousiainen et al. (2011). Strictly speaking, the Ray Optics Approximation (ROA) is valid when the curvature of the particle surface is much larger than the wavelength of the incident radiation everywhere on the particle and the surface can thus be considered locally planar, and when the phase differences between internal and external fields across the surface irregularities are sufficiently large to suppress the interference effects associated with the irregularities (Muinonen et al. 1997). However, it may provide sufficiently accurate results even when these conditions are not well met. It is noted that the lower particle size limit of the the Ray Optics Approximation is not well defined and difficult to establish as it depends, for example, on particle shape and composition. As presented in the previous section, the dust sample consists of large particles with overall curvature radii much larger than the wavelength but the particles are partly covered with wavelength-scale surface roughness. That makes it an interesting test case for studying the performance of RODS.

4.1. *Input matrices.*

In this section we describe the samples used to mimic internal/external inhomogeneities. All optical properties given below are valid for a wavelength of 632.8 nm. The scatterers are embedded in the host particle, which has refractive index m$_{host}$=1.5 + i(0.00001-0.0099). The imaginary part of the refractive index, k, is varied broadly by several orders of magnitude to test its role on the computed scattering matrix.

Based on the desertic origin of our cosmic dust analog, we can assume hematite (Jeong and Nousiainen 2014; Kemppinen et al. 2015) and clay particles (Banin et al. 1988; Orenberg and Handy 1992) as good candidates for simulating its internal and external inhomogeneities. Hematite is also found on Mars (Kula and Baldwin 2012), and is of interest in the study of the history of water on the planet. Also it may be a component exoplanetary atmospheres if their temperature allow its presence in solid form (Grenfell et al. 2010). Clay flakes can be found on the surface of Mars (Roush and Orenberg 1996). In this case clay is found also in presence of pyroxenes (Poulet et al. 2005). As a result, the sample of white clay which has previously been studied in the laboratory can be used to represent surface roughness in the samples where clay is present. Moreover, hematite and white clay are good examples of strongly and weakly absorbing particles respectively.

In this work we have used experimentally measured hematite and white clay scattering matrices as inputs in the code for the DIM and DEM. The measured scattering matrix for hematite is presented in Muñoz et al. (2006) at $\lambda = 632.8$ nm. The data for these two measured samples are hosted at the Amsterdam-Granada Light Scattering Database (Muñoz et al. 2012) and are freely available to the community. In Table 1 we show some physical properties of this sample. Hematite is a type of iron oxide Fe_2O_3, having a dark red powder aspect. We assume a refractive index $m_{hematite}$=3 + i0.01. The measured scattering of the white clay sample at 647nm is presented in Muñoz et al. (2011). The difference in wavelength between this measurement and the simulations is small enough to have insubstantial consequences. This material is a white powder whose main constituents are illite, kaolinite, montmorillonite and quartz. In our calculations we assume a refractive index $m_{whiteclay}$=1.6 + i10^{-5} at visible wavelengths.

As well as these two samples, it is also interesting to study the effects of water ice as inclusion material and as a wavelength-scale surface roughness for its role in many different astrophysical environments. In outer space we can find ice as a coating or major component of dust particles, for example in comets, asteroids, satellites and planetary atmospheres. Its existence as a coating (partially or totally) in protoplanetary dust has been proposed in small particles (as small as ∼20 µm) in Grigorieva et al. (2007). Since there are not available experimental scattering matrices for ice available, we have used a Mie model by this case. We assume a spherical particle with a radius r = 0.5 µm and refractive index $m_{waterice} = 1.33$ + i10^{-5}. From this Mie simulation, other optical parameters are obtained in addition to the scattering matrix, other optical parameters are also obtained; among them, the extinction coefficient Q_{ext}, which is necessary for computing the mean free path l_o for the DIM inclusions (Eq. 6). These values are $Q_{ext} = 1.013$ when the host particle is weakly aborbing, and $Q_{ext} = 0.471$ for the highly absorbing host particle. This Q_{ext} has been computed using the relative refractive index ($m_{waterice}/m_{host}$) as the host medium is not a vacuum. When the host particle is weakly absorbing, k_{host} is small enough to neglect, so we only take into account n_{host} (see Table 1). Since the classical Mie theory cannot be used for highly absorbing host media, we have used a code developed by Sudiarta and Chylek (2001) to obtain Q_{ext} when m_{host}=1.5 + i0.0099.

As in the case for ice, we need the value of Q_{ext} to compute l_o for hematite and white clay as an input for the DIM simulations. As the hematite particles are small enough, we assume the size distribution of the hematite measured in the laboratory by Muñoz et al. (2006) when computing the Mie simulation. We obtain a value of Q_{ext} equal to 2.091 for the m_{host}=1.5 + i10^{-5} and 2.69 for the m_{host}=1.5 + i0.0099. The same procedure is followed to compute Q_{ext} for white clay, but we use r = 0.5 µm inclusion radius as the measured white clay size distribution is too big to act as an internal inhomogeneity. The resulting value for Q_{ext} is equal to 0.477 for m_{host}=1.5 + i10^{-5} and 0.375 for m_{host}=1.5 + i0.0099.

	m=n+ik	r_{eff}	v_{eff}	Composition
Hematite	3+i0.01	0.4	0.6	Fe_2O_3
White Clay	1.6+i10^{-5}	2.6	0.7	Illite, kaolinite, montmorillonite, quartz

Table 1: Physical properties of hematite and white clay samples. This data are available at Amsterdam-Granada Light Scattering Database (www.iaa.es/scattering).

4.2. *Particle shapes*

The host particle shapes was generated as Gaussian random spheres, as detailed in Muinonen et al. (2009). In spherical coordinates, they are described by a radius vector which is the exponential of a Gaussian random variable:

$$r(\vartheta, \phi)\mathbf{e}_r = \frac{a \exp[s(\vartheta, \phi)]}{\sqrt{1 + \sigma^2}}\mathbf{e}_r \qquad (10)$$

$$s(\vartheta, \phi) = \sum_{l=0}^{\infty} \sum_{m=-l}^{l} s_{lm} Y_{lm}(\vartheta, \phi) \tag{11}$$

$$s_{l,-m} = (-1)^m s_{lm}^* \tag{12}$$

where $s(\vartheta, \phi)$ is the logarithmic radial distance, Y_{lm} are orthonormal spherical harmonics, and s_{lm} are Gaussian random variables with zero means. The parameters a and σ are the mean and relative standard deviation. The standard deviation of the Gaussian random variables s_{lm} follow the covariance function Σ_s which is given by a series of Legendre polynomials P_l. The degree l of these polynomials ranges from 0 to ∞, but in the code the series is truncated by l_{min} and l_{max}. The greater the value of l_{min} and l_{max}, the spikier the particle will be, reducing its sphericity accordingly.

The code parameters for the GRS are the mean radius of the host particle r, σ which describes the relative standard deviation of the radius vector, ν which sets the power law of the covariance function, l_{min} and l_{max} to fix the coefficients of the Legendre polynomials and the correlation angle for autocorrelation. The values of these parameters (except the radius r) are fixed for all the simulations presented in this work: $\sigma = 0.2$, $\nu = 3.3$, $l_{min} = 2$ and $l_{max} = 11$. These values are in agreement with the shape distribution of the dust sample presented in Muñoz et al. (2007) which is used as the host particle in this work.

5. RESULTS.

As explained above, we analyze two different kinds of inhomogeneities through the addition of DIM or DEM to the host particle. These media can be composed of one of three materials: hematite, white clay and water ice. For the DIM, the extent of its inclusion is determined by the volume fraction, ρ_{int}. For the case of the DEM, the equivalent parameter is the optical depth, τ_{ext}. In both sets of simulations we have fixed the single scattering albedos of the inclusions, ϖ_{int}, and surface roughness elements, ϖ_{ext}, to 0.9.

Previous results (Muñoz et al. 2007) seem to indicate that the spikiness of the host particle, defined by l_{min}, can actually mimic surface roughness but with less realistic shapes. Therefore, we decide to fix $l_{min} = 2$ corresponding to the actual shape of the dust particles and control surface roughness exclusively by varying τ_{ext}.

Moreover, we have tested the sensitivity of the computed scattering matrices to the value of the real part of the refractive index (n). The results (not shown here) do not indicate any significant effect on the computed scattering matrix elements when changing the value of n from 1.5 to 1.7 in steps of 0.02. Thus, n is fixed to 1.5 in all our simulations.

Some computed results presented in this section are integrated over a size distribution. In those cases, the size distribution consists of 26 different size bins, ranging between 9.55 µm (size parameter $x \sim 95$) and 707.95 µm ($x \sim 7030$) corresponding to the measured size distribution for the dust sample. For every size bin we use 5000 different shapes.

5.1. *Sensitivity study for model parameters.*

In this section we analyze the effects of changes in volume fraction, ρ_{int}, for DIM, and optical thickness, τ_{ext}, for DEM. Size effect figures are also presented, showing how the sensitivity of the scattering matrix to the choice of optical parameters is dependent on the host particle's radius.

5.1.1. *Internal inclusions.*

In a first step we study the effect of switching on the DIM within RODS by changing the volume fraction, ρ_{int}, of hematite (highly absorbing), white clay, and water ice (both weakly absorbing) inclusions in a weakly absorbing (m$_{host}$ = $1.5 + i10^{-5}$) host particle of constant size parameter $x = 100$. We have studied the whole range of ρ_{int} from 0% to 100%. The scattering matrix elements computed for the hematite case (m$_{inclusion} = 3 + i10^{-2}$) are shown in Figure 2. There are common trends with increasing ρ_{int} across all three inclusion types, but these were most pronounced in the case of hematite.

In the case of the $F_{11}(\theta)$ element, it is interesting to note that increasing the volume fraction of internal inclusions produces a narrowing effect in the forward scattering peak. Moreover, it produces a significant enhancement of the flux in the backwards hemisphere for all volume fractions studied. A higher volume fraction of inclusions also raises the peak of the degree of linear polarization for unpolarized incident light ($-F_{12}(\theta)/F_{11}(\theta)$ ratio) and shifts it towards lower scattering angles. Again, this shifting effect is most pronounced in the case of the highly absorbing hematite
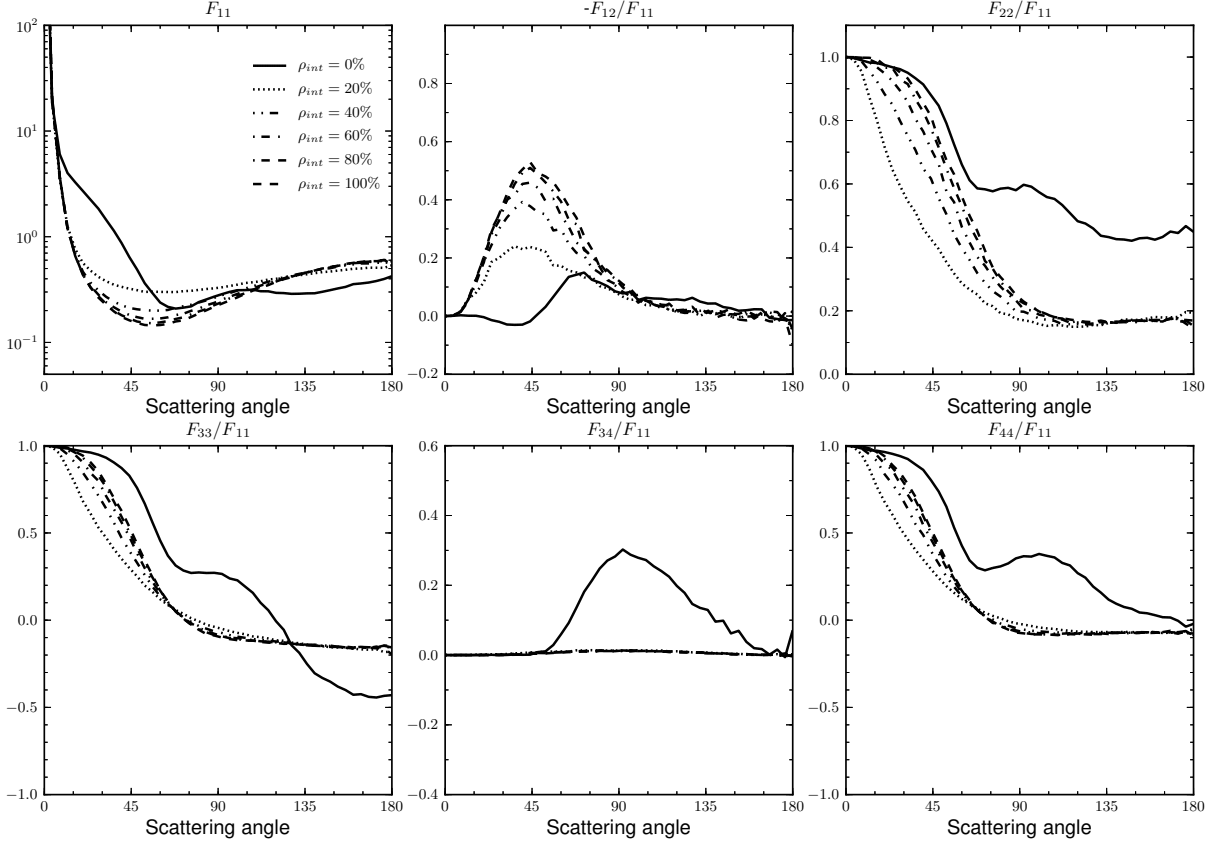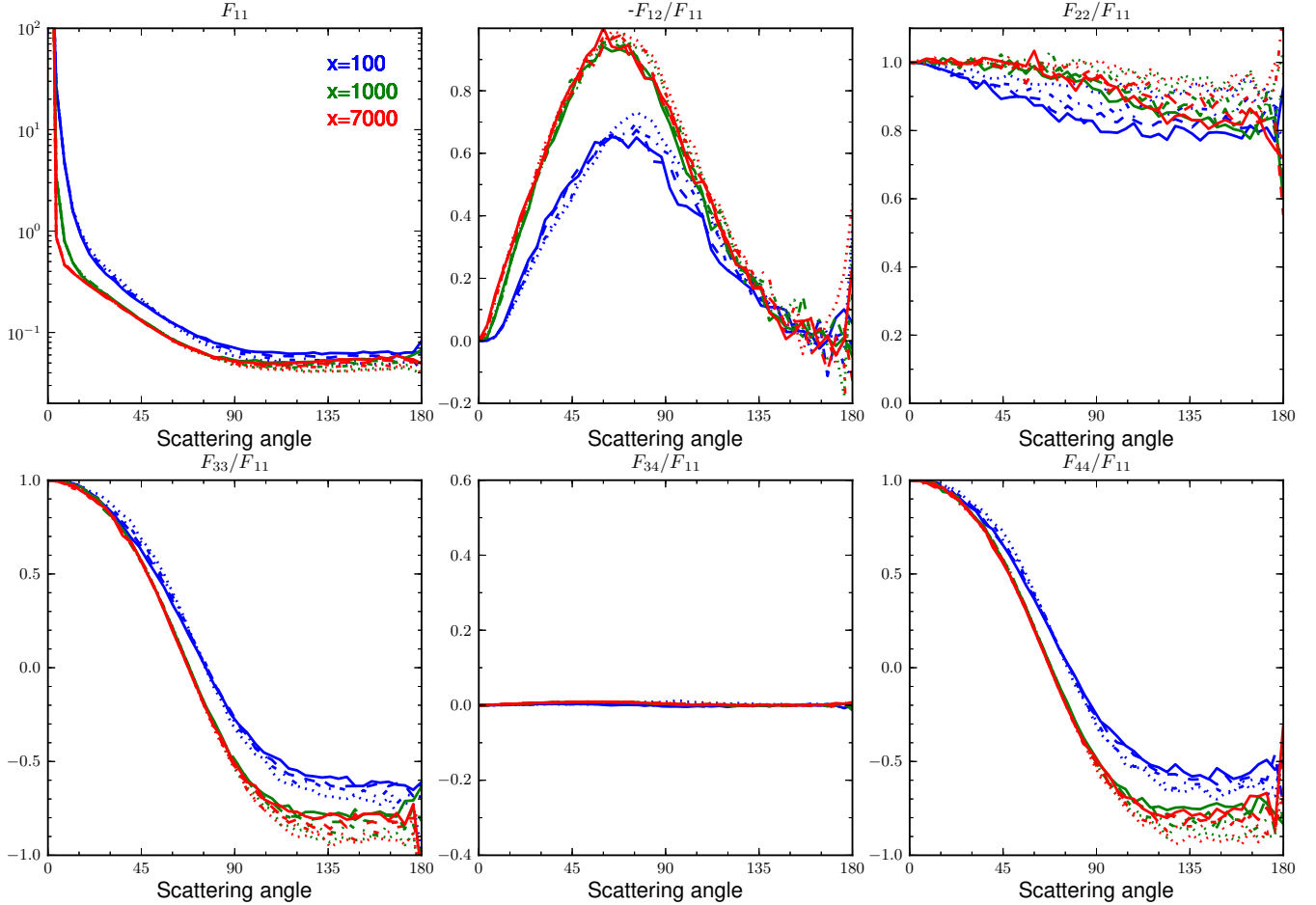
Figure 2: The effect of increasing the volume fraction, ρ_{int}, of hematite inclusions within a host particle of size parameter $x = 100$ and with $m_{host} = 1.5 + i10^{-5}$. Solid and dashed lines correspond to the two extreme cases i.e. host particle without any inclusions ($\rho_{int}=0\%$) and a pure hematite host particle ($\rho_{int}=100\%$).

inclusions, and is barely noticeable (although still present) for white clay and water ice inclusions. The $F_{33}(\theta)/F_{11}(\theta)$, $F_{34}(\theta)/F_{11}(\theta)$ and $F_{44}(\theta)/F_{11}(\theta)$ ratios tend to decrease at nearly all scattering angles when increasing ρ_{int} for all three inclusion types. It is important to highlight that $F_{34}(\theta)/F_{11}(\theta)$ ratio drops to 0 at all scattering angles.

In a second step we assume a highly absorbing ($m_{host}=1.5+i9.9\cdot10^{-3}$) host particle. Figure 3 shows the computed scattering matrix elements for different values of the volume fraction (20%, 40%, 60%, and 80%) for three highly absorbing host particles with different size parameters, namely x=100, 1000 and 7000. In the above figure, the inclusions have the same refractive index as white clay ($m_{inclusion}=1.6 + i10^{-5}$).

In contrast with the weakly absorbing host particle with high absorbing inclusions, the increase of the $F_{11}(\theta)$ at side- and back-scattering regions is significantly weaker. Nevertheless, we still see the effect when increasing the volume fraction of inclusions. Moreover, the increase of the maximum of the degree of linear polarization when increasing ρ_{int} is not as strong as in the case of the weakly absorbing host particle. This increase of ρ_{int} has hardly any effect for medium and large particles ($x = 1000$ and 7000 respectively), and little for the small ones. The $F_{33}(\theta)/F_{11}(\theta)$ and $F_{44}(\theta)/F_{11}(\theta)$ ratios tend to increase when increasing the value of ρ_{int} for all three inclusion types at side- and back-scattering region. The $F_{22}(\theta)/F_{11}(\theta)$ ratio decreases nearly at all scattering angles when increasing the value of ρ_{int}. As in the previous case, $F_{34}(\theta)/F_{11}(\theta)$ ratio drops to 0.

In Figure 4 we present an equivalent study for a weakly absorbing host particle ($m_{host}=1.5+i10^{-5}$) with weakly absorbing white clay inclusions ($m_{inclusion}=1.6 + i10^{-5}$). We also perform some simulations for another weakly absorbing host particle of $m_{host}=1.5+i4\cdot10^{-5}$ to test the sensitivity to small changes of k_{host}, but we observe no differences. The effect of increasing ρ_{int} is more remarkable for small sizes than for medium and large ones. As we can see, for size parameters x=100 and x=1000, the scattering matrix shows variability when increasing ρ_{int}, when for x=7000 the effect rapidly saturates. The maximum of $-F_{12}(\theta)/F_{11}(\theta)$ ratio is remarkably smaller for small particles compared with x=1000 and x=7000, and the $F_{22}(\theta)/F_{11}(\theta)$ ratio for these small particles tends to decrease when increasing ρ_{int}, the opposite behaviour to that shown in Figure 3. The $F_{33}(\theta)/F_{11}(\theta)$ and $F_{44}(\theta)/F_{11}(\theta)$ ratios have a
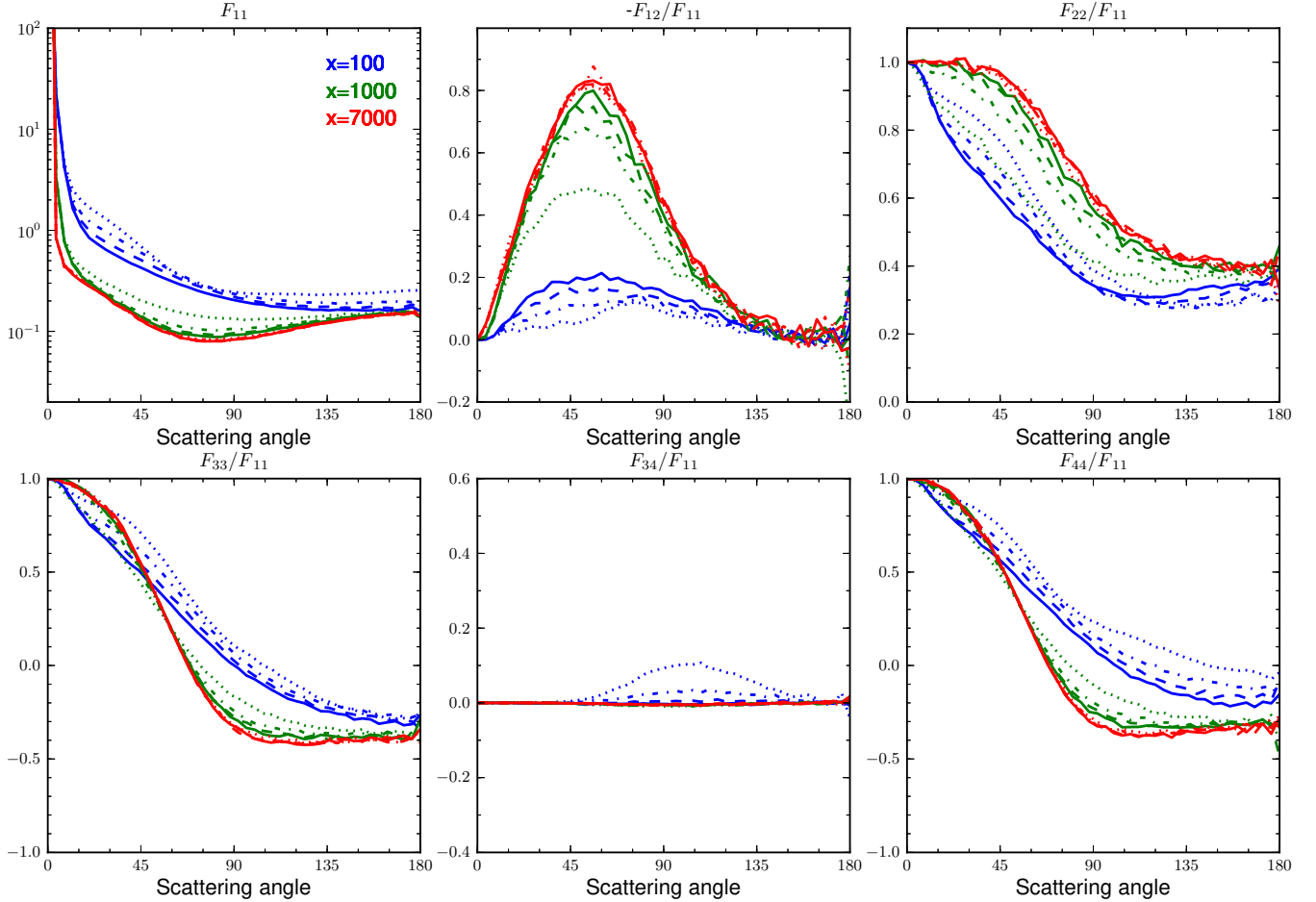
Figure 3: The effect of increasing the volume fraction, ρ_{int}, of white clay inclusions within a highly absorbing (m_{host}=1.5 + i9.9·10^{-3}) host particle varying the size parameter x = 100, 1000 and 7000 (blue, green and red lines, respectively). The volume fraction of internal inclusions, ρ_{int}, are 20% (dotted line), 40% (dot-dashed), 60% (dashed), and 80% (solid).

softer fall for small host particles.

In a third step we study the effect on the computed scattering matrix elements of adding inclusions when integrating over a size distribution. Figure 5 shows the computed results for a size distribution of weakly absorbing (m_{host} = 1.5 + i4·10^{-5}) host particles with three different percentages of white clay inclusions. All computed scattering matrices with internal inclusions are presented together with the corresponding computed scattering matrix for a size distribution of "clean" host particles.

In general, the shape of all computed scattering matrix elements is smoothed out as we add inclusions. As in Figure 2, the forward scattering peak width for the $F_{11}(\theta)$ element narrows, and a flattening effect appears at the side-scattering region. One of the most important effects of adding inclusions shows up in the maximum of the $-F_{12}(\theta)/F_{11}(\theta)$ ratio, which becomes significantly higher for hematite inclusions and moderately higher for white clay and ice inclusions. In general, the rest of the scattering elements have smaller values than the "clean" host particle case. The $F_{33}(\theta)/F_{11}(\theta)$ and $F_{44}(\theta)/F_{11}(\theta)$ ratios decrease when increasing ρ_{int}.

The effect of ρ_{int} on the computed asymmetry parameter for a weakly absorbing host particle is shown in Figure 6. The trends observed are similar for all inclusion compositions. For hematite (left panel of the figure) increasing the volume fractions of inclusions tends to increase the asymmetry parameter for particles smaller than 147.91 µm, does not produce any effect for larger particles. The same trend can be observed for white clay (middle panel), although the values of the computed asymmetry parameter are larger than for hematite, and the convergence occurs at 295.12 µm. The right panel shows a comparison between inclusion types with same ρ_{int}=30%. Water ice and white clay inclusions have virtually the same behaviour, while hematite has smaller values for all sizes. Adding inclusions to the

Figure 4: The effect of increasing the volume fraction, ρ_{int}, of white clay inclusions within a weakly absorbing ($m_{host}=1.5 + i10^{-5}$) host particle varying the size parameter

$x = 100$, 1000 and 7000 (blue, green and red lines, respectively). The volume fraction of internal inclusions, ρ_{int}, are 20% (dotted line), 40% (dot-dashed), 60% (dashed), and 80% (solid).

host particle size distribution triggers a flattening on the trend of the computed asymmetry parameter with scattering angle.

| m_{host}	Single-scattering albedo ϖ of a size distribution of host particles m_{host} with internal inclusions.									
	$\rho_{int} = 0$	$\rho_{int} = 5\%$			$\rho_{int} = 15\%$			$\rho_{int} = 30\%$		
		Hematite	White Clay	Water ice	Hematite	White Clay	Water ice	Hematite	White Clay	Water ice
$1.5 + i4 \cdot 10^{-5}$	0.912	0.643	0.735	0.666	0.620	0.641	0.601	0.615	0.604	0.582
$1.5 + i10^{-4}$	0.828	0.638	0.706	0.652	0.619	0.632	0.598	0.614	0.601	0.580
$1.5 + i4 \cdot 10^{-4}$	0.660	0.622	0.630	0.612	0.614	0.604	0.586	0.612	0.588	0.576

Table 2: Single scattering albedo ϖ of the simulated size distribution with DIM, for three different types of host particles and inclusion composition as function of the volume fraction ρ_{int}.

In Table 2 we present the computed single scattering albedos ϖ for a size distribution of a selected set of host particles, and percentages and compositions of internal inclusions.

5.1.2. *Surface roughness.*

As presented in the previous section, in the first step we study the effect of switching on the DEM by changing the optical depth, τ_{ext}, of hematite (highly absorbing), white clay, and water ice (both weakly absorbing) surface roughness covering a weakly absorbing ($m_{host} = 1.5 + i10^{-5}$) host particle. The scattering matrix elements computed for the
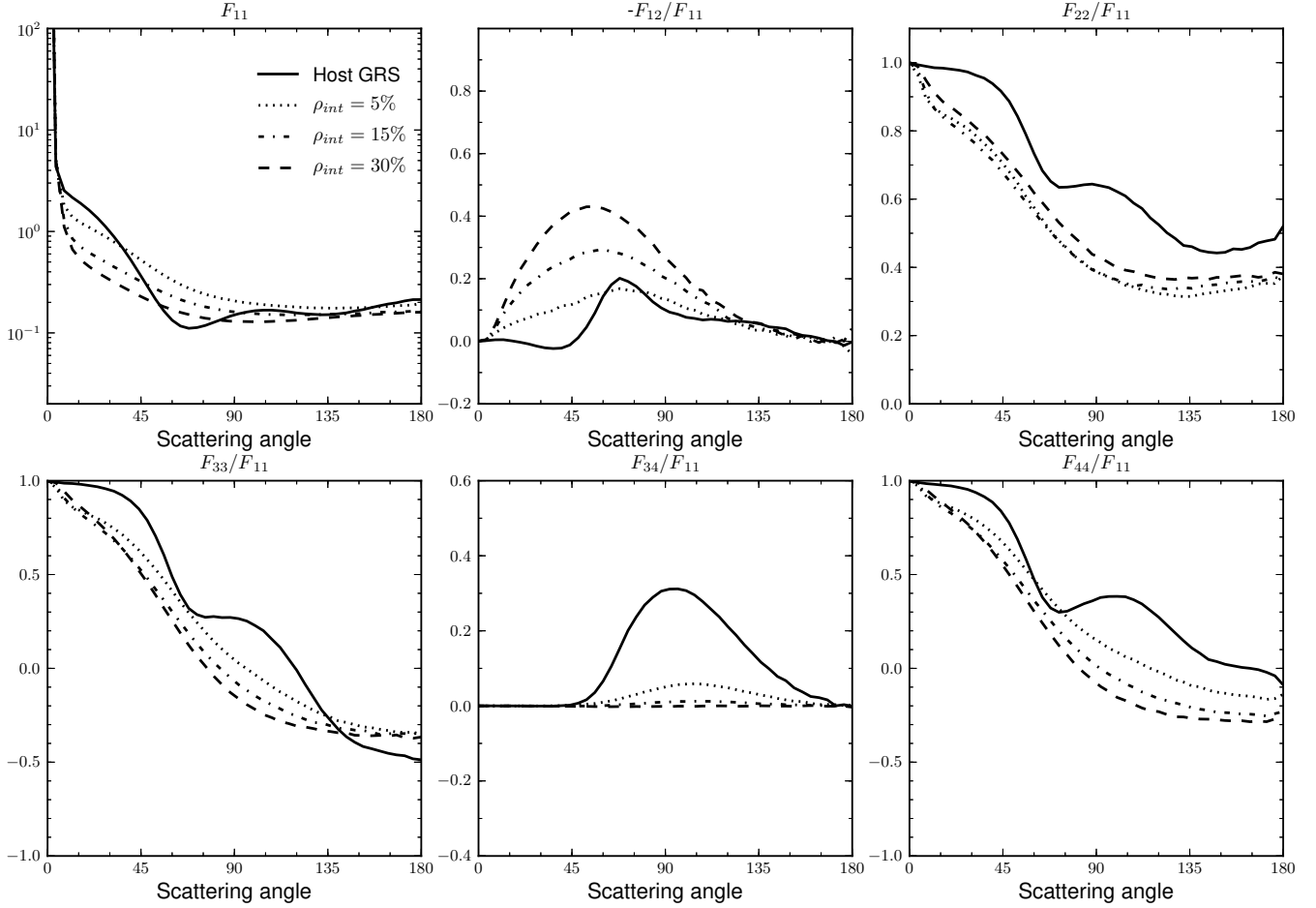
Figure 5: Results for increasing volume fraction, ρ_{int}, of white clay inclusions within a size distribution of weakly absorbing host particles (m_{host}=1.5 + i4·10^{-5}). The ρ_{int} values correspond to 5% (dotted line), 15% (dot-dashed), and 30% (dashed). The results are presented together with the computed scattering matrix for a size distribution of clean host particles.
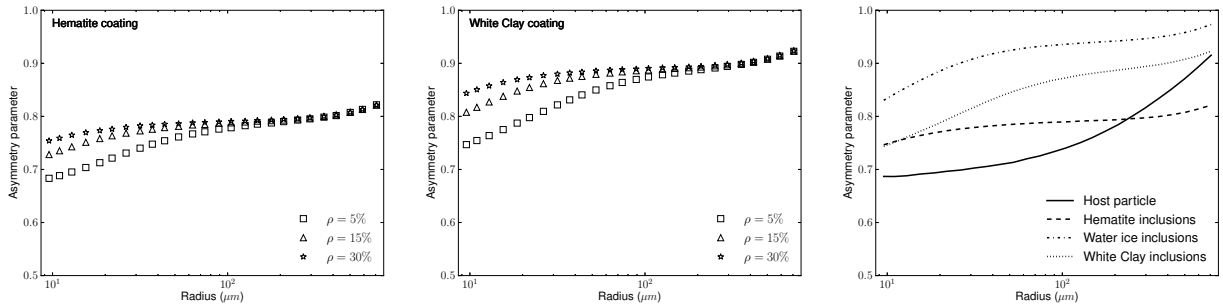
Figure 6: The effect on the computed asymmetry parameter when increasing the volume fraction of internal inclusions within a host particle with $m_{host} = 1.5 + i10^{-5}$: left panel for hematite inclusions and middle panel for white clay inclusions. The right panel shows a comparison between inclusion types (white clay, water ice, and hematite) with ρ_{int} fixed to 30% and the "clean" host particles.

hematite case ($m_{coating}$=3 + i10^{-2}) are shown in Figure 7.

As in Figure 2, the $F_{11}(\theta)$ element forward scattering peak width narrows as τ_{ext} increases, and the side-scattering and back-scattering region flattens and increases over the clean host particle curve. A higher τ_{ext} decreases the maximum of the degree of linear polarization for unpolarized incident light ($-F_{12}(\theta)/F_{11}(\theta)$ ratio). The $F_{22}(\theta)/F_{11}(\theta)$,
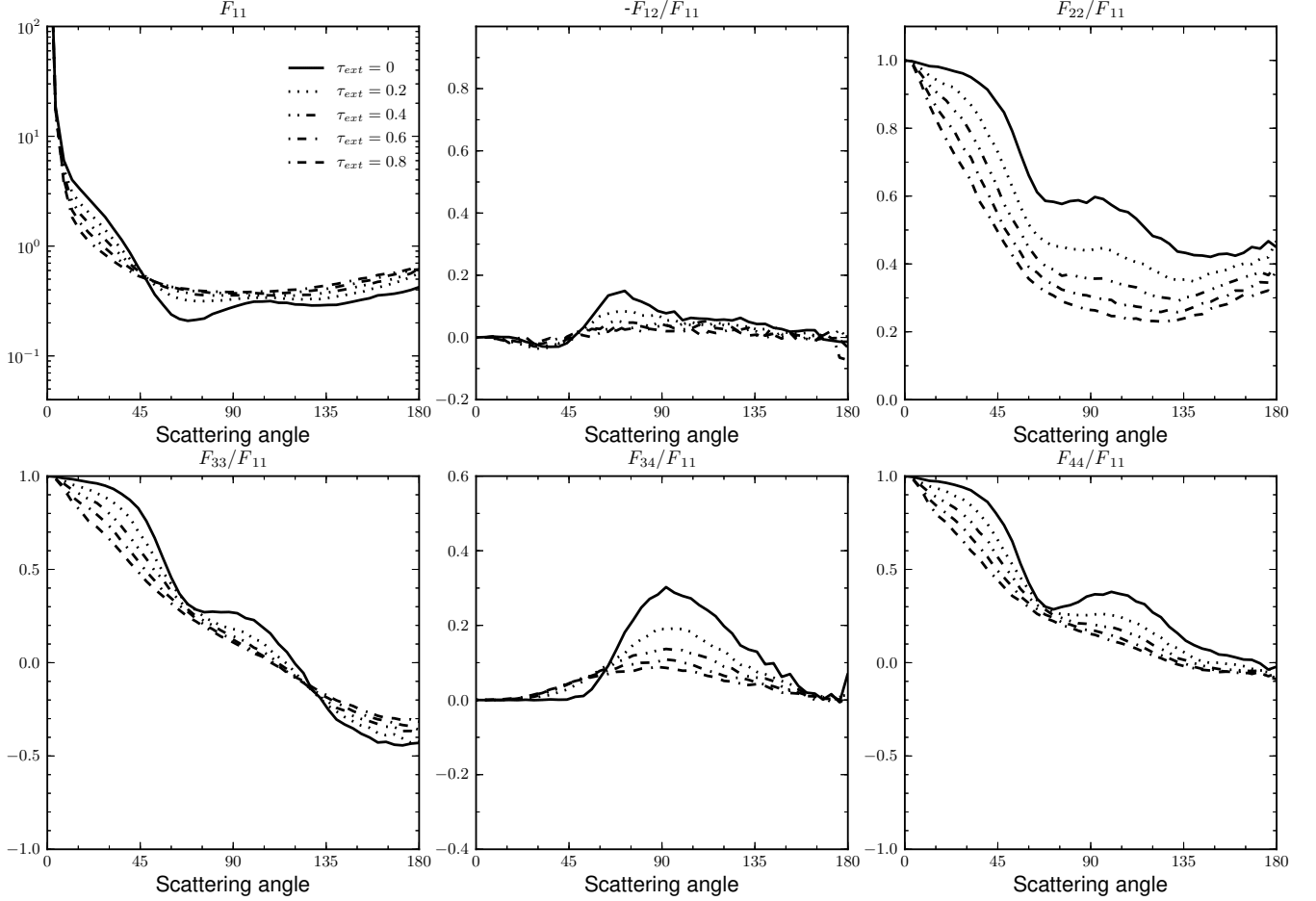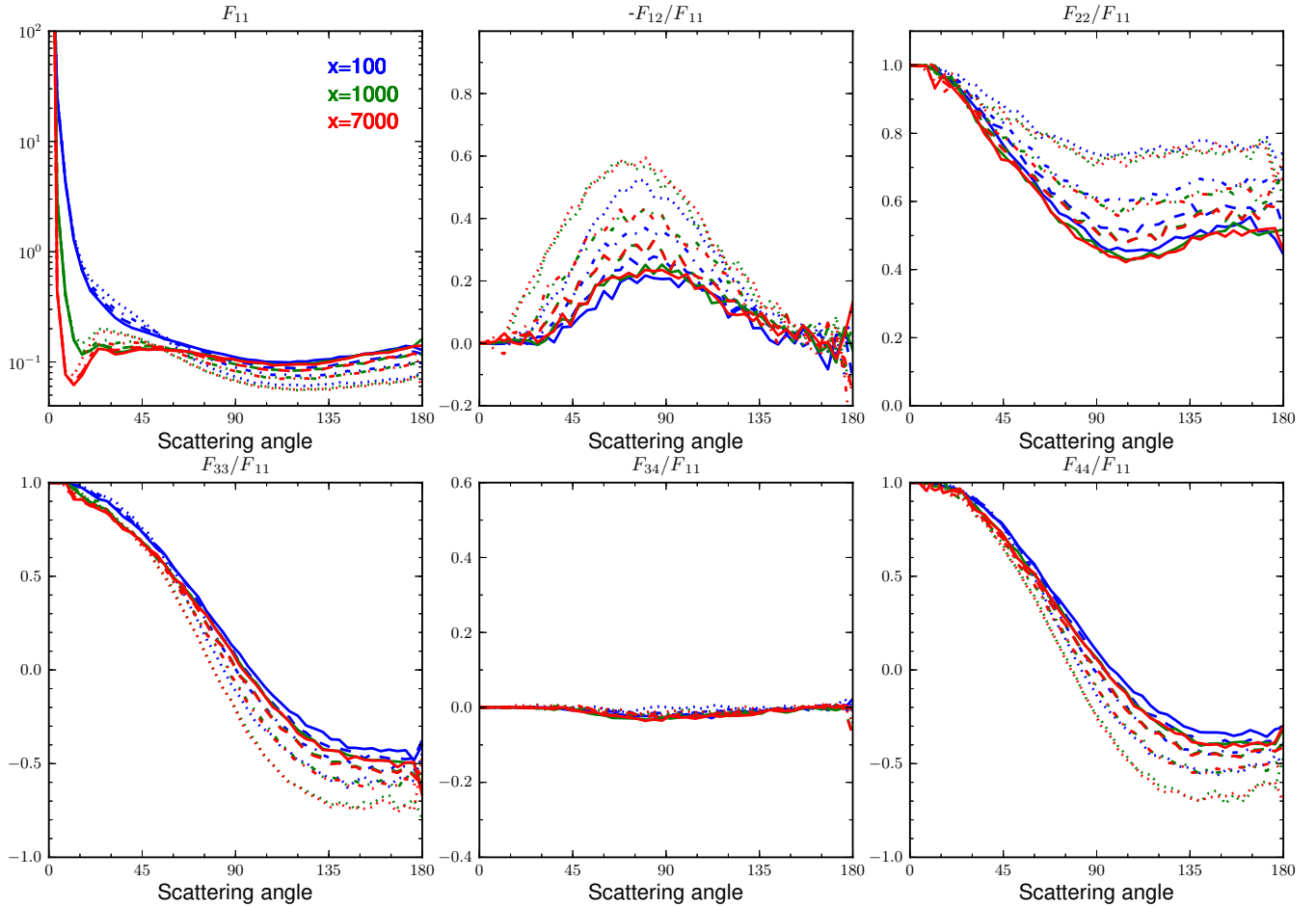
Figure 7: The effect of increasing the optical thickness, τ_{ext}, of external scatterers composed by hematite over a host particle of size parameter $x = 100$ and refractive index $m_{host} = 1.5 + i10^{-5}$. Solid and dashed lines correspond to $\tau_{ext}=0$ (clean host particle) and $\tau_{ext}=0.8$.

$F_{33}(\theta)/F_{11}(\theta)$, $F_{34}(\theta)/F_{11}(\theta)$ and $F_{44}(\theta)/F_{11}(\theta)$ ratios tend to decrease at nearly all scattering angles when increasing τ_{ext} for all three surface roughness types, although this effect is stronger for the $F_{22}(\theta)/F_{11}(\theta)$ ratio.

In a second step we assume a highly absorbing ($m_{host}=1.5+i9.9\cdot10^{-3}$) host particle. Figure 8 shows the computed scattering matrix elements for various optical thickness (0.2, 0.4, 0.6, 0.8) for three highly absorbing host particles with different size parameters, namely x=100, 1000 and 7000. For this figure, the surface roughness material has the same refractive index as white clay ($m_{coating}=1.6 + i10^{-5}$).

As is known, the forward peak of the $F_{11}(\theta)$ element mainly depends on the size of the particles but not on the shape or composition (Liu et al. 2003). The larger the particles the closer the forward peak is to $0°$. It is interesting to note that, for a certain value τ_{ext}, we do not find any significant effect on any of the elements of the scattering matrix when increasing the size parameter with the exception of the $F_{11}(\theta)$ element in forward direction. The computed degree of linear polarization $-F_{12}(\theta)/F_{11}(\theta)$ for a highly absorbing host particle seems to be very sensitive when increasing τ_{ext}. The ratios $-F_{12}(\theta)/F_{11}(\theta)$ and $F_{22}(\theta)/F_{11}(\theta)$ tend to decrease when increasing τ_{ext}, while the opposite effect occurs for the $F_{33}(\theta)/F_{11}(\theta)$ and $F_{44}(\theta)/F_{11}(\theta)$ ratios. The $F_{34}(\theta)/F_{11}(\theta)$ ratio is nearly insensitive to changes in τ_{ext} for all sizes.

For comparison we show the same results for a weakly absorbing host particle. Like in the previous section when studying the internal inclusions, we perform two simulations of weakly absorbing host particles to test the sensitivity to small changes in the imaginary part of the refractive index (for $m_{host}=1.5+i10^{-5}$ and $m_{host}=1.5+i4\cdot10^{-5}$). This time we observe important changes. For $k_{host}=4\cdot10^{-5}$ (presented in Figure 9), the forward scattering peak in $F_{11}(\theta)$ becomes more sensitive to changes in τ_{ext} than same simulations for $k_{host}=10^{-5}$. Moreover, in the case of $k_{host}=4\cdot10^{-5}$ we can see differences between sizes, where the largest size parameter (x=7000) separates from the other two. Because
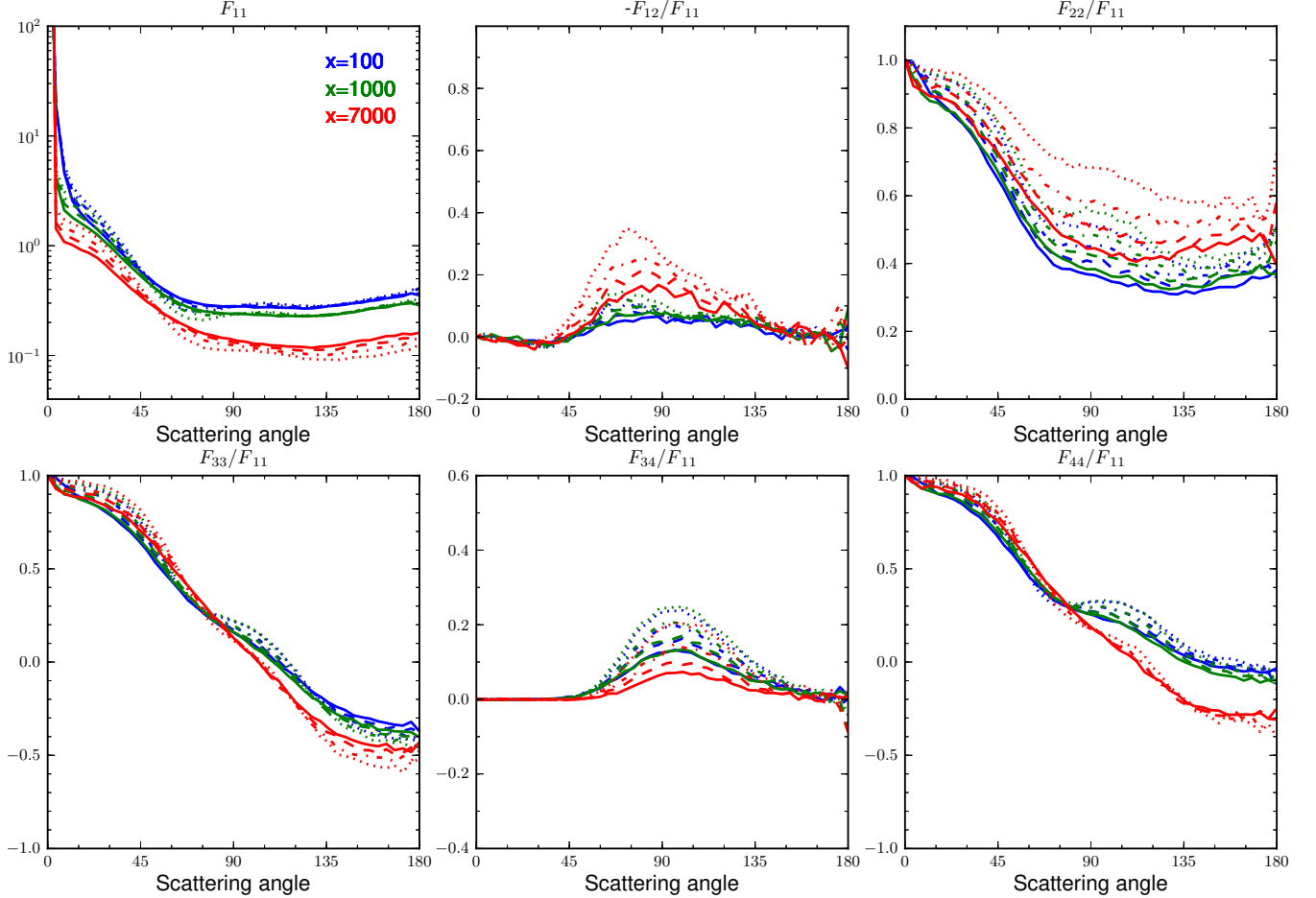
Figure 8: The effect of increasing the optical thickness, τ_{ext}, of white clay acting as surface roughness over a highly absorbing (m$_{host}$=1.5 + i9.9·10^{-3}) host particle varying the size parameter

x = 100, 1000 and 7000 (blue, green and red lines, respectively). Optical thickness τ_{ext} values are 0.2 (dotted line), 0.4 (dot-dashed), 0.6 (dashed), and 0.8 (solid).

these reasons, and due to the fact that the dust sample has been characterized through a k$_{host}$ value of 4·10^{-5}, herein we discuss these results instead of those for k$_{host}$=10^{-5}. In contrast to the previous case shown in Figure 8, the scattering matrix elements are sensitive to the size of the host particle. The $F_{11}(\theta)$ forward scattering region is more sensitive to changes in τ_{ext} for this weakly absorbing host particles than for the highly absorbing ones. The $-F_{12}(\theta)/F_{11}(\theta)$ and $F_{22}(\theta)/F_{11}(\theta)$ ratios maintain the same trend as in Figure 8, but with softer changes. The $F_{33}(\theta)/F_{11}(\theta)$ and $F_{44}(\theta)/F_{11}(\theta)$ ratios are also less sensitives to changes in τ_{ext} than in a highly absorbing host particle. In contrast with Figure 8, the $F_{34}(\theta)/F_{11}(\theta)$ ratio can trace variations in the surface roughness, decreasing its maximum when increasing τ_{ext}.

In a third step we study the effect of adding a coating on the computed scattering matrix elements when integrating over a size distribution. Figure 10 shows the computed results for a size distribution of weakly absorbing (m$_{host}$ = 1.5 + i4·10^{-5}) host particles with three different values of τ_{ext} for a white clay coating (m$_{coating}$=1.6 + i10^{-5}), although the same studies for hematite and water ice have been performed. All computed scattering matrices with surface roughness are presented together with the corresponding computed scattering matrix for a size distribution of "clean" host particles.

White clay and water ice have similar behaviour for $F_{11}(\theta)$. Again, the forward scattering peak width narrows as τ_{ext} increases. Moreover, adding surface roughness flattens the phase function at side-scattering angles. The maximum of the $-F_{12}(\theta)/F_{11}(\theta)$ ratio (degree of linear polarization for unpolarized incident light) decreases in all cases when increasing the surface roughness. This effect is strongest for the hematite coating. The computed $F_{22}(\theta)/F_{11}(\theta)$, $F_{33}(\theta)/F_{11}(\theta)$ and $F_{44}(\theta)/F_{11}(\theta)$ ratios for hematite and white clay inclusions are similar to each other, their values decreasing with increasing τ_{ext}. The $F_{22}(\theta)/F_{11}(\theta)$ ratio values for water ice are slightly closer to the clean host particle

Figure 9: The effect of increasing the optical thickness, τ_{ext}, of white clay acting as surface roughness over a weakly absorbing ($m_{host} = 1.5 + i4 \cdot 10^{-5}$) host particle varying the size parameter

$x = 100$, 1000 and 7000 (blue, green and red lines, respectively). Optical thickness τ_{ext} values are 0.2 (dotted line), 0.4 (dot-dashed), 0.6 (dashed), and 0.8 (solid).

values than for the other two samples, for all τ_{ext}. In the case of water ice surface roughness, the $F_{33}(\theta)/F_{11}(\theta)$ and $F_{44}(\theta)/F_{11}(\theta)$ ratios slightly increase with increasing τ_{ext}, instead of the soft decrease shown in Figure 10.

Figure 11 shows the dependence of the asymmetry parameter, g, when varying coating properties. As shown, g increases as the particle size grows, due to the predominance of reflected light on the surface as the transmitted light is absorbed in the host particle, in agreement with previous results by Nousiainen et al. (2011). Top panel shows the results for a hematite coating, with g decreasing for increasing τ_{ext}, while in the middle panel, for the white clay coating, there is almost no difference between different τ_{ext}. In the bottom panel of Figure 11, we show that the computed results for a coating of white clay and water ice are very similar to each other and following the trend of the clean host particle size distribution, while the hematite coating has smaller values of the asymmetry parameter.

m_{host}	Single-scattering albedo ϖ of a size distribution of host particles m_{host} with surface roughness.									
	$\tau_{ext} = 0$	$\tau_{ext} = 0.2$			$\tau_{ext} = 0.5$			$\tau_{ext} = 1$		
		Hematite	White Clay	Water ice	Hematite	White Clay	Water ice	Hematite	White Clay	Water ice
$1.5 + i4 \cdot 10^{-5}$	0.912	0.882	0.881	0.881	0.844	0.841	0.841	0.795	0.786	0.786
$1.5 + i10^{-4}$	0.828	0.808	0.804	0.804	0.783	0.774	0.804	0.749	0.734	0.734
$1.5 + i4 \cdot 10^{-4}$	0.660	0.665	0.653	0.653	0.669	0.645	0.644	0.673	0.633	0.632

Table 3: Single scattering albedo ϖ of the simulated size distribution with DEM, for three different types of host particles and surface roughness composition as a function of the optical thickness τ_{ext}.

In Table 3 we present the computed single scattering albedos ϖ for a size distribution of a selected set of host
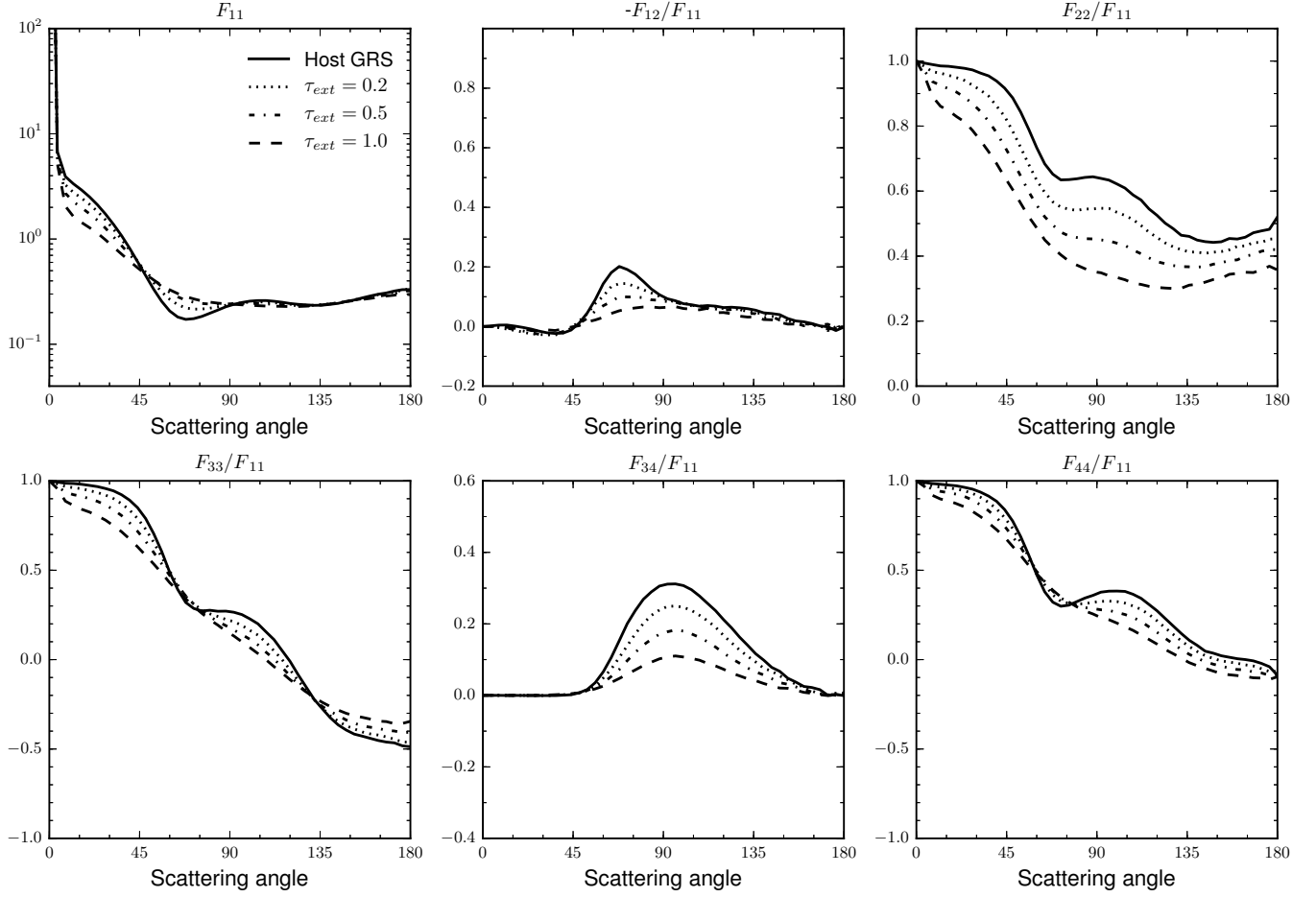
Figure 10: Results for increasing optical thickness, τ_{ext}, of white clay as surface coating for a size distribution of weakly absorbing host particles (m_{host}=1.5 + i4·10^{-5}). The τ_{ext} values correspond to 0.2 (dotted line), 0.5 (dot-dashed), and 1 (dashed). The results are presented together with the computed scattering matrix for a size distribution of clean host particles.
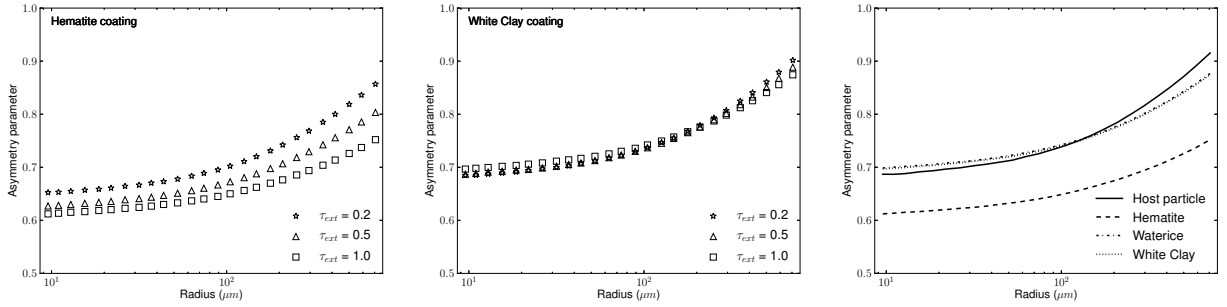
Figure 11: The computed asymmetry parameter as function of radius for two coatings materials, namely hematite (left panel), and white clay (middle panel), with different τ_{ext} values: 0.2 (stars), 0.5 (triangles) and 1.0 (squares). Bottom panel shows a comparison between coating samples: clean host particle (solid line), hematite (dashed), water ice (chain-dashed) and white clay (dotted). In right panel τ_{ext}=1 and ϖ_{ext}=0.9.

particles, and optical thicknesses and compositions for the surface roughness.

5.2. Simulating the experimental scattering matrices for realistic dust particles

As a final test for RODS we consider the experimental scattering matrix for a realistic sample of dust particles presented in Muñoz et al. (2007). As mentioned above, we want to test the performance of RODS by including experimental scattering matrices for natural dust samples as internal and external scatterers.

In Figure 12 we present the measured scattering matrix elements as functions of the scattering angle for the dust sample. The measurements are performed at 632.8 nm covering the scattering angle range from $4°$ to $174°$. The measurements are presented together with i) Mie computations for homogeneous spherical particles; ii) RODS computations for "clean " Gaussian Random Shapes (GRS); and iii) RODS computations for Gaussian Random Shapes including a coating of white clay or hematite. In all computed cases we use the measured size distribution and refractive index ($m_{host} = 1.5 + i4 \cdot 10^{-5}$) of the dust sample. For comparison with the experimental data all calculated phase functions are normalized to 1 at 30°. From the comparison of the experimental scattering matrix with Mie calculations it is clear that light scattered by an ensemble of randomly oriented dust grains can be dramatically different from that scattered by an ensemble of spheres with the same refractive index and size distribution. The Mie identities $F_{11}(\theta) = F_{22}(\theta)$ and $F_{33}(\theta) = F_{44}(\theta)$ are not fulfilled by the dust sample particles. The measured phase function $F_{11}(\theta)$ for the dust sample presents a strong forward peak with a flat dependence at side- and back-scattering regions. That seems to be a general characteristic of irregular compact dust grains. The degree of linear polarization for unpolarized incident light ($-F_{12}(\theta)/F_{11}(\theta)$ ratio) for irregular dust grains shows a typical bell shape with a maximum around $90°$ and a negative branch at large scattering angles. Moreover, the $F_{44}(\theta)/F_{11}(\theta)$ ratio tends to be larger than the $F_{33}(\theta)/F_{11}(\theta)$. The mentioned effects of non-sphericity may have serious implications when interpreting remote sensing observations (e.g. Mishchenko et al. 2003; Min et al. 2012; Räisänen et al. 2013; Kahnert et al. 2014).

The effect of particle shape on the scattering matrix elements is clearly shown by the second set of simulations presented in Figure 12. All computed scattering matrix elements for a size distribution of "clean" Gaussian Random Shapes are significantly closer to the experimental data than those computed for the same size distribution of spherical particles. However, the fitting may be further improved by taking internal and/or surface inhomogeneities of the dust grains into account. As examples the third and the fourth sets of simulations in Figure 12 show the computed results for a size distribution of Gaussian Random Shapes with a coating of white clay and hematite, respectively. In those simulations we assume the optical thickness, τ_{ext} equal to 1.0 and single scattering albedo, ϖ_{ext} equal to 0.9 (Nousiainen et al. 2011). In general, adding surface roughness to the host particles improves the fit to the experimental data for roughly all scattering matrix elements. In particular the coating of white clay produces nearly perfect fits to the experimental data for the $-F_{12}(\theta)/F_{11}(\theta), F_{22}(\theta)/F_{11}(\theta)$, and $F_{33}(\theta)/F_{44}(\theta)$ ratios. However, even though the shape of the $F_{11}(\theta)$ element is significantly improved in the case of the coating of white clay we still do not get a perfect fit for that element.

Encouraged by the results of the sensitivity tests presented in the previous section, we try to improve the fitting to the experimental data including both DIM and DEM in our size distributions of GRS grains, corresponding to a more realistic model for natural dust. In Figure 13, we present the measured scattering matrix elements as functions of the scattering angle for the dust sample together with computations for a size distribution of "clean" Gaussian Random Shapes and two different combinations of DIM and DEM, namely $DIM_{hematite}+DEM_{whiteclay}$, and $DIM_{whiteclay}+DEM_{whiteclay}$. In both cases we fix $\rho_{int} = 1\%$ and $\varpi_{int} = 0.9$, and $\tau_{ext} = 0.5$ and $\varpi_{ext} = 0.9$ which are the parameters that best fit the measurements. As in the previous figure, in all computed cases we use the measured size distribution and refractive index ($m_{host} = 1.5 + i4 \cdot 10^{-5}$) of the dust sample. Moreover, all calculated phase functions are normalized to 1 at 30°. The combination of internal and external inhomogeneities produces better fits for almost all elements of the scattering matrix. With the combination $DIM_{whiteclay}+DEM_{whiteclay}$ we get a nearly perfect fit for the $-F_{12}(\theta)/F_{11}(\theta), F_{22}(\theta)/F_{11}(\theta)$, and $F_{33}(\theta)/F_{44}(\theta)$ ratios at all measured scattering angles. The $F_{11}(\theta)/F_{11}(30^o)$ seems to be slightly overestimated at side- and back-scattering regions. However, we may note that this could be an effect of the arbitrary normalization to 1 at 30° degrees. Figure 14 corresponds to the uppermost left panel of Figure 13, showing $F_{11}(\theta)$ with two types of normalizations: normalized to unity at 30° and normalized to unity at 90°. This normalization at 90° is used to avoid the forward scattering domain where the $F_{11}(\theta)$ values show strong variations in a narrow range of scattering angles. As can be seen, the $DIM_{whiteclay}+DEM_{whiteclay}$ case produces a nearly perfect fit in the scattering angle range from ∼45 to 174 degrees. There is also good agreement in the diffraction peak region, which is mainly dependent on the size of the particles. The main differences occur in the 5-45 degree region where the computations underestimate the $F_{11}(\theta)$ element. The overall improvement to the fit with experimental data when inclusions are added illustrates the importance of internal and surface structure for computing the scattering behaviour of irregular particles.
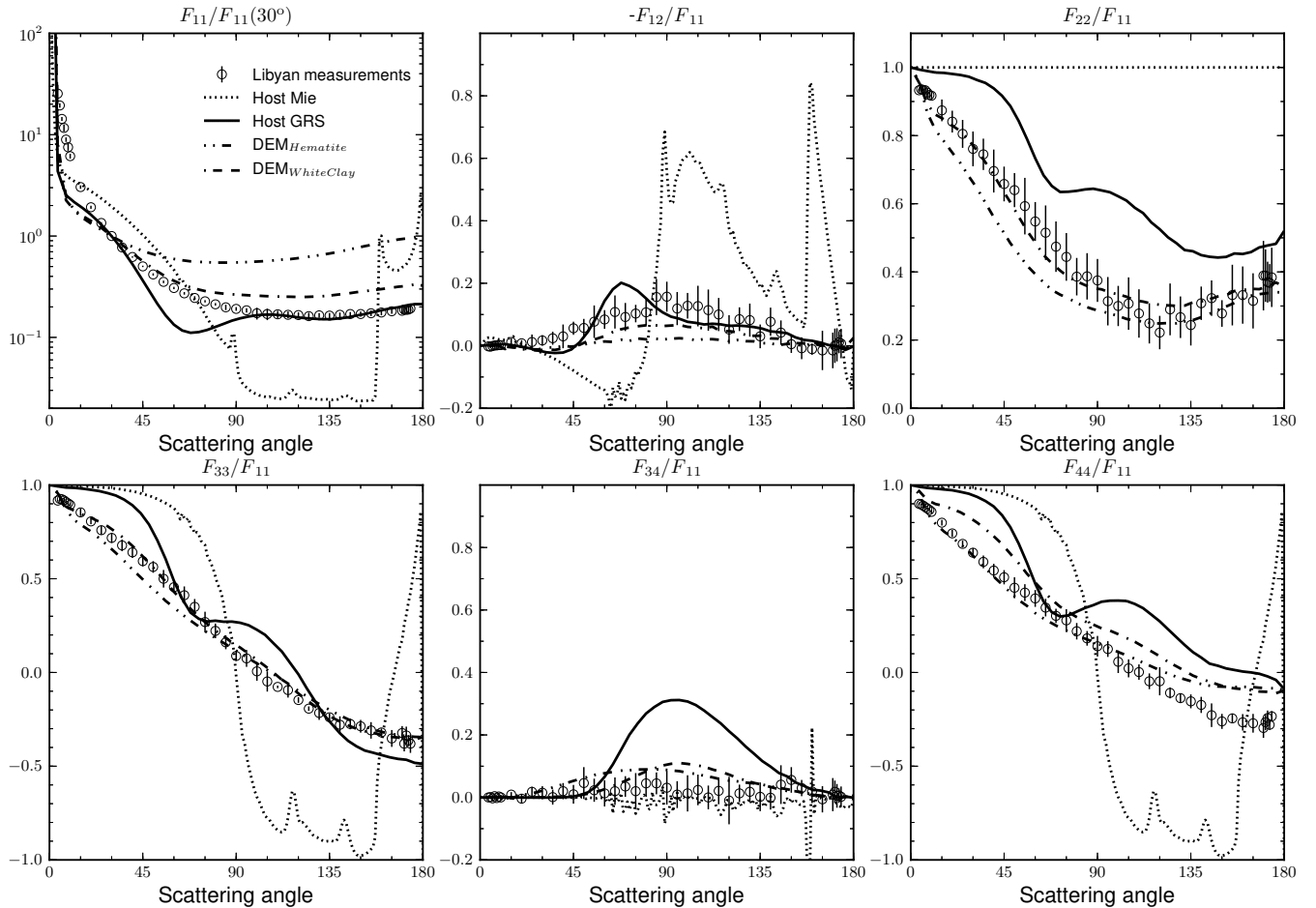
Figure 12: Comparison between experimental measurements of the dust sample size distribution (circles with error bars) and four different computed scattering matrices: a host particle size distribution composed by spheres computed by a Mie simulation (doted line); a host particle size distribution of "clean" irregular particles (Gaussian Random Shapes, solid line); and two different size distributions of GRS particles with two surface roughness compositions: hematite ($\cdots$ –) and white clay ($\cdot$ – –). Surface roughness parameters are $\tau_{ext} = 1.0$ and $\varpi_{ext} = 0.9$.

6. SUMMARY AND CONCLUSIONS.

The purpose of this work is to study the effects that internal inclusions and wavelength-scale surface roughness have on the scattering matrix elements of large cosmic dust grains. To achieve this, we perform sensitivity tests of the RODS code using experimentally measured scattering matrices as inputs for simulating internal and surface inhomogeneities. This paper can be considered as an extension of the study done by Nousiainen et al. (2011), but performing a parameter space exploration by changing the various knobs of the RODS code. For realistic input matrices, two different samples have been used: hematite and white clay, studied in Muñoz et al. (2006) and Muñoz et al. (2010) respectively. These samples are chosen to compare the effect of highly absorbing and weakly absorbing inhomogeneities on the computed scattering matrix. Moreover, these materials are known to be present in astrophysical environments such as Mars, comets and asteroids.

In particular we study the effects of changes in the volume fraction, ρ_{int}, of internal inclusions (DIM), and the optical thickness, τ_{ext}, of the surface roughness (DEM). Size effect figures are also presented, showing how the sensitivity of the scattering matrix to the choice of optical parameters is dependent on the host particle's radius.

From the size effect studies we conclude that the DIM hardly affects scattering when the host particle is highly absorbant. Sensitivity to DIM is practically non-existent regardless of the inclusion material. Only the $F_{11}(\theta)$, $-F_{12}(\theta)/F_{11}(\theta)$, and $F_{22}(\theta)/F_{11}(\theta)$ ratios are slightly affected for small host particle sizes. In contrast, when dealing with a weakly absorbing host particle, all scattering matrix elements are affected to some extent extent even when the DIM is composed of a weakly absorbing material. This situation is reversed when DEM is studied, as the
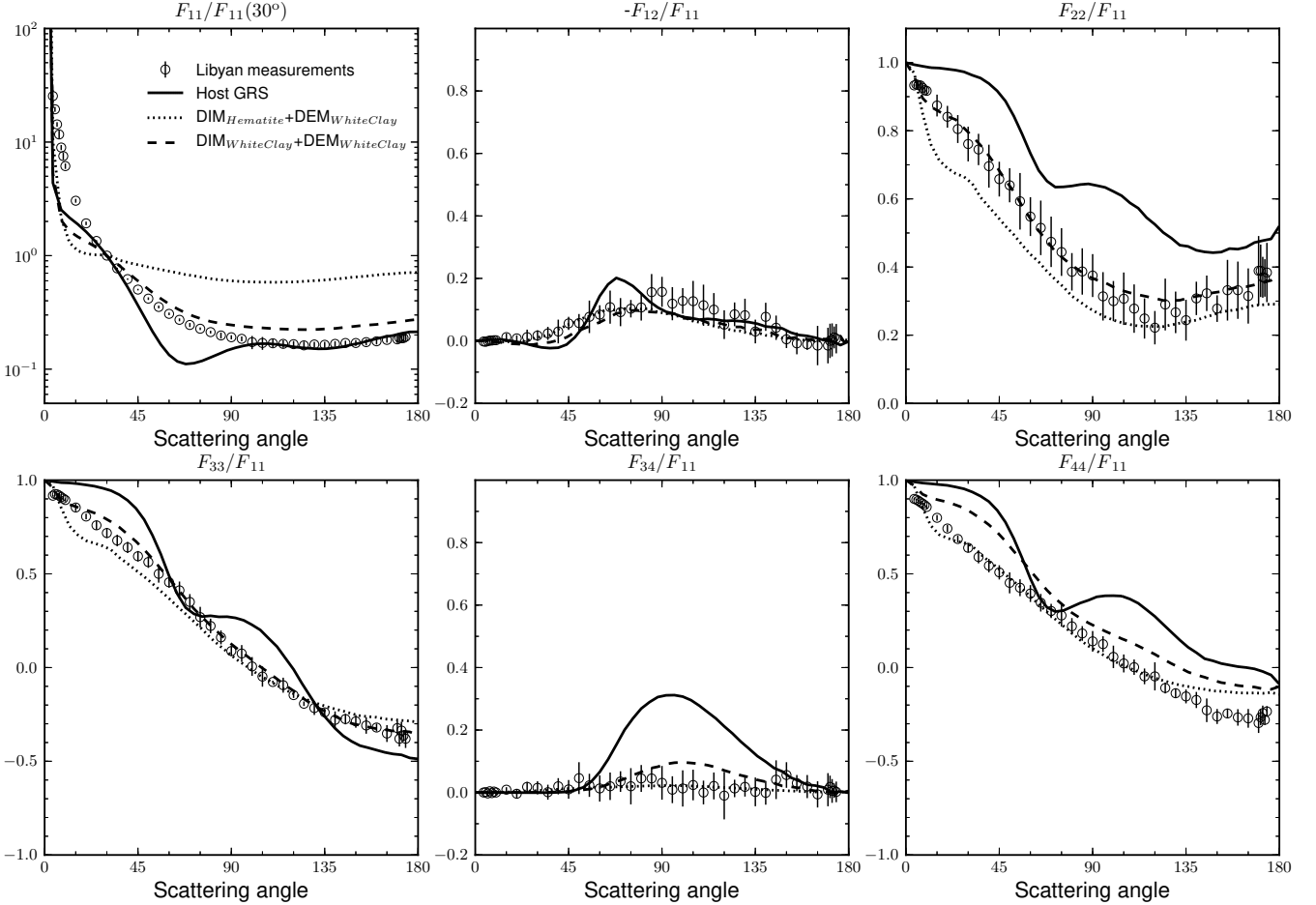
Figure 13: Comparison between experimental measurements of the dust sample size distribution (circles with error bars) and three different computed scattering matrices: a host particle size distribution of "clean" irregular particles (Gaussian Random Shapes, solid line) and two different size distributions of GRS particles including both, Diffuse Internal Medium (DIM) and Diffuse External Medium (DEM) compositions, namely $DIM_{hematite}+DEM_{whiteclay}$, and $DIM_{whiteclay}+DEM_{whiteclay}$. The DIM and DEM parameters are fixed, being $\rho_{int} = 1\%$ and $\varpi_{int} = 0.9$, and $\tau_{ext} = 0.5$ and $\varpi_{ext} = 0.9$ respectively.

computed scattering matrix elements for highly absorbing host particles are strongly affected when τ_{ext} increases. The effect of τ_{ext} is mainly constrained to the $F_{11}(\theta)$, $-F_{12}(\theta)/F_{11}(\theta)$, and $F_{22}(\theta)/F_{11}(\theta)$ ratios. There are hardly any differences between different size parameters when studying DEM for $m_{host}=1.5+i10^{-5}$ and $m_{host}=1.5+i9.9\cdot10^{-3}$. Further simulations were performed for small differences in the imaginary part of the refractive index of the weakly absorbing host particle ($k_{host}=10^{-5}$ and $k_{host}=4\cdot10^{-5}$). Even for such small differences in the value of k_{host} we see a significant effect on the computed scattering matrix elements. In the case of $k_{host}=10^{-5}$, no size effect is observed for the studied size parameters ($x=100, 1000$ and 7000). However, for $k_{host}=4\cdot10^{-5}$ the computed scattering matrix elements for the largest size parameter ($x=7000$) show significant differences with the computed values for $x=100$, and 1000.

From the results obtained for a size distribution of host particles we consistently observe four effects as we add internal inclusions:

- The forward scattering peak width of $F_{11}(\theta)$ element narrows as the volume fraction of inclusions increases.

- In general, the F11 element is flattened in the side-scattering region and enhanced in the backwards hemisphere with increasing volume fractions of internal inclusions, being significantly stronger for a weakly absorbing host particle with highly absorbing inclusions (Figure 2); this is an interesting result for astronomy, as similar effects have been detected, e.g., in comet comae observations (e.g. Meech and Jewitt (1987)) and protoplanetary debris
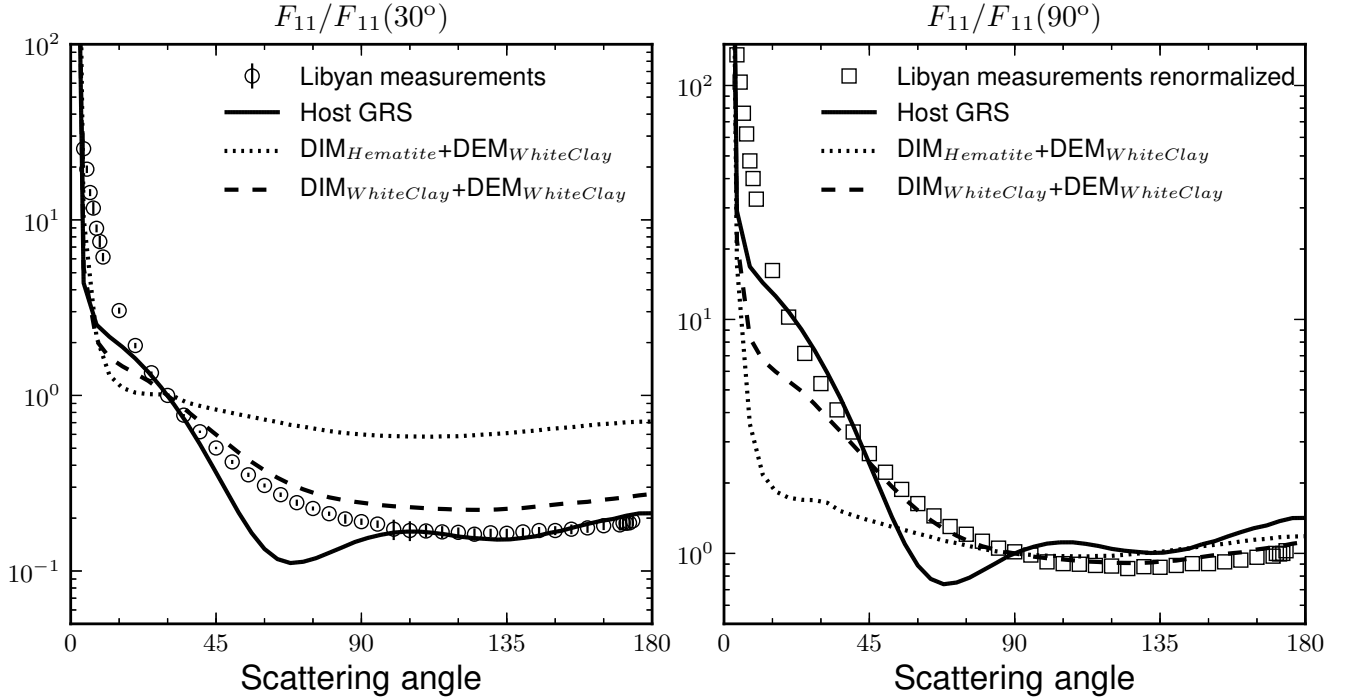
Figure 14: Comparison of phase functions $F_{11}(\theta)$ with and without normalization. The left panel corresponds to the uppermost left panel of Figure 13 for phase function $F_{11}(\theta)/F_{11}(30^o)$. The right panel displays the phase functions normalized at 90 degrees $F_{11}(\theta)/F_{11}(90^o)$. New normalized experimental data values are reprensented as empty squares in the right panel.

disks (e.g. Min et al. (2016)).

- The $F_{34}(\theta)/F_{11}(\theta)$ ratio rapidly decrease to 0 for growing ρ_{int}.

- The maximum of the degree of linear polarization for unpolarized incident light $(-F_{12}(\theta)/F_{11}(\theta)$ ratio) increases strongly as the volume fraction of inclusions is increased (e.g., for the weakly absorbing host particle, the $-F_{12}(\theta)/F_{11}(\theta)$ ratio grows from $\approx 20\%$ for the clean host particle to values over 40% when adding inclusions).

The $-F_{12}(\theta)/F_{11}(\theta)$ ratio increase could be due to a "darkening" within the host particle because of the addition of inclusions. In these tests, the host particles lack surface roughness, so the reflection of the incident light over the soft surface generates a strong linear polarization. Taking into account that for a host particle without internal inclusions, scattered light from the interior of the particle is mainly unpolarized, the degree of linear polarization for unpolarized incident light $(-F_{12}(\theta)/F_{11}(\theta)$ ratio) obtains a maximum value of around 0.2. But when adding inclusions, the mean free path of the refracted light increases inside the particle, so the unpolarized refracted light that should compensate the highly linearly polarized reflected light extinguishes, resulting in a higher degree of linear polarization. This effect can be observed also in the case of a highly absorbing host particle with weakly absorbing inclusions, because the majority of the inner volume is already absorbing.

The general features observed when adding surface roughness to a size distribution of host particles are:

- The same narrowing of the $F_{11}(\theta)$ forward peak and flattening at side- and back-scattering regions mentioned above.

- A decrease in the degree of linear polarization for unpolarized light $(-F_{12}(\theta)/F_{11}(\theta)$ ratio).

- A smoothing and decrease of the rest of the scattering matrix elements.

Finally, we compare the measured scattering matrix for a dust sample presented in Muñoz et al. (2007) with Mie computations for homogeneous spherical particles, RODS computations for "clean" Gaussian Random Shapes, and

RODS computations for Gaussian Random Shapes including a coating of white clay or hematite. In all computed cases we use the measured size distribution and refractive index ($m_{host} = 1.5 + i4 \cdot 10^{-5}$) of the dust sample. The Mie computations cannot reproduce any of the experimental scattering matrix elements. Computations for a size distribution of Gaussian Random Shapes significantly improves the results. The fitting to the experimental data is further improved by taking internal and/or surface inhomogeneities of the dust grains into account. Indeed, our results seems to indicate that a small amount of internal inclusions (ρ_{int}=1%) can significantly affect the computed scattering matrix elements.

In conclusion, using experimental scattering matrices to characterize surface roghness and internal inclusions provides an excellent approach to reproduce the scattering matrices of large cosmic dust grains. Both kinds of inhomogeneities play a major role in the scattering matrix elements. Some refinements are still needed in the code to better reproduce the experimental phase functions of cosmic dust grains at all scattering angles.

7. ACKNOWLEDGEMENTS

REFERENCES

Banin, A., Margulies, L., Ben-Shlomo, T., et al. 1988, Lunar Planet. Sci., 19, 27.

Della Corte, V., Rotundi, A., Fulle, M. et al. 2015, A&A, 583, A13.

Draine, D.T. & Flatau, P.J. 1994, J. Opt. Soc. Am. A, Vol. 11, No. 4.

Dorschner, J., Begemann, B., Henning, T., et al. 1995, A&A, 300, 503.

Dubovik, O., Sinyuk, A., Lapyonok, T., et al. 2006, J. Geophys. Res., 111, D11

Fujiwara, H., Onaka, T., Ishihara, D. et al. 2010, ApJL, 714, L152-L156.

Fulle, M., Della Corte, V., Rotundi, A. et al. 2015, ApJL, 802,L12.

Fulle, M., Marzari, F., Della Corte, V., Fornasier, S., et al. 2016, ApJ, 821,1.

Grenfell, J.L., Stock, J.W., Patzer, A.B.C. et al. 2010, Planet. Space Sci., 58, 1252-1257.

Grigorieva, A., Thébault, Ph., Artymowicz, P. et al. 2007, A&A, 475, 755–764.

Hansen, J. E., and L. D. Travis 1974, SSRv, 16, 527–610.

Hovenier, J.W., van der Mee, C.V.M., Domke, H., 2004. Transfer of polarized light in planetary atmospheres: basic concepts and practical methods. Kluwer. Springer. Dordrecht. Berlin.

Jeong, G. & Nousiainen, T. 2014, ACP, 14, 7233–7254.

Kahnert, F.M. 2003, JQSRT, 79, 775-824.

Kahnert, M., Nousiainen, T. and Lindqvist, H. 2014, JQSRT, 146, 41-58.

Kemppinen, O.,Nousiainen, T. & Lindqvist, H. 2015, JQSRT, 150, 55-67.

Kula, J. & Baldwin, S.L. 2012, Planet. Space Sci., 67, 101-108.

Liu, L., Mishchenko, M., Hovenier, J.W. et al. 2003, JQSRT, 79–80, 911–920.

Meech, K.J. & Jewitt, D.C., 1987, A&A, 187, 585-593.

Mie, G. 1908, AnPhy, 25, 377.

Min, M., Hovenier, J., & de Koter, A. 2005, A&A, 432, 909-920.

Min, M., Hovenier, J., de Koter, A. et al. 2005, Icar., 179, v.1, 158–173.

Min, M., Kama, M., Dominik, C., & Waters, L. 2010, A&A, 509, L6.

Min, M.,Canovas, H., Mulders, G.D. et al. 2012, A&A, 537, A75.

Min, M., Rab, C., Woitke, P. et al. 2016, A&A, 585, A13.

Mishchenko, M.I., Hovenier, J.W., Travis, L.D., 2000. Light Scattering by Non spherical Particles: Theory, Measurements, and Applications (Academic Press, San Diego).

Mishchenko, M., Geogdzhayev, I., Liu, L. et al. 2003, JQSRT, 79-80, 953–972.

Mishchenko, M.I., 2009, JQSRT, 110, 11, 808-832.

Molster, F.J., Waters, L.B.F.M. & Tielens, A.G.G.M. 2002, A&A, 382, 222–240.

Muinonen, K., Nousiainen, T., Fast, P. et al. 1996, JQSRT, 55, 577-601.

Muinonen, K., Lamberg, L., Fast, P. et al. 1997, JQSRT, 57, 197–205.

Muinonen, K., Nousiainen, T., Lindqvist, H. et al. 2009, JQSRT, 110, 1628–1639.

Muñoz, O., Volten, H., Hovenier, J. W. et al. 2004, A&A, 446, 525–535.

Muñoz, O., Volten, H., Hovenier, J. W. et al. 2007, J. Geophys. Res., 112, D13215.

Muñoz, O., Moreno, F., Guirado, D. et al. 2010, JQSRT, 111, 187–196.

Muñoz, O., Moreno, F., Guirado, D. et al. 2011, Icar., 211, 894-900.

Muñoz, O., Moreno, F., Guirado, D. et al. 2012, JQSRT, 113(7), 565-674.

Nousiainen, T., Muinonen, K. & Räisänen, P. 2003, J. Geophys. Res., 108, D1, 4025.

Nousiainen, T. 2009, JQSRT, 110, 14-16, 1261-1279.

Nousiainen, T., Munoz, O., Lindqvist, H. et al. 2011, JQSRT, 112,420–433.

Orenberg, J., Handy, J., 1992, Icar., 96, 219–225.

Patterson, E., Gillete, D. & Stockton, B. 1977, J. Geophys. Res., 82(C21), 3153–3160.

Poulet, F., Bibring, J., Mustard, J. et al. 2005, Nature, 438, 623-627

Räisänen, P., Haapanala, P., Chung, C.E. et al. 2013, Quarterly Journal of the Royal Meteorological Society, vol. 139, 677, 2222-2232.

Roush, T.L., Orenberg, J.B., 1996, J. Geophys. Res., 101, 26111–26118.

Schröder, S., Grynko, Y., Pommerol, A. et al. 2014, Icar, 239, 201-216.

Shettle, E. & Fenn, R. 1979, AFCRL Tech. Rep., 79 0214.

Sudiarta, I.W., & Chylek, P. 2001, JQSRT, 70 (4-6), 709-714.

Testi, L., Birnstiel, T., Ricci, L., et al. 2014, Protostars and
    Planets VI, eds. H. Beuther, R. Klessen, C. Dullemond, Th.
    Henning (University of Arizona Press).
Wolff, M.J., Clancy, R.T., Goguen, J.D., et al. 2006,
    J. Geophys. Res., 111, 12.

Wolff, M.J., Clancy, R.T., Goguen, J.D., et al. 2010, Icar., 208,
    143-155.
Zubko, E., Muinonen, K., Muñoz, O. et al. 2013, JQSRT, 131,
    175-187.

Paper III: Simulations of effects of nanophase iron space weather products on lunar regolith reflectance spectra

SIMULATIONS OF EFFECTS OF NANOPHASE IRON SPACE WEATHER PRODUCTS ON LUNAR REGOLITH REFLECTANCE SPECTRA.

J. Escobar-Cerezo[1], A. Penttilä[2], T. Kohout[2,3], O. Muñoz[1], F. Moreno[1], K. Muinonen[2,4]

[1]Instituto de Astrofísica de Andalucía, CSIC, Glorieta de la Astronomía s/n, 18008 Granada, Spain.

[2]Department of Physics, P.O. Box 64, 00014 University of Helsinki, Finland.

[3]Institute of Geology, The Czech Academy of Sciences, Prague, Czech Republic.

[4]National Land Survey of Finland, Finnish Geospatial Research Institute, P.O. Box 84, 00521 Helsinki, Finland.

ABSTRACT

Lunar soil spectra differ from pulverized lunar rocks spectra by reddening and darkening effects, and shallower absorption bands. These effects have been described in the past as a consequence of space weathering. In this work we focus on the effects of nanophase iron ($npFe^0$) inclusions on the experimental reflectance spectra of lunar regolith particles. The reflectance spectra are computed using SIRIS3, a code that combines ray optics with radiative transfer modeling to simulate light scattering by different types of scatterers. The imaginary part of the refractive index as a function of wavelength of immature lunar soil is derived by comparison with the measured spectra of the corresponding material. Further, the effect of adding nanophase iron inclusions on the reflectance spectra is studied. The computed spectra qualitatively reproduce the observed effects of space weathered lunar regolith.

Keywords: Space weathering, Ray-optics approximation, Reflectance spectra, Lunar regolith, Maturity index, Simulations

1. INTRODUCTION.

Space weathering has been extensively studied and characterized through the last decades. It affects any atmosphereless solar system body. The main interests of space weathering effects over the reflectance spectra are centered in the Moon (Pieters et al. 1993), asteroids (Clark et al. 2002; Brunetto et al. 2015) and planets (e.g. Mercury, Domingue et al. (2014)). In the present work we focus on computer simulations of the effects of space weathering on lunar regolith.

The first lunar soil samples were brought to Earth in 1969 by the Apollo 11 mission. A typical lunar soil spectrum shows an increase of reflectance with wavelength (reddening) as well as weak absorption bands at 1 µm and 2 µm. The bands present at 1 µm and 2 µm are due to Fe^{2+} in silicates. Olivine has three overlapping bands at 1 µm, while pyroxenes has one at 1 µm and another at 2 µm (Burns 1970; Cloutis and Gaffey 1991). The absorption band at 1 µm is consistent with those present in silicate type particles, and the weak 2 µm band is typical of pyroxenes.

On the lunar surface, it was observed that freshly exposed material from meteoroid impacts are brighter than the surrounding regolith deposits. Spectra from pulverized lunar rocks from Apollo missions were studied to compare with the regolith (Pieters et al. 1993). This pulverized material has a higher albedo than the soil gathered in the same spot. Moreover, the absorption bands are more pronounced and the spectrum has a flatter slope. In comparison, lunar soils have weaker absorption bands, larger slope of the spectrum at longer wavelengths (reddening) and lower values of reflectance for all wavelength range (darkening). When the lunar soils were analyzed to explain these differences, abundant dark glass particles were discovered, mainly in the agglutinates. In a first approach, it was suggested a vitrification origin of lunar rocks by meteorite impact, with the consequent darkening (Conel and Nash 1970). A lunar rock sample was melted, and the obtained material had optical features consistent with those observed in the lunar soil, i.e., dark and reddish material with shallower absorption bands. However, subsequent attempts to reproduce these results were unfruitful as they differ from what was expected (Cassidy and Hapke 1975; Hapke et al. 1975). The new experimentally vitrified material had high albedo, flat spectra (no reddening) and strong absorption bands. The differences between these two experiments were the environmental conditions. As pointed out by Wells and Hapke (1977), the initial experiments were conducted in a regular atmosphere (Conel and Nash 1970), whereas these new experiments were made in a vacuum chamber, along with a different crucible material. This produced oxidizing conditions for the first experiment, generating ferric oxides or Fe^{3+}, which have strong absorption bands similar to

those found in lunar regolith. Vitrification was then discarded as a possible explanation for these spectrum features.

Two experiments were performed by Gold et al. (1970) and Hapke et al. (1970) to test the hypothesis of a surface origin of the space weathering effects. Lunar samples were treated with a solution of 20% hydrochloric acid. HCl washed the surface of the grains without affecting their sizes. The washing of the surfaces produced an increase in the albedos, deeper absorption bands, and a decrease of the spectrum slope. As the lunar rocks are milled, fresh surfaces are exposed, and the effect of the weathered surfaces decreases.

Several numerical models has been developed in the past to mimic the effects of space weathering on the reflectance spectra (see e.g. Hapke 2001; Lucey and Riner 2011; Trang et al. 2017). These models are based on radiative transfer models and Maxwell-Garnett theory. In this work we use SIRIS3 code as described in Muinonen et al. (2009). The code combines the ray optics and radiative-transfer treatments to compute light scattering by irregular particles much larger than the wavelength of the incident light. In geometric optics there are no interference effect among the fields scattered by particles in the system and thus the scattered electromagnetic field can be considered incoherent, significantly simplifying the computations. The ray optics code also accounts for internal medium of diffuse scatterers mimicking inclusions inside the particle. Different versions of SIRIS have been previously used for reproducing the experimental scattering matrices of clouds of irregular mineral dust particles (Muinonen et al. 1996; Nousiainen et al. 2011; Escobar-Cerezo et al. 2017). A recent work report on the performance of SIRIS for reproducing the spectral properties of meteorites in the ultraviolet, visible, and near-infrared ranges (Martikainen et al. 2018).

In the present paper we test the performance of SIRIS3 for modeling the effect of nanophase iron ($npFe^0$) space weathering product on the reflectance spectra of lunar regolith. In particular, we retrieve information about the space weathering nanophase iron $npFe^0$ volume fraction by comparing between experimental and computed spectra. Further, we derive the imaginary part of the refractive index k_{host} of an immature lunar sample in the wavelength range from 300 nm to 2600 nm. This k_{host} is derived by fitting the experimental reflectance spectrum of an immature soil sample to mimic a non-weathered host particle. From there, four models are computed with four different volume fractions of $npFe^0$ inclusions inside the host particle. We use two experimental spectra from NASA RELAB (Reflectance Experiment Laboratory) facility at Brown University for comparison and as starting model. These experimental spectra correspond to two lunar soil spectra from samples named 12030,56 and 12001,853, which are presented in Section 3.

2. SPACE WEATHERING.

Space weathering is produced by galactic and solar cosmic rays, sputtering from solar wind particles and bombardment by micrometeorites. Laboratory experiments suggest a timescale of $10^4 - 10^6$ yr for inducing the space weathering effects observed on the reflectance spectra from S-type near-Earth asteroids (Strazzulla et al. 2005). However, other experiments suggest that this time can be as short as $10^3 - 10^4$ yr in asteroids (Brunetto et al. 2014). This exposure age of space weathered soils can be characterized approximately by the I_s/FeO index, known as maturity index, where I_s is the characteristic ferromagnetic resonance from submicroscopic (single-domain) iron and FeO is the weight percent of FeO in the soil. As the exposure of the soil increases, the single-domain iron amount increases, and thus the higher the value of I_s/FeO.

In the case of the lunar regolith the FeO content in mare soils is, in average, at least three times greater than in highland soils implying larger values of I_s in the former one (Noble et al. 2001; Pieters et al. 2000). Small nanophase iron ($npFe^0$) is formed by space weathering processes near the surface of lunar grains (Keller and McKay 1997). The amount of $npFe^0$ depends on several factors, as the initial availability of Fe^{2+} in the regolith source, the micrometeorites kinetic energy and the frequency of impact, the ion radiation produced by the Sun, and the exposure time to this environment (Pieters et al. 2000). In some cases, several layers of $npFe^0$ are observed, suggesting different episodes of weathering processes (Pieters et al. 2000). Dedicated laboratory experiments have been performed through the years to produce space weathering products on diverse substrates through different methods: laser irradiation (e.g. Brunetto et al. 2005), ion bombardment (e.g. Marchi et al. 2005), microwave irradiation (e.g. Tang et al. 2012) or by chemical reduction as Noble et al. (2007) in silica gels or Kohout et al. (2014) in olivine. In the case of Noble et al. (2007), the silica gel particles contain pores ranging between 2.6 and 50 nm. A treatment with ferric nitrate solutions, drying and posterior calcination produced iron oxides deposits in those pores. The samples were then introduced in a furnace under reducing conditions to obtain several sizes of $npFe^0$ deposits (from 5 to 200 nm). Those samples were then studied to check the effect of the $npFe^0$ size on the reflectance spectra. The Kohout et al. (2014) experiment worked in a similar way, but in this case the naturally present iron in the olivine was the source to produce $npFe^0$. Through two heating processes they could produce different amounts and sizes of $npFe^0$ deposits. Both experiments reproduced the space weathering effects, namely, darkening, reddening and subdued absorption bands on the reflectance spectra.

Moreover, they studied the effects of quantity and size of these products on the reflectance spectra indicating that lunar soil continuum is better simulated with npFe^0 spheres with sizes ranging from 15 to 25 nm (Noble et al. 2007).

Another space weathering product is the so called Britt-Pieters microphase. It consists of Fe^0 particles larger than 33 nm in the regolith (Britt and Pieters 1994). The nanophase iron (npFe^0) seems to be the principal mechanism for producing darkening, reddening and subdued absorption bands on the reflectance spectra of lunar regolith (Pieters et al. 1993), while the Britt-Pieters microphase only produces darkening (Pieters and Noble 2016). In this work we focus on the effects of npFe^0 inclusions on the lunar reflectance spectra.

3. EXPERIMENTAL SPECTRA OF LUNAR SAMPLES.

In this section we present two experimental spectra corresponding to two lunar soil samples with different maturity indexes, namely, samples 12030 (McKay et al. 1972) and 12001 (Morris 1978), collected in Apollo 12 mission. Physical characterization of these samples can be found in Morris (1980) and Taylor et al. (2001). These spectra have been selected as a representative of an immature spectrum and a mature spectrum, respectively. We focus on the measured reflectance spectra of subsamples consisting of grains in the size range from 20 to 45 µm. In particular, subsample 12030,56 is composed of particles ranging from 30 to 37 µm with an I_s/FeO value of 12 i.e. it can be considered as an immature soil sample. Subsample 12001,853 consists of dust particles in the 20-45 µm size range with an I_s/FeO value of 51 (submature).

Their measured reflectance spectra are presented in Figure 1 (top panel). We notice the absorption band weakening as I_s/FeO increases. Also the darkening of the spectra is perceived. To facilitate the slope comparison of the reddening effect, the measurements are normalized at the wavelength of 550 nm in the bottom panel of this figure. Here we clearly see the reddening effect as the maturity index increases. Moreover, the absorption band dampening is easily observed.

4. MODELING APPROACH.

In this work we use a numerical code based on ray optics with diffuse and specular interactions, the so-called SIRIS3 code. The method is thoroughly described by Muinonen et al. (2009), so that we only give a brief description. Diffraction and geometric optics are treated separately, although in this work diffraction is not considered. Moreover, it takes into account internal and/or external diffuse scattering media. The diffuse scatterers can constitute an internal medium distributed uniformly across the particle interior (DIM, for diffuse internal medium). DIM is defined by the volume fraction ρ and by its scattering properties, i.e. single-scattering albedo ϖ and extinction efficiency Q_{ext}. The scatterers are placed in an isotropic medium which we name the host particle, and they represent small scale features that affect the scattering. The scattering behaviour of these inclusions can be simulated inside SIRIS3 using either double Henyey-Greenstein functions, customized input matrices, or Rayleigh scattering. The latter case is the one selected in this work due to the small size of the inhomogeneities (npFe^0 smaller than 20 nm).

4.1. Particle shapes.

The host particle shape is generated as a Gaussian random sphere (GRS), as detailed in Muinonen et al. (2009). In spherical coordinates, they are described by a radius vector which is the exponential of a Gaussian random process:

$$r(\vartheta, \phi)\mathbf{e}_r = \frac{a \exp[s(\vartheta, \phi)]}{\sqrt{1 + \sigma^2}} \mathbf{e}_r \tag{1}$$

$$s(\vartheta, \phi) = \sum_{l=0}^{\infty} \sum_{m=-l}^{l} s_{lm} Y_{lm}(\vartheta, \phi) \tag{2}$$

$$s_{l,-m} = (-1)^m s_{lm}^* \tag{3}$$

where $s(\vartheta, \phi)$ is the logarithmic radial distance, Y_{lm} are orthonormal spherical harmonics, and s_{lm} are Gaussian random variables with zero means. The parameters a and σ are the mean and relative standard deviation. The standard deviation of the Gaussian random variables s_{lm} follow the covariance function Σ_s which is given by a series of Legendre polynomials P_l. The degree l of these polynomials range from 0 to ∞, but in the code the series is truncated by l_{min} and l_{max}. The greater the value of l_{min}, the spikier the particle will be, reducing its sphericity accordingly.

The code parameters for the GRS are the mean radius of the host particle r, σ which describes the relative standard deviation from sphere's surface, ν which sets the power law of the covariance function, l_{min} and l_{max} to fix the
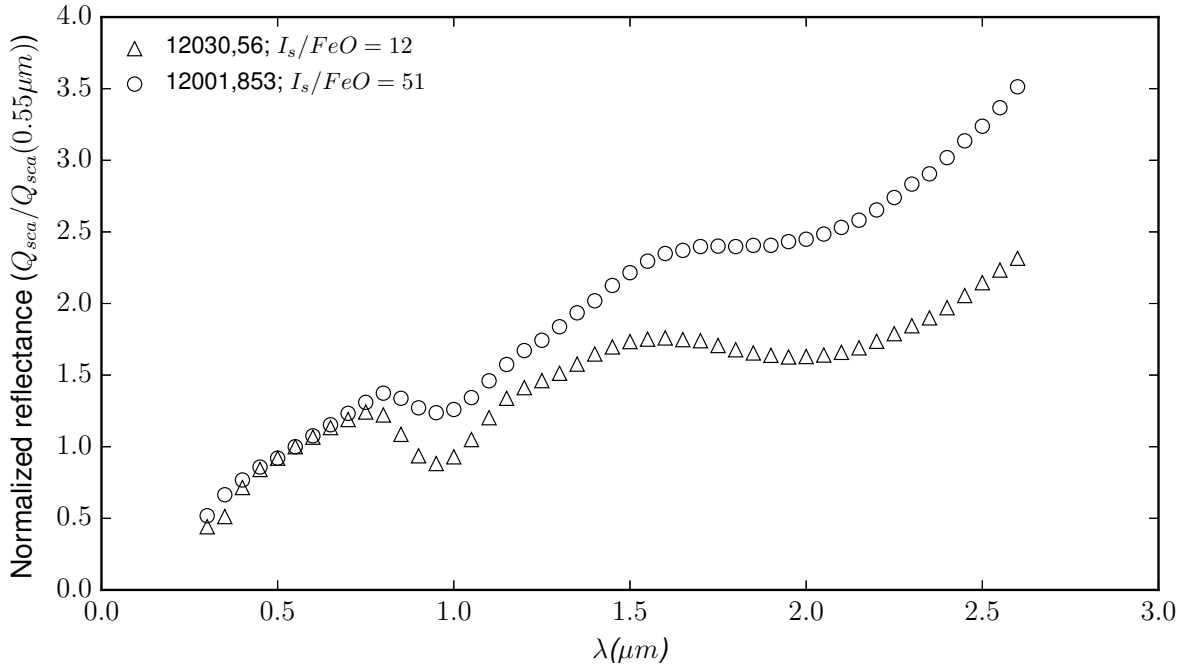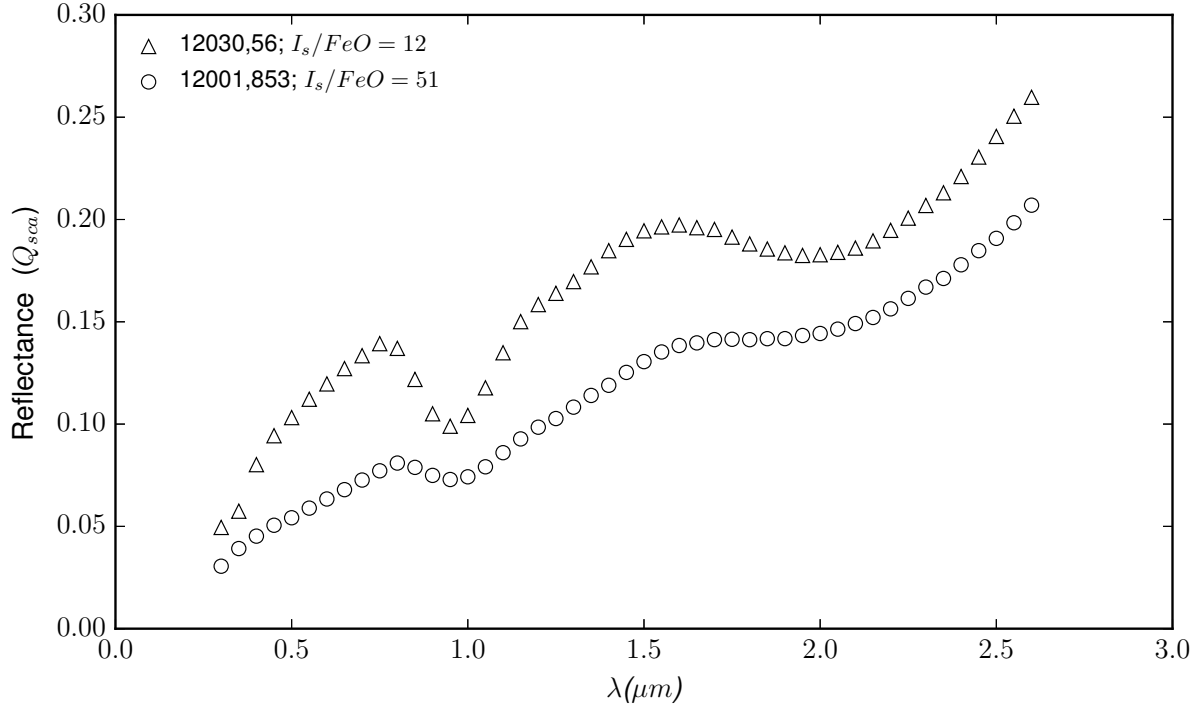
Figure 1. Reflectance spectra of two lunar regolith samples. Sample 12030,56 is an immature regolith (I_s/FeO=12), and sample 12001,853 is submature (I_s/FeO=51). These data are available at NASA RELAB database.

coefficients of the Legendre polynomials and the correlation angle for autocorrelation. The values of these parameters (except the radius r) are fixed for all the simulations presented in this work: $\sigma = 0.2$, $\nu = 3.3$, $l_{min} = 2$ and $l_{max} = 11$. These values are in agreement with the shape distribution of a silicate sample collected in the Sahara desert (Libya) presented in Muñoz et al. (2007), considered as a reasonable standard irregular particle.
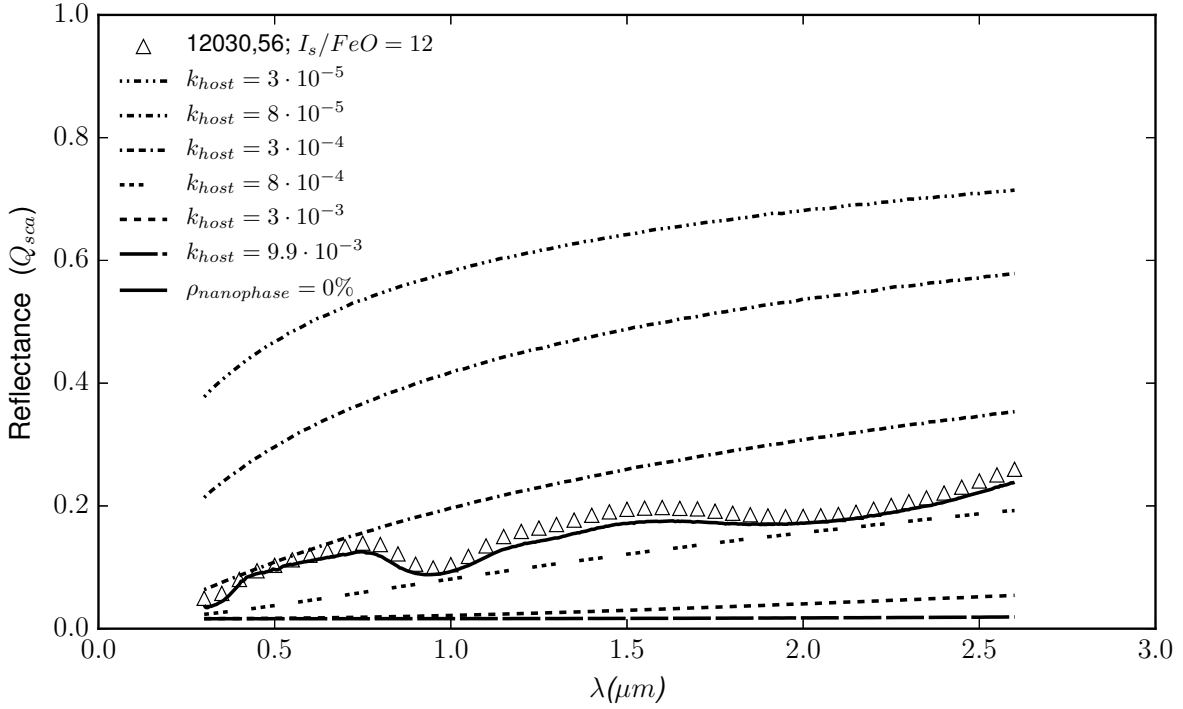
Figure 2. Fitting model for non-weathered host particle. The triangles correspond to the experimental spectrum for sample 12030,56 which acts as model. The dashed lines are the computed spectra when using a constant k_{host}. Solid line is the spectra resulting when fitting the model with the computations.

4.2. *Simulations methodology.*

The procedure consists of three steps. Firstly, we compute the imaginary part of the refractive index, k_{host}, of the non-weathered host particle. Then, a first simulation of a weathered particle is performed by adding iron inclusions ($npFe^0$) to the non-weathered host particle. The result of this simulation is equivalent to the single scattering behaviour of irregular space weathered particles. To fully simulate the reflectance spectra of an ensemble of regolith particles, a radiative transfer simulation is computed by using the results of the single-scattering particles acting as inclusions within a 10 cm-radius vacuum sphere.

The simulations cover the wavelength range from 300 nm to 2600 nm with a resolution of 20 nm. In all computed cases, the particle size is fixed to 33.5 μm as an average value representative of the studied samples. One of the multiple outputs of the code is the scattering efficiency, Q_{sca}, which is defined as the ratio of the scattering cross section σ_{sca} to the geometrical cross section πa^2, where a is the host particle radius. The dependence of Q_{sca} versus the wavelength λ conforms the reflectance spectrum.

The wavelength dependence of k_{host} is derived by SIRIS3 as follows: we perform six sets of simulations with k_{host} ranging between $8 \cdot 10^{-5}$ and $3 \cdot 10^{-2}$ to cover a wide range of values. In each case, k_{host} is constant along the wavelength range. The real part of the refractive index is fixed to 1.67 at all computed wavelengths (Goguen et al. 2010). A reflectance spectrum is computed by SIRIS3 for each k_{host}. The reflectance spectrum of the immature sample 12030,56 is fitted by combining all the six simulations (Figure 2). The $k_{host}(\lambda)$ values obtained by this fitting as presented in Figure 3, are then used to simulate the host particle.

The scattering matrix and single scattering albedos for 33.5 μm lunar grains with $npFe^0$ inclusions are computed using Gaussian-random-spheres in SIRIS3. The scattering properties of the inclusions are computed using Rayleigh approximation, due to their small size compared to the wavelength (15-25 nm). In the Rayleigh approximation, the scattering efficiency Q_{sca} and the absorption efficiency Q_{abs} of a particle with a size parameter $x = \frac{2\pi a}{\lambda}$ are given by:

$$Q_{sca} = \frac{8}{3} x^4 \left| \frac{m_{iron}^2 - 1}{m_{iron}^2 + 2} \right|^2, \quad Q_{abs} = 4 x \operatorname{Im} \left(\frac{m_{iron}^2 - 1}{m_{iron}^2 + 2} \right), \tag{4}$$
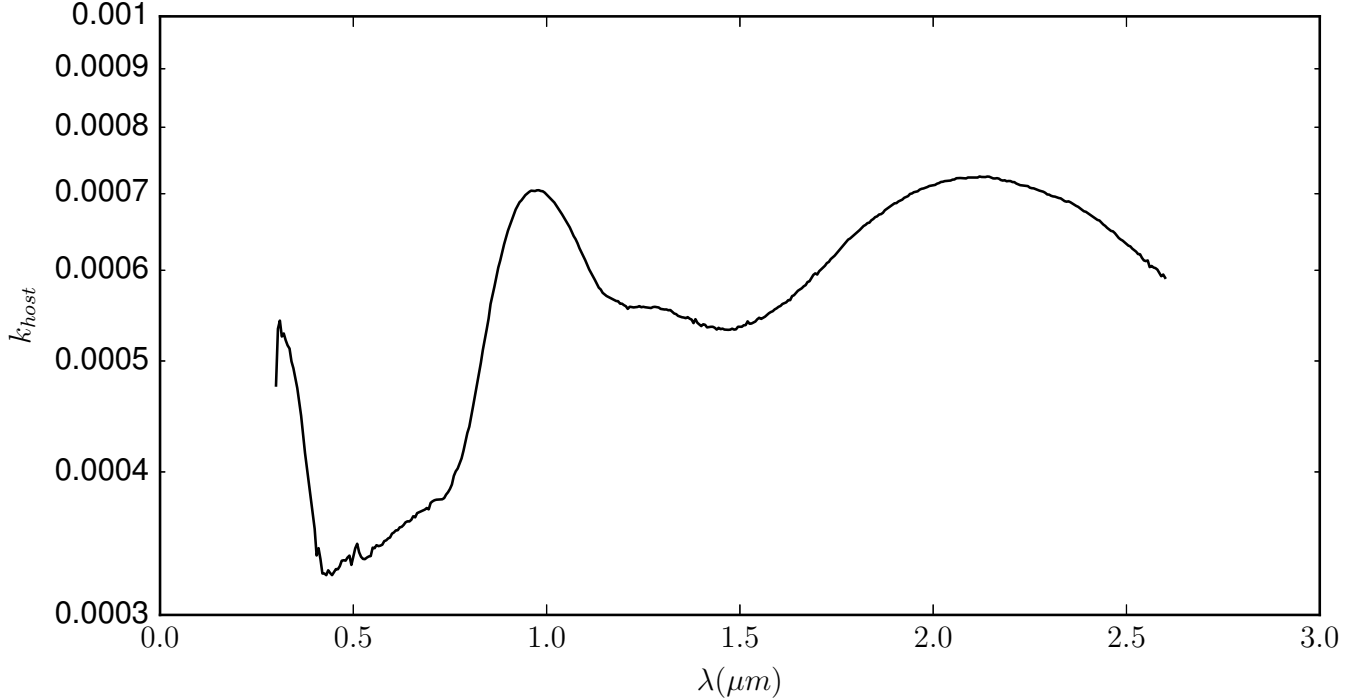
Figure 3. Modeled imaginary part of the refractive index (k_{host}) for the non-weathered particle. The experimental spectrum of 12030,56 is used as a non-weathered sample.

where m_{iron} is the relative complex refractive index of the iron particle in the host particle matrix. We obtain the complex refractive index for iron from Cahill et al. (2012). The actual inputs for the SIRIS3 code, the single-scattering albedo ϖ_{iron} and volume fraction of inclusions, $\rho_{nanophase}$ in the host matrix, are derived as:

$$\varpi_{iron} = \frac{Q_{sca}}{Q_{sca} + Q_{abs}} \text{ and } \rho_{nanophase} = \frac{4a}{3\ell(Q_{sca} + Q_{abs})}, \tag{5}$$

where ℓ is the mean-free-path in the host matrix and a is the radius of each npFe^0 inclusion, set to 8.25 nm. Each inclusion has then a size of 16.5 nm, half of the 33 nm size established as upper limit to consider it as nanophase iron.

The obtained scattering properties for the inclusions are then used in SIRIS3 so that the npFe^0 particles act as diffuse scatterers inside a 33.5 µm non-weathered host lunar grain. The inclusions are assumed to be uniformly distributed inside the grain. The amount of inclusions is controlled by means of the volume fraction parameter $\rho_{nanophase}$.

In order to model the reflectance spectrum of space weathered lunar regolith, the computed scattering matrices and single-scattering albedos of the weathered particles are used in the code so that 33.5 µm lunar grains with internal inclusions act as diffuse scatterers inside a vacuum volume of a radius of 10 cm. The volume fraction of lunar grains in the vacuum space was set to $\rho_{grains}=15\%$.

5. RESULTS.

In Figure 3, we present the retrieved imaginary part of the refractive index (k_{host}) as a function of wavelength for non-weathered lunar regolith. The results are based on the best-fitted reflectance spectrum for the immature 12030,56 lunar sample displayed in Figure 2.

In Figure 4 we present the dependence of the computed reflectance spectra on different values of npFe^0 volume fraction, $\rho_{nanophase}$, which is varied in the range 0.01% to 10%. As shown (Figure 4, top panel), even in the case of very small amount of inclusions (as low as $\rho_{nanophase}=0.01\%$) the darkening and dampening of absorption bands are clearly seen in the computed spectra. In contrast, when $\rho_{nanophase}=1\%$ the spectrum becomes unrealistic: all structure has disappeared and the spectrum becomes almost featureless at visible wavelengths. At $\rho_{nanophase}=10\%$ the spectrum corresponds to a completely black surface. In the bottom panel of the same figure, the reddening can be easily observed between $\rho_{nanophase}=0\%$ and $\rho_{nanophase}=0.1\%$. For values $\rho_{nanophase} \geq 1\%$ the spectra start to fade in the visible range. Hereafter we focus only in those $\rho_{nanophase} <1\%$ results.
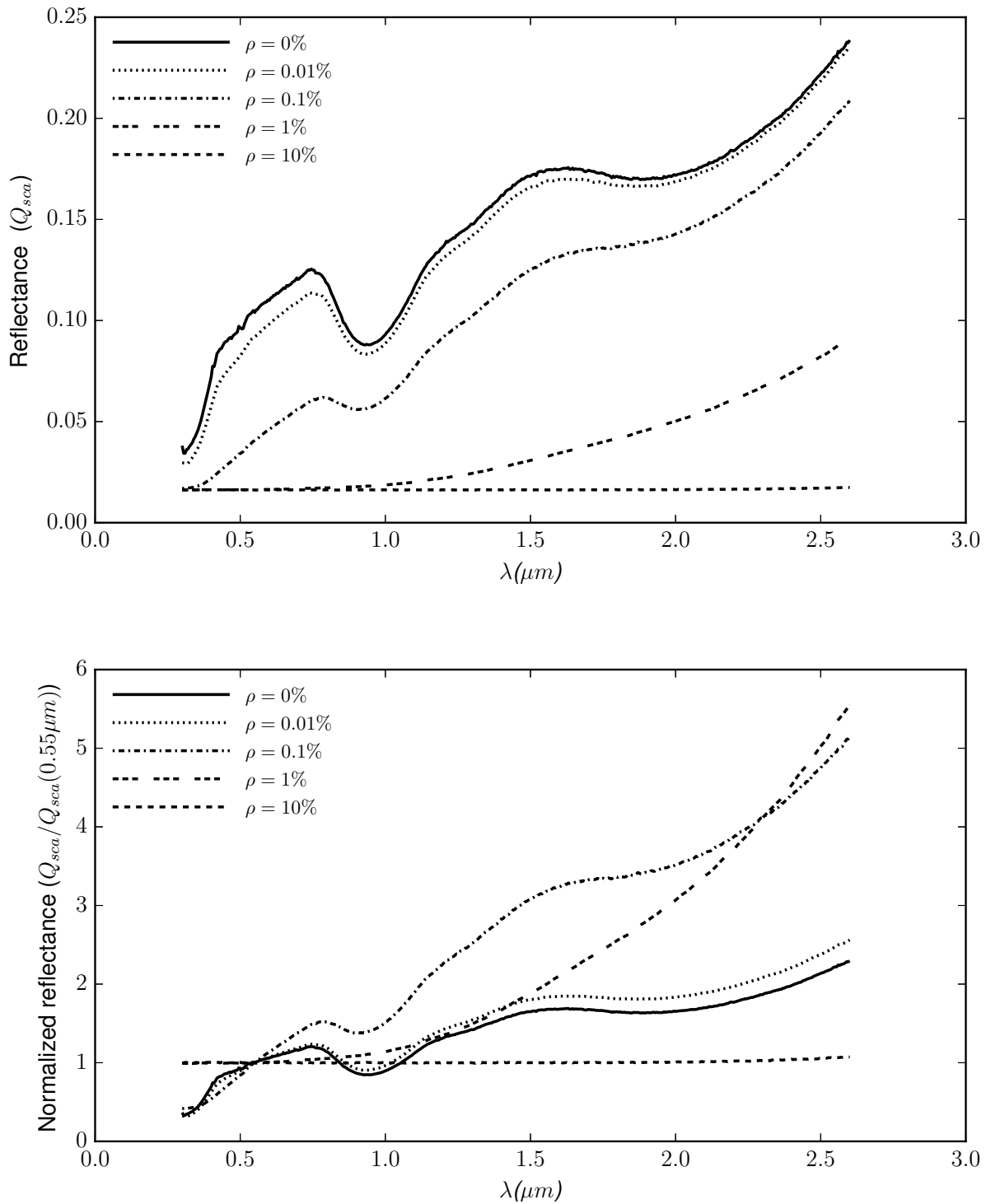
Figure 4. Computed reflectance spectra for five different volume fractions ($\rho_{nanophase}$=0%, 0.01%, 0.1%, 1%, and 10%). $\rho_{nanophase}$=0% curve is the fitted result of experimental spectrum soil 12030,56. Top panel correspond to the original simulation data. Bottom panel shows the same spectra normalized to unity at 550 nm.

In Figure 5 we present a comparison between experimental spectrum for sample 12001,853 and spectra simulations for various values of $\rho_{nanophase}$. In the bottom panel (normalized data) the experimental spectra are located between the $\rho_{nanophase}$=0.01% and 0.1% simulations spectra.

6. DISCUSSION.

As shown in Figure 4, SIRIS3 code qualitatively reproduces the measured effects on the reflectance spectra as the amount of npFe^0 is increased. The reflectance spectrum darkens, the slope becomes steeper and the absorption bands tend to vanish. In Figure 5 we find that the experimental spectrum for sample 12001,853 is located between the simulated spectra for values $\rho_{nanophase}$=0.01% and $\rho_{nanophase}$=0.1%.

To our knowledge, there are no published data of the volume fraction of nanophase iron inclusions for the samples studied in the present work. To compare the results of our simulations with measured properties of the samples we use two equations to transform the FeO wt% (weight percent) and the maturity index (I_s/FeO) into npFe^0 volume fraction.

Firstly, we use the empirical equation from Morris (1980) to obtain the Fe^0/FeO ratio corresponding to Fe^0 with sizes from 4 nm to 33 nm as is the case in our simulations:

$$\frac{Fe^0}{FeO} = [(3.20 \pm .08) \times 10^{-4}]\frac{I_s}{FeO} + (1 \pm 5) \times 10^{-4}. \tag{6}$$

Taylor et al. (2001) provide FeO wt% values of 17.6 and 16.9 for samples 12030,56 and 12001,853, respectively along with the maturity index of both samples. From the previous equation and those data, we obtain the values of Fe^0 weight percent of 0.069 ± 0.013 for sample 12030,56, and 0.28 ± 0.03 for sample 12001,853. To transform from weight percent to volume fraction we use the equation from Lucey and Riner (2011):

$$V_{Fe} = \frac{M_{Fe}\rho_h}{\rho_{Fe}}, \tag{7}$$

where M_{Fe} is the Fe^0 wt%, ρ_h is the host particle density, and ρ_{Fe} is the Fe density. As ρ_h we use a mean value of 3 g/cm^3 (Colwell et al. 2007), and for ρ_{Fe} we use 7.86 g/cm^3. Using those values, Equation 7, and the results from the Equation 6 for the samples studied in this work, we obtain $\rho_{nanophase}$=0.023 % for sample 12030,56 and $\rho_{nanophase}$=0.105 % for sample 12001,853.

As shown in Figure 5, the modeled spectrum is nearly consistent with the observed spectrum, however, the model has a slightly higher reflectance than the observed spectrum and it is not as red. The computed spectrum for $\rho_{nanophase}$=0.1 % is very similar to the measured spectrum for sample 12001,853. In particular, it shows a nearly perfect fit to the experimental spectra in the wavelength range from 1.3 µm to 2.6 µm. Some differences with the experimental data are found in the 0.3 µm to 1.2 µm wavelength range. Several sources of errors in the simulations might be taken in consideration as possible explanation of the observed discrepancies at shorter wavelengths. As mentioned, in our computations we assume the nanophase iron inclusions uniformly distributed throughout the host particle volume instead of locating the npFe^0 on a thin layer close the surface of the grain. Another issue is the monodispersity of the size distribution of the iron inclusions in the host particle, which could be more realistically replicated by taken into account the Britt-Pieters microphase, but this requires a different simulation method. It would be interesting also to compute a size distribution of host particles to check whether the regolith spectrum is more accurately reproduced.

7. CONCLUSIONS.

SIRIS3 code qualitatively reproduces the effects of nanophase iron inclusions on the reflectance spectra of space weathered lunar soils. As a first step, a non-weathered reflectance spectrum is simulated. As a result, an imaginary refractive index model as function of wavelength is obtained for immature lunar regolith. Once we have an immature regolith model, we reproduce the space weathering by assuming Rayleigh iron internal scatterers inside a large host particle. In the simulations, the increase of npFe^0 volume fraction produces a darkening effect, a reddening of the spectra and weakening of the absorption bands. A saturation of the space weathering effects is found for $\rho_{nanophase} \geq$ 1%, as the spectrum flattens with a very low reflectance.

A comparison between the experimental spectrum for lunar soil 12001,853 with computed spectra for $\rho_{nanophase}$=0%, 0.01%, and 0.1% is made. When comparing simulated and experimental spectra, we find a good agreement between experimental and simulated npFe^0 volume fractions. Still some discrepancies between experimental and computed spectra are found. This could be due to the fact that not all the parameters influencing the weathering effects could have been properly taken into account. Among other reasons, and owing to a limitation of the code, the nanophase iron has been supposed to be uniformly distributed inside the host particle instead of being located near the surface. Also, the internal inclusions and the host particles are simulated with a single size instead of a size distribution, that could be more realistic.
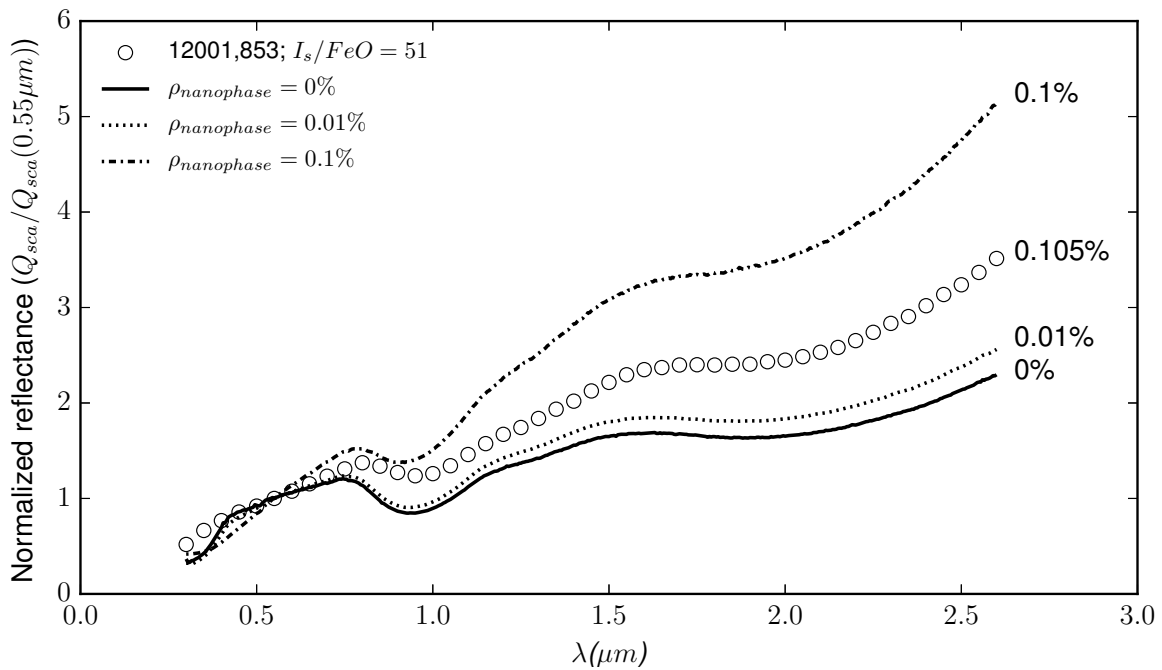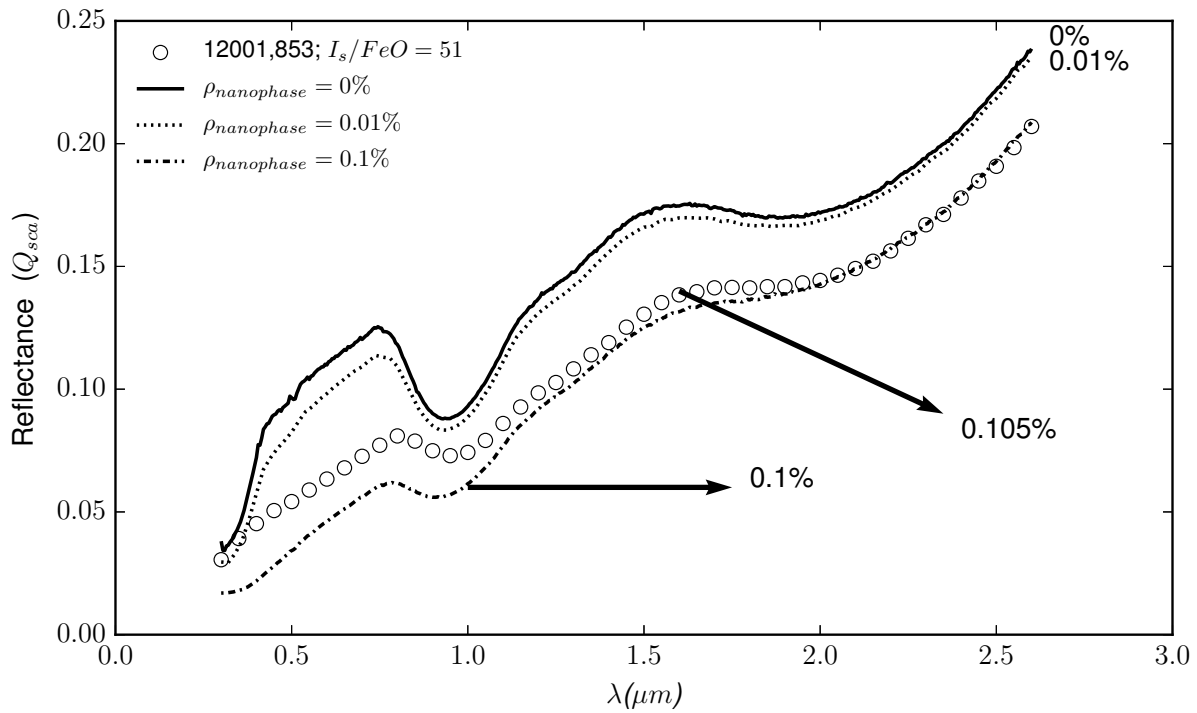
Figure 5. Top panel shows reflectance spectra comparison between the experimental lunar regolith spectrum for sample 12001,853 and three computed reflectance spectra with space weathering inclusions (volume fractions $\rho_{nanophase}$=0%, 0.01%, and 0.1%). The numbers next to each spectrum are the correspondent volume fraction (computed for the sample and used as input for the simulations). Bottom panel shows the same spectra normalized to unity at 550 nm.

The overall results show that space weathering must be considered when computing the scattering of such susceptible samples as those found in airless bodies. The role of npFe^0 inclusions in simulations is essential to reproduce and characterize the reddening, darkening and weakening of absorption bands in the reflectance spectra of these samples. Although this ray optic code with diffuse internal medium has demonstrated its ability to nearly reproduce the space weathering effects over visible to near-infrared spectra, further improvements should be made. It would be necessary to implement the npFe^0 layer depth and the possibility to mimic npFe^0 size distributions, as well as other space weathering subproducts.

ACKNOWLEDGEMENTS

REFERENCES

Britt, D.T. and Pieters, C.M. 1994, Geochim. Cosmochim. Acta, Vol. 98, No. 18, 3905-3919.

Brunetto, R., Romano, F., Blanco, A. et al. 2005, Icarus, 180, 546–554.

Brunetto, R., Lantz, C., Ledu, D. et al. 2014, Icarus, 237, 278-292.

Brunetto R., Loeffler M. J., Nesvorný D. et al. 2015, Asteroid surface alteration by space weathering processes. In Asteroids IV (P. Michel et al., eds.), pp. 597–616. Univ. of Arizona, Tucson.

Burns, R.G. 1970, Am. Mineral., vol. 55.

Cassidy, W. and Hapke, B. 1975, Icarus, vol. 25, 371-383.

Cahill,J.T.S., Blewett,D.T., Nguyen,N.V. et al. 2012, GeoRL, v. 39, n. 10.

Clark, B.E., Hapke, B., Pieters, C. and Britt, D. 2002, "Asteroid Space Weathering and Regolith Evolution", Asteroids III, ed. Bottke, Jr., W.F., Cellino, A., Paolicchi, P. and Binzel, R.P., p. 585-599.

Cloutis, E.A and Gaffey, M.J. 1991, J. Geoph. Res., 96, E5, 22809-22826.

Colwell, J., Batiste, S., Horányi, M. et al. 2007, Rev. Geophys., 45, RG2006.

Conel, J., and Nash, D. 1970, Geochim. Cosmochim. Acta, Suppt, 1, 2013-2024.

Domingue, D.L., Chapman, C.R., Killen, R.M. et al. 2014, Space Sci. Rev., 181, 121-214.

Escobar-Cerezo, J., Palmer, C., Muñoz, O. et al. 2017, ApJ, 838, 74.

Goguen, J., Stone, T., Kieffer, H. and Buratti, B. 2010, Icarus, 208, 548-557.

Gold, T., Campbell, M., and O'Leary B. 1970, Geochim. Cosmochim. Acta, Suppl., 1, 2149-2154.

Hapke, B., Cohen, A., Cassidy, W. and Wells, E. 1970, Geochim. Cosmochim. Acta,Suppl.,1, 2199-2212.

Hapke, B., Cassidy, W., and Wells, E., 1975, The Moon, vol. 13, 339-353.

Hapke, B. 2001, J. Geoph. Res., 106, E5, 10039-10073.

Keller, L. and McKay, D. 1997, Geochimica et Cosmochimica Acta, Vol. 61, No. 11, 2311-2341.

Kohout, T., Čuda, J., Filip, J. et al. 2014, Icarus, 237, 75-83.

Lucey, P.G. and Riner, M.A. 2011, Icarus, 212, 451-462.

Marchi, S., Brunetto, R., Magrin, S., et al. 2005, Astron. Astrophys., 443, 769–775.

Martikainen, J., Penttilä, A., Gritsevich, M. et al. 2018, JQSRT, 208, 144-157.

McKay, D.S., Heiken, G.H., Taylor, R.M. et al. 1972, Proc. Lunar Planet. Sci. Conf., vol. 3, p.983.

Morris, R. 1978, Lunar and Plan. Sci. IX, pp. 760-762. Abstract. TKO.

Morris, R. 1980, Proc. Lunar Planet. Sci. Conf. 11th, p. 1697-1712.

Muinonen, K., Nousiainen, T., Fast, P. et al. 1996, JQSRT, V. 55, Issue 5, 577-601.

Muinonen, K., Nousiainen, T., Lindqvist, H. et al. 2009, JQSRT, 110, 1628–1639.

Muñoz, O., Volten, H., Hovenier, J. W. et al. 2007, J. Geophys. Res., 112, D13215.

Noble, S., Pieters, C., Taylor L. et al. 2001, Meteor. & Planet. Sci. 36, 31-42.

Noble, S., Pieters, C. & Keller L. 2007, Icarus ,Vol. 192, Issue 2, p. 629-642.

Nousiainen, T., Muñoz, O., Lindqvist, H. et al. 2011, JQSRT, V. 112, Issue 3, 420-433.

Pieters, C. M., Fischer, E. M., Rode, O. and Basu, A. 1993, J. Geoph. Res., 98, E11, 20817-20824.

Pieters, C. M., Taylor, L. A., Noble, S. K. et al. 2000, Meteor. & Planet. Sci. 35, 1101-1107.

Pieters, C. M., and S. K. Noble 2016, J. Geoph. Res. Planets, 121, 1865–1884.

Strazzulla, G., Dotto, E., Binzel, R. et al. 2005, Icarus, Vol. 174, Issue 1, p. 31-35.

Tang, H., Wang, S., & Li, X. 2012. Planet. Space Sci. 60, 322–327.

Taylor, L. A., Pieters, C. M., Keller, L. P. et al. 2001, J. Geoph. Res., 106, E11, 27985-27999.

Trang, D., Lucey, P.G. and Izenberg,N.R. 2017, Icarus, Vol. 293, p. 206-217.

Wells, E., and Hapke, B. 1977, Science, 195, 977-979.

Chapter 7

Conclusions

This thesis gathers the results of a study on the lunar regolith simulant JSC-1A using both experimental and computational approaches. According to the different results obtained, the conclusions can be summarized as:

- In paper I, the experimental measurements of the scattering matrix of the JSC-1A sample carried out at the IAA-CODULAB apparatus are presented. These measurements were performed at three visible wavelengths (488 nm, 520 nm, and 647 nm) in the scattering angle range 3° to 177°. An extrapolated scattering matrix $\mathbf{F}^{syn}$ is also presented to cover the whole scattering angle range. The results show the typical behaviour for randomly oriented irregular particles of mineral dust. The degree of linear polarization for unpolarized incident light shows a negative branch of 1.4%-2% at large scattering angles and a maximum of polarization of 12%-14%. The effect of the loss of the smaller particles fraction (<1 μm) is studied: the negative polarization branch disappears, the maximum increases to $\sim$17% and it moves to smaller scattering angles. The polarization colour suggest a nearly constant value of the imaginary part of the refractive index at visible wavelengths. From the extrapolated matrix, the depolarization factor at backscattering δ_L and the asymmetry parameter g are computed, yielding δ_L a value in the range of 0.3-0.4 depending on the wavelength and g=0.74 at all measured wavelengths, respectively.

- In paper II, a systematic study of the parameter space has been performed to test the sensitivity of the SIRIS code when varying physical properties of the particles as size, refractive index, density and composition of inhomogeneities in the host particle. Hematite and white clay are used to mimic very extreme media in terms of imaginary part of the refractive index. The inhomogeneities can be located inside the particle or its surface known as diffuse internal medium (DIM) and diffuse external medium (DEM), respectively. These inhomogeneities are managed by the code through the volume fraction parameter ρ_{int} for DIM and the optical thickness τ_{ext} for DEM. The results of the size effects studies show that if the host particle is very absorbing, the sensitivity to any DIM material is almost negligible, while the opposite occurs for DEM.

The scattering of weakly absorbing host particles is sensitive to any DIM or DEM. The simulations of size distributions of particles show smoother curves and both DIM and DEM produce a narrowing of the forward scattering peak of the phase function when the density of inhomogeneities increases. In terms of the degree of linear polarization, DIM inhomogeneities produce an increase of the maximum, while the opposite effect happens for DEM. The former effect could be produced due to a darkening effect inside the particle, triggered by the internal scattering and subsequent absorption of light as the number of internal scatterers increases. As a final test, both internal inclusions and surface roughness are included in a size distribution of particles trying to reproduce the measured scattering matrix of a cosmic dust analog. The scattering matrix is qualitatively well reproduced with very small amount of internal inclusions (ρ_{int}=1%) and a reasonable density of surface roughness (τ_{ext}=0.5).

- In paper III, the SIRIS code is used to reproduce the effects of space weathering over the reflectance spectra of a lunar regolith sample. The reduced iron nanophase is replicated by using internal inclusions with the corresponding physical parameters (iron nanophase refractive index and single scattering albedo) in a non-weathered regolith host particle. As a first step, the reflectance spectra of a non weathered lunar regolith host particle was obtained. From the non-weathered lunar regolith model it is possible to retrieve the imaginary part of the refractive index (k_{host}) by fitting a measured spectrum with several simulations. The increase of volume fraction of iron nanophase produced the three expected space weathering effects: darkening, reddening and shallowing of the absorption bands. These effects saturate very quickly as the volume fraction increases. For those values above 1%, the spectrum becomes unrealistic: the absorption bands totally disappear and the reddening distort the shape of the spectrum. For higher values the darkening overcomes the other effects and the spectrum becomes totally black.

As future work, we intend to expand our studies along several research lines. The most immediate is to perform new laboratory measurements to study the negative polarization branch. One of the conclusions of Paper I is that this negative branch can be produced by submicron particles. Further measurements must be done to study if a similar effect can be produced by submicron surface features. From the point of view of lunar regolith characterization, it would be interesting to study different lunar analogs. The MLS-1 is a highland regolith simulant while the JSC-1A is a mare regolith simulant. Some differences have been spotted between these two kind of materials, e.g their composition (titanium, aluminum and iron oxides) and where can be found on the lunar surface. A more complete characterization of the moon regolith will be achieved with the laboratory measurements of any simulant resembling the highland regolith. In terms of the simulations, the computer science is still a young field of knowledge that has many opportunities to improve. To mention some of them related with this thesis, it would be interesting to be able to locate the inclusions in a small layer near the surface of the host particle instead of the whole

volume, as these would be a more realistic model of space weathering. It is also known that the reflectance spectra of the regolith depend on the size of the particles measured, so simulations with size distributions of host particles instead of a single-sized particle would be a better approach.

Bibliography

[1]   D. T. Britt and C. M. Pieters. "Darkening in black and gas-rich ordinary chondrites: The spectral effects of opaque morphology and distribution". In: *Geochimica et Cosmochimica Acta* 58 (Sept. 1994), pp. 3905–3919. DOI: 10.1016/0016-7037(94)90370-0.

[2]   D. D. Dabrowska, O. Muñoz, F. Moreno, J. L. Ramos, J. Martínez-Frías, and G. Wurm. "Scattering matrices of martian dust analogs at 488 nm and 647 nm". In: *Icarus* 250 (Apr. 2015), pp. 83–94.

[3]   A. Dollfus and E. Bowell. "Polarimetric Properties of the Lunar Surface and its Interpretation. Part I. Telescopic Observations". In: *Astronomy and Astrophysics* 10 (Jan. 1971), p. 29.

[4]   B. T. Draine and P. J. Flatau. "Discrete-dipole approximation for scattering calculations". In: *Journal of the Optical Society of America A* 11 (Apr. 1994), pp. 1491–1499. DOI: 10.1364/JOSAA.11.001491.

[5]   G. Fielder. "On the polarization of light reflected by the Moon". In: *Structure of the Moon's surface*. 1st ed. Pergamon Press, 1961. Chap. 6, pp. 79–90.

[6]   J. D. Goguen, T. C. Stone, H. H. Kieffer, and B. J. Buratti. "A new look at photometry of the Moon". In: *Icarus* 208 (Aug. 2010), pp. 548–557. DOI: 10.1016/j.icarus.2010.03.025.

[7]   J. W. Hovenier. "Measuring scattering matrices of small particles at optical wavelengths". In: *Light scattering by Nonspherical particles*. Ed. by M. I. Mishchenko, J. W. Hovenier, and L. D. Travis. 1st ed. Academic Press, 2000. Chap. 12, 355–365.

[8]   J. W. Hovenier and C. van der Mee. "Relationships for Matrices Describing Scattering by Small Particles". In: *Light scattering by Nonspherical particles*. Ed. by M. I. Mishchenko, J. W. Hovenier, and L. D. Travis. 1st ed. Academic Press, 2000. Chap. 3, pp. 61–89.

[9]   J. W. Hovenier, H. Volten, O. Muñoz, W. J. van der Zande, and L. B. Waters. "Laboratory study of Scattering Matrices for Randomly Oriented Particles: Potentials, Problems, and Perspectives". In: *Journal of Quantitative Spectroscopy and Radiative Transfer* 79 (Sept. 2003), p. 741.

[10]   J. W. Hovenier, C. Van Der Mee, and H. Domke, eds. *Transfer of polarized light in planetary atmospheres : basic concepts and practical methods.* Vol. 318. Astrophysics and Space Science Library. 2004.

[11]   J. W. Hovenier and D. Guirado. "Zero slopes of the scattering function and scattering matrix for strict forward and backward scattering by mirror symmetric collections of randomly oriented particles". In: *Journal of Quantitative Spectroscopy and Radiative Transfer* 133 (2014), pp. 596–602.

[12]   A. J. Hunt and D. R. Huffman. "A new polarization-modulated light scattering instrument". In: *Review of Scientific Instruments* 44 (Dec. 1973), pp. 1753–1762.

[13]   M. M Kiphardt, ed. *Experimental determination of scattering matrices of ice crystals.* Graduation report. 1993.

[14]   L. Liu, M. I. Mishchenko, J. W. Hovenier, H. Volten, and O. Muñoz. "Scattering matrix of quartz aerosols: comparison and synthesis of laboratory and Lorenz-Mie results". In: *Journal of Quantitative Spectroscopy and Radiative Transfer* 79 (2003), pp. 911–920. DOI: 10.1016/S0022-4073(02)00328-X.

[15]   B. Lyot. "Recherches sur la polarisation de la lumière des planètes et de quelques substances terrestres". In: *Annales de l'Observatoire de Paris, section de Meudon* 8 (1929), pp. 1–161.

[16]   D. S. McKay, R. M. Fruland, and G. H. Heiken. "Grain size and the evolution of lunar soils". In: *Lunar and Planetary Science Conference Proceedings.* Vol. 5. Lunar and Planetary Science Conference Proceedings. 1974, pp. 887–906.

[17]   G. Mie. "Beiträge zur Optik trüber Medien, speziell kolloidaler Metallösungen". In: *Annalen der Physik* 330 (1908), pp. 377–445. DOI: 10.1002/andp.19083300302.

[18]   M. I. Mishchenko. *Electromagnetic scattering by particles and particle groups.* Cambridge University Press, New York, 2014.

[19]   M. I. Mishchenko, L. D. Travis, and D. W. Mackowski. "T-matrix computations of light scattering by nonspherical particles: A review". In: *Journal of Quantitative Spectroscopy and Radiative Transfer* 55.5 (1996), pp. 535 –575. ISSN: 0022-4073. DOI: https://doi.org/10.1016/0022-4073(96)00002-7.

[20]   M. I. Mishchenko, J. W. Hovenier, and L. D. Travis. *Light scattering by nonspherical particles : theory, measurements, and applications.* Academic Press, 2000.

[21]   M. I. Mishchenko, L. D. Travis, and A. A. Lacis. *Scattering, absorption, and emission of light by small particles.* Cambridge University Press, UK, 2002.

[22]   O. Muñoz, H. Volten, J. W. Hovenier, T. Nousiainen, K. Muinonen, D. Guirado, F. Moreno, and L. B. F. M. Waters. "Scattering matrix of large Saharan dust particles: Experiments and computations". In: *Journal of Geophysical Research: Atmospheres* 112.D13 (2007). ISSN: 2156-2202. DOI: 10.1029/2006JD008074.

[23] O. Muñoz, F. Moreno, D. Guirado, J. L. Ramos, A. López, F. Girela, J. M. Jerónimo, L. P. Costillo, and I. Bustamante. "Experimental determination of scattering matrices of dust particles at visible wavelengths: The IAA light scattering apparatus". In: *Journal of Quantitative Spectroscopy and Radiative Transfer* 111 (Jan. 2010), pp. 187–196.

[24] O. Muñoz, F. Moreno, D. Guirado, J. L. Ramos, H. Volten, and J. W. Hovenier. "The IAA cosmic dust laboratory: Experimental scattering matrices of clay particles". In: *Icarus* 211 (Jan. 2011), pp. 894–900.

[25] O. Muñoz, F. Moreno, D. Guirado, D. D. Dabrowska, H. Volten, and J. W. Hovenier. "The Amsterdam-Granada Light Scattering Database". In: *Journal of Quantitative Spectroscopy and Radiative Transfer* 113 (Feb. 2012), pp. 565–574.

[26] K. Muinonen, T. Nousiainen, P. Fast, K. Lumme, and J. Peltoneimi. "Light scattering by Gaussian random particles: ray optics approximation". In: *Journal of Quantitative Spectroscopy and Radiative Transfer* 55 (May 1996), pp. 577–601. DOI: `10.1016/0022-4073(96)00003-9`.

[27] K. Muinonen, T. Nousiainen, H. Lindqvist, O. Muñoz, and G Videen. "Light scattering by Gaussian particles with internal inclusions and roughened surfaces using ray optics". In: *Journal of Quantitative Spectroscopy and Radiative Transfer* 110.14 (2009), pp. 1628 –1639. ISSN: 0022-4073. DOI: `https://doi.org/10.1016/j.jqsrt.2009.03.012`.

[28] T. Nousiainen, K. Muinonen, J. Avelin, and A. Sihvola. "Microwave backscattering by nonspherical ice particles at 5.6GHz using second-order perturbation series". In: *Journal of Quantitative Spectroscopy and Radiative Transfer* 70.4 (2001). Light Scattering by Non-Spherical Particles, pp. 639 –661. ISSN: 0022-4073. DOI: `https://doi.org/10.1016/S0022-4073(01)00035-8`. URL: `http://www.sciencedirect.com/science/article/pii/S0022407301000358`.

[29] F. R. S. Rayleigh. "X. On the electromagnetic theory of light". In: *The London, Edinburgh, and Dublin Philosophical Magazine and Journal of Science* 12.73 (1881), pp. 81–101. DOI: `10.1080/14786448108627074`.

[30] I. G. Shkuratov, N. V. Opanasenko, and M. A. Kreslavskii. "Polarimetric and photometric properties of the moon: Telescopic observations and laboratory simulations. I - The negative polarization". In: *Icarus* 95 (Feb. 1992), pp. 283–299. DOI: `10.1016/0019-1035(92)90044-8`.

[31] I. G. Shkuratov and N. V. Opanasenko. "Polarimetric and photometric properties of the moon: Telescope observation and laboratory simulation. II - The positive polarization". In: *Icarus* 99 (Oct. 1992), pp. 468–484. DOI: `10.1016/0019-1035(92)90161-Y`.

[32] Y. Shkuratov, L. Starukhina, H. Hoffmann, and G. Arnold. "A Model of Spectral Albedo of Particulate Surfaces: Implications for Optical Properties of the Moon". In: *Icarus* 137 (Feb. 1999), pp. 235–246. DOI: `10.1006/icar.1998.6035`.

[33] Y. Shkuratov, V. Kaydash, V. Korokhin, Y. Velikodsky, N. Opanasenko, and G. Videen. "Optical measurements of the Moon as a tool to study its surface". In: *Planetary and Space Science* 59 (Oct. 2011), pp. 1326–1371. DOI: 10.1016/j.pss.2011.06.011.

[34] M. F. Sterzik, S. Bagnulo, and E. Palle. "Biosignatures as revealed by spectropolarimetry of Earthshine". In: *Nature* 483 (Mar. 2012), pp. 64–66.

[35] N. Umov. "Chromatische depolarisation durch Lichtzerstreuung". In: *Phys. Zeit.* 6 (1905), 674–676.

[36] H. C. van de Hulst. *Light Scattering by Small Particles*. New York: John Wiley & Sons, 1957.

[37] H. Volten, O. Muñoz, E. Rol, J. F. de Haan, W. Vassen, J. W. Hovenier, K. Muinonen, and T. Nousiainen. "Scattering matrices of mineral aerosol particles at 441.6 nm and 632.8 nm". In: *Journal of Geophysical Research* 106 (Aug. 2001), pp. 17375–17402. DOI: 10.1029/2001JD900068.

[38] H. Volten, O. Muñoz, J. W. Hovenier, and L. B. Waters. "An update of the Amsterdam Light Scattering Database." In: *Journal of Quantitative Spectroscopy and Radiative Transfer* 100 (2006), 437–443.

[39] P. C. Waterman. "Matrix formulation of electromagnetic scattering". In: *Proceedings of the IEEE* 53.8 (1965), pp. 805–812. ISSN: 0018-9219.

[40] M. Wolff. "Theory and application of the polarization-albedo rules". In: *Icarus* 44 (Dec. 1980), pp. 780–792. DOI: 10.1016/0019-1035(80)90144-X.

[41] P. Yang and K. N. Liou. "Finite Difference Time Domain Method for Light Scattering by Nonspherical and Inhomogeneous Particles". In: *Light Scattering by Nonspherical Particles : Theory, Measurements, and Applications*. Ed. by M. I. Mishchenko, J. W. Hovenier, and L. D. Travis. Jan. 2000, p. 174.

[42] E. Zubko, G. Videen, Y. Shkuratov, K. Muinonen, and T. Yamamoto. "The Umov effect for single irregularly shaped particles with sizes comparable with wavelength". In: *Icarus* 212 (Mar. 2011), pp. 403–415. DOI: 10.1016/j.icarus.2010.12.012.